Impact Volatilization of Calcite and Anhydrite and the Effect on Global Climate from K/T Impact Crater at Chicxulub

Thesis by

Wenbo Yang

In Partial Fulfillment of the Requirements

for the Degree of

Doctor of Philosophy

California Institute of Technology

Pasadena, California

1996

(Nov. 21, 1995)

Acknowledgments

Over the years, I have always felt being privileged to be a graduate student at Caltech. The years of experience here will definitely benefit my career and personal life through my life time.

First , I would like to sincerely thank my thesis advisor, Professor Thomas J. Ahrens. Without his years of academic guidance, financial support, personal care and encouragement, I would not be possible for me to accomplish any of my scientific research work here at Caltech.

Caltech is a unique place for doing scientific research and learn the most recent advances in science. When I have a question, there is always an answer or a suggestion that leads to the answer. I would like to express my sincere thanks to all the faculty members of the GPS division. Prof. Stevenson gave me a fascinating geophysics introduction class. Prof. Rossman helped me with one of my first year proposition and taught me a lot about minerals.

Thanks to all the staff and students and former students in the shock wave laboratory. Dr. T. Duffy set up the first version of the VISAR system which allowed my continued application and improvement of this apparatus possible. Dr. W. Anderson, Mr. G. Chen, Ms. K. Gallagher, Mr. C. Liu, and Dr. L. Rowan provided continued fellowship and help during our discussions and collaborations in research. Mr. A. Devora, Mr. P. Gelle and Mr. M. Long helped me with all my experiments. Thank you all.

I especially thank the assistance Professor Peter Wyllie has given me on phase diagrams and suggestions on improving the thesis proffered by Professors W. Clayton, G. Ravichandron and D. Stevenson.

The Seismological Laboratory staff members have always been both friendly and helpful. I thank you all for your help and care. Special thanks to S. Yamada, she is always ready to help me when I had need.

Finally, I heartily thank my dear wife, Sarah, and our lovely daughter, Toni. Over the years, your support and understanding make the hard work much easier.

Abstract

In geophysics and planetary science, it is important to understand the shock devolatilization process of minerals as these represent key elements in our understanding of the formation and evolution of atmosphere and ocean.

Shock vaporization experiments were carried out for porous (70% crystal density) anhydrite and porous (54% crystal density) up to 76 and 19 GPa, respectively. Velocity histories of aluminum-LiF window interface, which were driven by the vapor, were measured using velocity interferometer. Incipient and complete vaporization of $CaSO_4$ and $CaCO_3$ criteria have been obtained through thermodynamic calculations in which chemical dissociation or shock melting is taken into account. The incipient and complete vaporization pressures are 81±7 and 155±13 GPa for crystal anhydrite, and 27±1 and 67±6 GPa for porous anhydrite. For porous calcite, the incipient and complete vaporization pressure are 5.4±1.9 and 14.6±3.8 GPa, respectively. For crystal calcite, they are 54±6 and 103±12 GPa, respectively.

One-dimensional numerical simulation was used to simulate the measured velocity profiles. The vaporized products can be described by equation, $P=(\gamma-1)\rho E$, where γ varied as pressure changes.

Using the new criteria, the amount of degassed carbon and sulfur have been estimated from Chicxulub impact and their effects on the global temperature have been calculated and discussed. The global warming caused by the degassed CO_2 is 0.2-1.1°C and the degassed SO_2 may caused a global cooling of is 8.5-16°C.

Shock temperature measurements place constraints on high-pressure equation-of-states, permit detection and quantification of phase transformations.

A high-sensitivity (24 mv/μW @850nm), time-resolved six-channel pyrometer has been designed and constructed and used in shock temperature measurements. Due to the high gain of the system, small mineral samples (~5 mm in diameter) can be used in shock temperature experiments. Thermal conductivities of LiF and Al_2O_3 were measured, for the first time, using this new system, their values are 2-3 orders of magnitude less than theoretical values.

Table of Contents

List of Figures

List of Tables

Introduction

Alvarez et al. [1980] proposed that a global, impact-induced , dust cloud from the impact of an asteroid or comet drastically reduced solar insulation, and this caused the previously recognized mass extinctions of some 80% marine and terrestrial genera at the Cretaceous/Tertiary (K/T) boundary. This proposal has led to extensive studies of various impact-induced extinction mechanisms. Extinction mechanisms that have been proposed are: impact-generated H_2O and/or CO_2-inducing greenhouse global warming [Emiliani et al., 1981; O'Keefe and Ahrens, 1989], dust-induced global cooling [Alvarez et al., 1980; Pollack et al., 1983], nitric acid rain [Crutzen, 1987; Prinn and Fegley, 1987], global forest fires inducing solar insulation from soot [Wolbach et al., 1985], severe global radiative heating upon reentering of impact ejecta [Melosh et al., 1990] and global cooling from stratospheric H_2SO_4 aerosols induced by volatilization of SO_2 and SO_3 from anhydrite and gypsum at the impact site, Chicxulub, Yucatan, Mexico [Brett, 1992; Sigurdsson et al., 1992; Pope et al., 1994].

The Chicxulub impact structure has recently been recognized as the leading candidate for the crater(s) associated with the Cretaceous/Tertiary bolide [Hildebrand et al., 1991; Sigurdsson et al., 1991a; Sigurdsson et al., 1991b; Blum and Chamberlain, 1992; Swisher et al., 1992]. The dominance of calcium carbonate (calcite) and calcium sulfate minerals (anhydrite and gypsum) in the upper 3 km of the Chicxulub section (in the sequence of limestone, anhydrite-dolomite conglomerates, limestone-dolomite and anhydrite-gypsum layers [Koeberl, 1993]) has prompted active research on the effects of their devolatilization upon impact [Chen et al., 1994; Brett, 1992; Sigurdsson et al., 1992; Pope et al., 1994].

In Chapter 1, shock vaporization experiments were carried out for porous (70% crystal density) anhydrite up to 76 GPa. Velocity histories of aluminum-LiF window

interface were measured using velocity interferometer system for any reflector (VISAR) [Duffy, 1992; Barker and Hollenbach, 1972].

Thermodynamic calculations of incipient and complete reaction criteria for porous and crystal density anhydrite have been carried out using two methods. The first method is the one previously used by many authors in which no chemical bonds are assumed to break upon shock compression. Chemical dissociation occurs only upon adiabatic release from shock states along the Hugoniot. The second method assumes incongruent break down of $CaSO_4$ to CaO, SO_2 and O_2 along the Hugoniot. The first method predicts much higher shock pressure values for devolatilization upon isentropic release. The shock pressure required for complete reaction from crystal anhydrite to CaO, SO_2 and O_2 is 280±23 GPa using first (no-break-down) method while the second (break-down) method predicts 155±13 GPa. The incipient vaporization pressure is 81±7 GPa for crystal anhydrite. For porous (70% crystal density) anhydrite, the incipient and complete vaporization pressures are 27±1 GPa and 67±6 GPa, respectively. The energy required for complete vaporization at high pressure is 13.2±0.85 MJ/Kg for crystal anhydrite, and 3.34±0.33 MJ/Kg for porous anhydrite. The anhydrite phase change energy at zero pressure is estimated as 0.085 MJ/Kg, which is negligible compared to the vaporization energy required at high pressure.

A Lagrangian one-dimensional wave propagation code (WONDY) [Kipp and Lawrence, 1982] was used to simulate the measured velocity profiles. We found that the vaporization criteria calculated assuming partial dissociation along the Hugoniot provides better agreement with the experimental profiles versus profiles calculated that do not take into account the dissociation reaction. The vaporized products can be described by an equation of the form $P=(\gamma-1)\rho E$, where γ varied from 1.73 to 2.5 for release from shock pressures of 25 to 76 GPa.

The thermodynamics of the reaction $2CaSO_4=2CaO+2SO_2+O_2$ appears to closely describe the observed particle velocity profiles and provides a decomposition mechanism

at relatively low energy levels (<6.43 MJ/Kg). Here the dominant gas is SO_2, but the reaction $CaSO_4=CaO+SO_3$ may be dominant at higher energy levels (>6.43 MJ/Kg) where the dominant gas is SO_3.

In Chapter 2, the same experimental and analytical methods as used in Chapter 1 were applied to calcite. Porous calcite (54% crystal density) was shocked up to 19 GPa. For porous calcite, the incipient vaporization pressure is 5.4±1.9 GPa. And the shock pressure required for complete vaporization is 24.5±6 GPa, using the no-break-down method, while the break-down method predicts 14.6±3.8 GPa. For crystal calcite, the incipient vaporization pressure is 54±6 GPa and the complete vaporization shock pressures are 151±18 GPa (no-break-down method) and 102±12 GPa (break-down method). The break-down value, 102±12 GPa, is close to those predicted, but not achieved, in previous shock recovery results [Lange and Ahrens, 1986]. The energy required to complete vaporize crystal calcite is 2.6 MJ/Kg, which is much larger than the Calcite I—Calcite IV phase change energy, ΔE_{tr} =0.02 MJ/Kg.

As in Chapter 1, numerical simulation showed that the break-down criteria provide better agreement with the experimental profiles than the no-break-down criteria. The vaporized products can also be described by an equation of the form $P=(\gamma-1)\rho E$, where γ varied from 5.4 to 3.4 for release from pressures of 8.7 to 19 GPa.

In Chapter 3, using the criteria obtained in Chapters 1 and 2, the amount of degassed carbon and sulfur have been estimated for the Chicxulub impact and their effects on the global temperature have been calculated and discussed. The global warming caused by the degassed CO_2 is 0.2-1.1°C and the global cooling introduced by the degassed SO_2 is 8.5-16°C after the Chicxulub impact. We conclude that impact-induced sulfuric acid aerosols may caused severe environmental stress by decreasing solar radiation incident on the Earth for several months to years as suggested by Pope et al. [1994]. The impact-induced CO_2, on the other hand, may cause a long-term ($>10^3$ years) global warming of ~1°C which is unlikely to have produced mass extinctions.

In the field of high-pressure geophysics, there have been great interest in measuring the temperatures of Fe, Fe compounds and alloys, Earth mantle minerals under shock pressures up to ~300 GPa [e.g., Yoo et al., 1993; Ahrens et al., 1990]. Because temperature measurements place constraints on high-pressure equation-of-states, these permit detection and quantification of phase transformations and thus provide data needed to describe both evolution of heat from the core as well as constrain mantle convection modeling [e.g. Tackley et al., 1994].

In Chapter 4, a high-sensitivity (24 mv/μW @850nm), time-resolved six-channel pyrometer has been designed and constructed and used in shock temperature measurements. Due to the high gain of the system, small mineral samples (~5 mm in diameter) can be used in shock temperature experiments. The employment of a field lens in the light path of the system and the random packing of the glass fiber bundle insures that the temperature measured is an average over the whole viewed area of the sample and thus is insensitive to flaws in minerals. Thermal conductivities of LiF and Al_2O_3 were measured, for the first time, using this new system, their values are 2-3 orders of magnitude less than theoretical values which were previously used for shock temperature measurements for Fe [Bass et al., 1987].

Chapter 1

Shock Vaporization of Anhydrite

1.1 Introduction

The impact of a large bolide, exactly at the Cretaceous/Tertiary (K/T) boundary, is now widely believed to account for world-wide mass extinction of many marine and terrestrial biota [Alvarez et al., 1980; Bohor et al., 1984; McHone et al., 1989]. The Chicxulub impact structure has recently been recognized as the crater associated with this bolide [Hildebrand et al., 1991; Sigurdsson et al., 1991a; Sigurdsson et al., 1991b; Blum and Chamberlain, 1992; Swisher et al., 1992]. The presence of thick deposits of anhydrite ($CaSO_4$) and gypsum ($CaSO_4 \cdot 2H_2O$) in the geological section at the Chicxulub site in NW Yucatan, Mexico, has raised the possibility that enormous amounts of SO_2 and/or SO_3 were released into the Earth's atmosphere during the formation of the Chicxulub impact crater [Brett, 1992; Sigurdsson et al., 1992]. These suggestions have led to active studies of shock vaporization of calcium sulfate ($CaSO_4$). Chen et al. [1994] studied shock-induced devolatilization of anhydrite, gypsum and mixtures of anhydrite and silica (SiO_2), they found that anhydrite did not decompose up to 42 GPa, which is the highest pressure in their recovery experiments, and gypsum only released its water content. Gerasimov et al. [1994] vaporized gypsum and anhydrite using a pulsed Nd-glass laser and studied the composition of the condensed vapor layer deposited onto a Ni foil. Gerasimov et al. suggested that a simple decomposition mechanism:

$$CaSO_4 \rightarrow CaO + SO_3 \qquad (1.1)$$

took place rather than the reaction

$$2CaSO_4 \rightarrow 2CaO + 2SO_2 + O_2 \qquad (1.2)$$

In this study, vaporization experiments using porous anhydrite (70% of crystal density) up to 76 GPa are reported. We employed porous anhydrite disk samples that were impacted by flyer plates. An aluminum witness plate was placed in vacuum at a stand-off distance behind the sample. The shocked sample material, upon adiabatic expansion, impacted an aluminum witness plate. The velocity history of the witness plate was monitored using a lithium fluoride (LiF) window via a velocity interferometer (VISAR) [Barker and Hollenbach, 1972]. This technique is distinctly different than the solid recovery method, as it is not limited by the pressure range from which recovery assemblies can survive and provides a methodology for monitoring volatilization of samples after impact. The VISAR measurements thus provide a quantitative description of dynamic process of shock vaporization. A one-dimensional Lagrangian finite-difference wave code, WONDY [Kipp and Lawrence, 1982], was used to fit the experimental VISAR results. Combined with thermodynamic calculations, that provide incipient and complete vaporization criteria and a vapor equation of state, the chemical decomposition reactions within the sample in space and time may be inferred. A similar type of experimental assembly has been used by Trucano and Asay [1987] to study the cadmium vaporization under high-velocity impact. This study is the first attempt to use this technique to study the vaporization of a polyatomic material for which incongruent vaporization reactions take place.

1.2 Experiments

Samples

The starting materials of this study were natural anhydrite (Farady mine, Farady Township, Hastings County, Ontario, Canada) and gypsum (New York) crystals. Both of them were first ground in a mortar to powders with sizes less than 100 μm, then mixed with each other (80% anhydrite, 20% gypsum). Gypsum powder was used to stick the anhydrite particles together since they are too " dry " to bond together. The powder mixture was compressed into disks 1.5-2.6 mm thick and 31 mm in diameter using a stainless steel mold under a pressure of 4.9 MPa for 10 minutes. The structural and absorbed water content was released upon heating the sample disks at 170 °C in a vacuum oven for 12 hours. The density of the final samples was 2.09 ± 0.04 g/cm^3, which is 70% of crystal density of anhydrite. After exposure to air for two weeks in the laboratory, the sample disks absorbed ~0.6% by weight of water. This water content is approximately the water content of the anhydrite powder ground from the natural anhydrite crystal in air.

Dynamic Loading System

The porous anhydrite samples were shock loaded using gun-launched impactors. To achieve shock pressures of up to 40 GPa, a 40-mm-bore propellant gun was employed. A 25 mm, two-stage light-gas gun was employed at higher pressures in one experiment. For the 40 mm gun experiments, the projectile mass is ~100 grams. These projectiles were constructed using a lexan sabot with a variable mass and thickness, 32 mm-diameter-flyer-plates mounted on their face. The projectiles were accelerated along a 8 m-long-gun barrel that extends into an evacuated chamber (~100 μmHg) containing the target assembly. Impact velocities between 1.0-2.5 km/sec are achievable. For the 25 mm bore two-stage light-gas gun, the projectiles mass is ~20 grams and an impact velocity of 5.1 km/sec was employed in one experiment. Using the 40 mm gun, projectile velocity is determined to ~0.5% precision using both double-exposure flash X-ray photography and time interval counters triggered by laser beam interrupts. The flash radiography system

for the two-stage light-gas gun achieves precision of ~0.5% in velocity determination. Detailed descriptions of experimental apparatus for achieving one-dimensional planar shock loading can be found elsewhere [Ahrens et al., 1971; Ahrens, 1987]. The target assembly (Figure 1.1) employed flyer plate and driver materials of aluminum 6061 (Al6061), 304 stainless steel (304 S. S.), copper (Cu) or tungsten (W). Table 1.1 lists the experimental parameters of these materials used in the anhydrite experiments.

Interferometry

The primary diagnostic technique used in this study was the velocity interferometer system for any reflector (VISAR) [Barker and Hollenbach, 1972]. VISAR works on the principle that an incident beam of laser light is reflected from a surface within the target and its motion induces a Doppler shift in reflected laser light. The reflected light is then split into two equal intensity beams in a modified Michelson interferometer in which one of the beams is delayed (1-2 ns) upon passage through an etalon and then superposed with the other beam. Superposition of the two beams induces interference fringes. Each interference fringe indicates a change in velocity. Integration of fringe versus time data yields the velocity history of the reflecting surface. A schematic of the VISAR setup is shown in Figure 1.2. The interference fringes form from a diffuse (spatially incoherent) source [Zwick and Shepard, 1971]. The VISAR used in this study was constructed by Duffy [1992]. It is similar to that originally described by Barker and Hollenbach [1972] but incorporates the push-pull modification and data reduction scheme of Hemsing [1979]. It was recently up-dated using fiber optics [Barker, 1994]. The laser beam propagates to the experimental assembly via an optic fiber leading to the target chamber. The laser beam is then focused via a small lens onto the diffused target surface, the reflected diffused light is collected using another lens and focused into an adjacent optic fiber and returned to interferometer. The focusing and collection of light are conducted

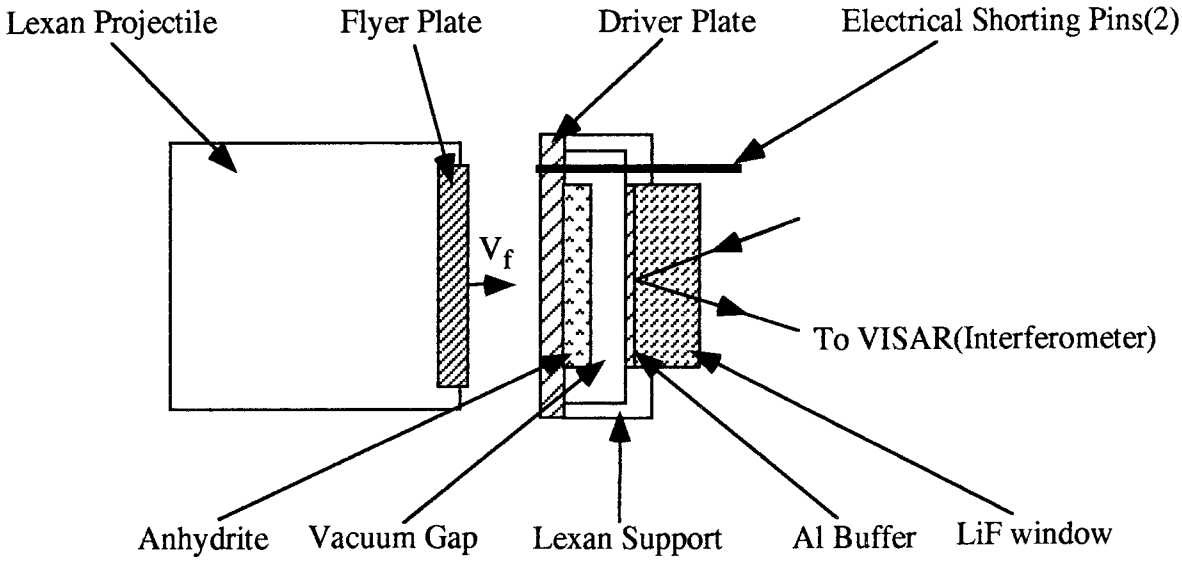

Figure 1.1 Experimental configuration, shock vaporization experiments, anhydrite.

Table 1.1 Experimental Parameters of Anhydrite Experiments

Shot No.	Flyer Plate Thickness (mm) (Material)	Impact Velocity (km/sec)	Driver Plate Thickness (mm) (Material)	Sample Thickness (mm)	Sample Density (Kg/m^3)	Gap (mm)	Al6061 Buffer Thickness (mm)	LiF Window Thickness (mm)
975	3.763±0.003 (Al6061)	1.98±0.02	0.988±0.003 (Al6061)	2.55±0.05	2120±40	1.00±0.05	1.001±0.003	12.000±0.002
971	3.856±0.003 (304 S. S.)	2.46±0.02	0.879±0.005 (304 S. S.)	2.66±0.03	2090±30	2.68±0.03	0.917±0.002	12.000±0.001
970	3.922±0.003 (W)	2.49±0.02	1.979±0.008 (304 S. S.)	2.61±0.04	2090±30	3.61±0.04	0.963±0.001	12.100±0.005
294	1.5697±0.0025 (Cu)	5.08±0.04	0.4216±0.0024 (Cu)	1.547±0.029	2090±40	1.62±0.03	1.016±0.004	8.130±0.003

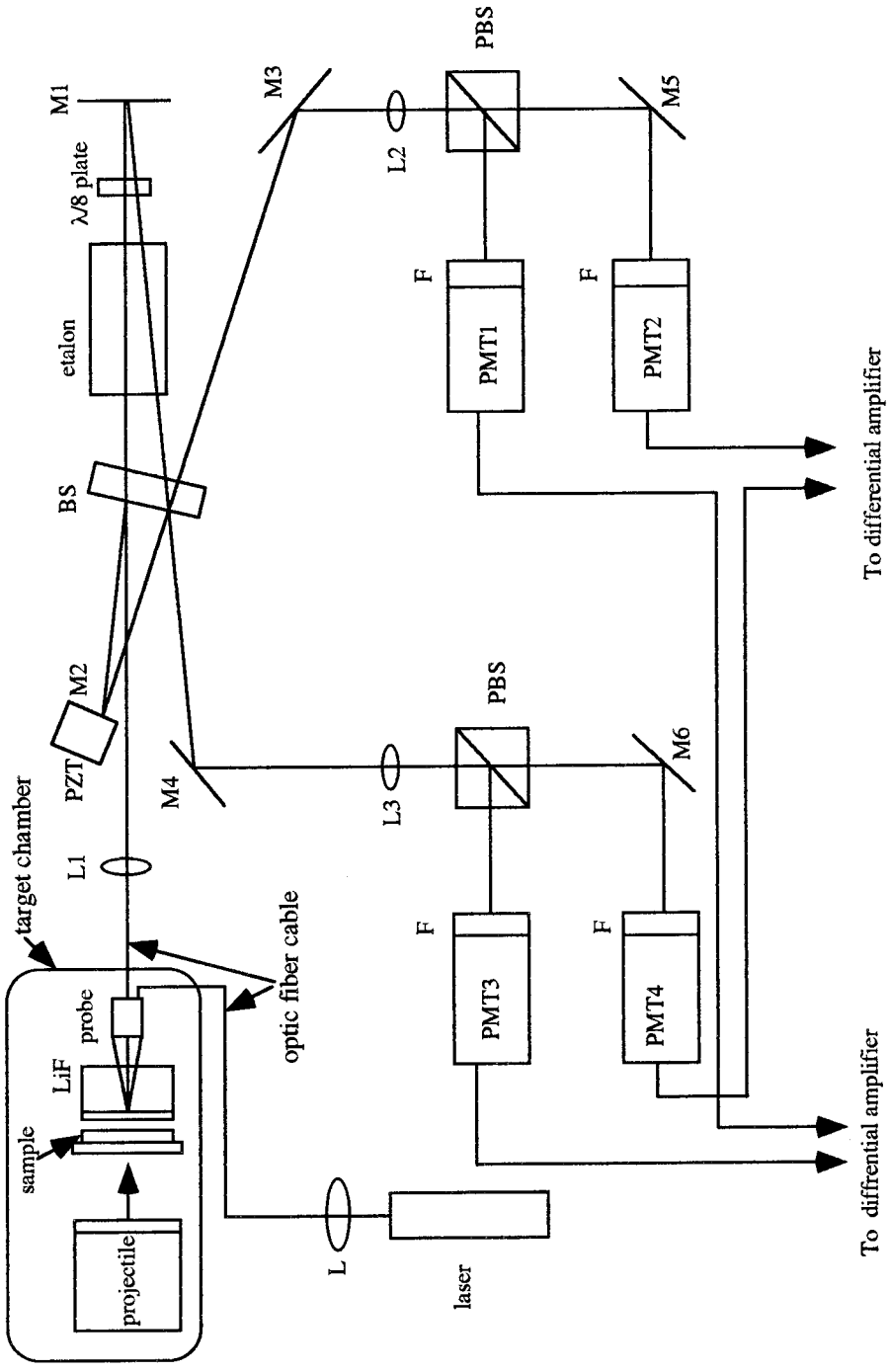

Figure 1.2 Velocity interferometer system for any reflector (VISAR). Designation M is mirror, L is lens, BS is beam splitter, PBS is polarizing cube beam splitter, F is narrow bandwidth (10 nm) laser-line interference filter, and PMT, photomultiplier tube (Burle 7764). PZT is piezoelectric translator attached to mirror which is mounted in precision angular orientation device. Probe is device which focuses laser light onto target and collects reflected light back into interferometer.

immediately adjacent to the target via a fiber optic probe (Figure 1.3) [Barker, 1994]. The deployment of optic fibers and the probe makes the alignment of the experiments an efficient operation as described below. A 3 Watt Ar^+ laser (Lexcel 95-3) provides the laser light source. The light returned to the interferometer is collimated by lens, L1. The beam splitter, BS, together with mirrors, M1 and M2, provides laser beam splitting , delay, and recombination. Fused silica etalons (up to 19 cm in the present VISAR) provide the required delay (< 2 ns). They are placed in the right leg. M1 is then translated manually during VISAR set-up such that the apparent distance to each mirror as seen by the photo-multiplier detector are equal. Upon recombination at the beam splitter, BS, interference fringes are generated and directed to the four photomultipliers (PMT's) (Burle 7764). The one-eighth ($\lambda/8$) wave-plate in the delay leg introduces a 90° phase shift between the s- and p-polarized components of the returned light. Polarizing beam splitter cubes (PBS) separate the p- and s-components of the beam and direct them to different PMT's for separate recording.

A separate recording of the p- and s-components has two advantages: First, it can be shown that ambiguities in the sign of the acceleration are removed by this process [Barker and Hollenbach, 1972]. When sign of the acceleration reverses, the leading polarization component reverses as well. Secondly, the loss of velocity resolution near fringe peaks and troughs is eliminated since when one component is near a fringe peak, the other is near its midpoint (where velocity resolution is maximized). The interference patterns traveling to the left and right of the beam splitter are 180° out-of-phase due to phase shifts upon reflection. These are recorded by separated PMT's and subtracted from each other using differential amplifiers (Comlinear Inc., 1 GHz bandwidth, model s-1500) to cancel non-interfering stray light and to double the signal levels. This is known as the push-pull VISAR modification [Hemsing, 1979]. The use of a differential amplifier has the additional benefit of conserving oscilloscope channels and providing more redundancy in oscillographic recording with different sensitivity and sweeping speeds.

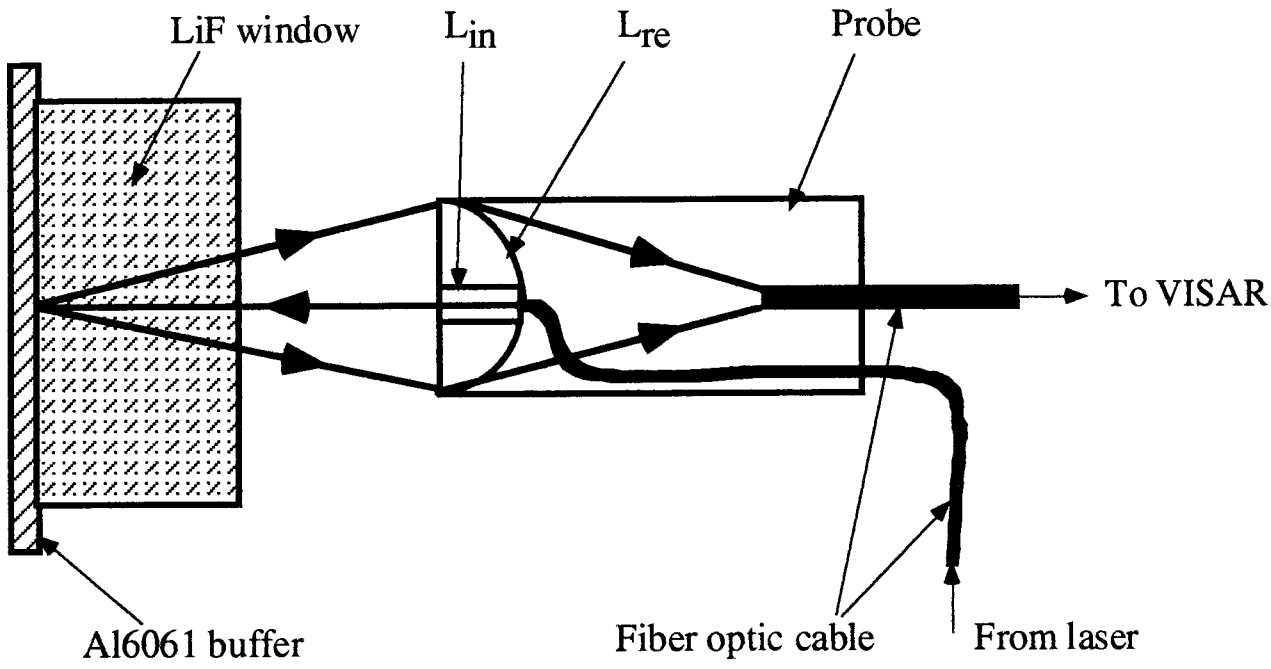

Figure 1.3 Fiber optic probe. L_{in}, focuses the incident laser onto the diffuse reflecting surface, L_{re}, collects the reflected light.

The fringe signals from the differential amplifiers are recorded by digital oscilloscopes (HP 54111D). Narrow bandwidth (10 nm) interference filters (F) are mounted in front of each PMT to filter out extraneous light generated during the experiment and allowing operation of the system with the room lights on.

The piezoelectric translator (PZT) is attached to M2 and, when driven at high voltage, continuously changes the path between the beam splitter, BS, and M2, resulting in a slowly (~1 kHz) varying fringe pattern which is used during alignment of the VISAR.

The relationship between the reflector velocity, u, and the fringe count, F, is given by [Barker and Hollenbach, 1972]:

$$u(t-\tau/2) = kF(t) \tag{1.3}$$

where k is the fringe constant which is given by [Barker and Schuler, 1974]:

$$k = \lambda_o/(2\tau)/(1+\Delta\nu/\nu_o)/(1+\delta) \tag{1.4}$$

where the incident laser wave length, λ_o=514.5 nm, and $(1+\delta)$ is a correction term due to the dispersion in the etalons [Barker and Schuler, 1974]:

$$\delta = -\frac{n_o}{n_o^2-1}\lambda_o\left(\frac{dn}{d\lambda}\right)_{\lambda=\lambda_o} \tag{1.5}$$

Here n_o is the index of refraction of fused silica etalon at λ_o=514.5 nm, and $(1+\delta)$=1.0339 is determined at λ_o=514.5 nm using index versus wavelength data [Malitson, 1965].

The $(1+\Delta\nu/\nu_o)$ is a correction term that accounts for the change in the refractive index of the shock-compressed window materials and generally is a function of shock pressure (or particle velocity) [Barker and Hollenbach, 1970]. Here ν_o is the fringe frequency of the reflected light if no window was present and $\Delta\nu$ represents the correction due to strain induced changes in the window refractive index. For a LiF window, the correction term $(1+\Delta\nu/\nu_o)$ equals a constant, 1.281±0.009, up to 115 GPa, which is calibrated by Wise and Chhabildas [1986]. (This differs markedly to the behavior of other window materials where $\Delta\nu/\nu_o$ varies with strain.)

The delay time τ is determined from

$$\tau = 2h/c/(n - 1/n) \qquad (1.6)$$

where h is the etalon thickness, n is the etalon refractive index, and c is the speed of light. The refractive index for the present etalon is n=1.468±0.003 [Duffy, 1992].

Velocity histories are extracted from the interferometer records using the program VISAR91 [Duffy, 1992] which is a modified version of the program VISAR88 [Barker, 1988] with the algorithm we used for the velocity calculation written by Hemsing [1983]. The velocity is determined using the equation:

$$V(t) = k(\arctan(\frac{d2(t) - d1(t)\cos\phi}{d1(t)\sin\phi}) - \psi_o) \qquad (1.7)$$

where d1(t) and d2(t) are the normalized signal amplitudes of the two data channels, $\phi \approx 90°$, is the phase angle between the two channels, about 90^o, Ψ_o is the initial random phase. This data reduction method is insensitive to signal intensity fluctuations and is therefore more appropriate for a push-pull VISAR, in which, for the present instruments, the beam intensity is not explicitly monitored. The shock arrival at the buffer-LiF interface, in the present experiments, produced a burst of fringes at too high a frequency to be tracked by the ~500 MHz recording system. The change in interference velocity at this point can be determined reliably from the known impact velocity, and approximate knowledge of the equations of state of the target and flyer plate materials, and the signal intensity levels before and after the velocity jump [Barker and Hollenbach, 1972; Barker, 1988]. More details on interferometers for shock wave profile measurements and data reduction methods are described by Duffy [1992].

Target Assembly

As illustrated in Figure 1.1, the target assembly consists of a driver plate, sample, aluminum buffer, lithium fluoride (LiF) window (Solon Technologies, Inc.), electrical shorting pins, and a lexan support. Upon impact by the flyer plate, a shock wave is driven

through the driver plate and then a shock propagates into the sample. The shocked sample material move across the vacuum gap and strikes the aluminum buffer. The velocity history of the buffer-LiF interface is then recorded by VISAR via the LiF window. The electrical shorting pins (Dynasen Corp., ca-1038) are small electrical switches in which two conductors are separated by a small air gap (0.635±0.012 mm) which is closed mechanically upon impact of the flyer plate. Upon closing of the shorting pins, an electrical pulse is generated by a circuit [Duffy, 1992] that triggers the oscilloscopes. The purpose of the LiF window is to match the impedance of the buffer in order to obtain a wave profile as close as possible to that propagating through the buffer and prevents a rarefaction wave from propagating back into the buffer and sample material from right to left in Figure 1.1. The reflecting surface of the buffer is a diffuse optical surface. Its reflectivity is not expected to change dramatically when shock wave strikes it. The LiF window is epoxied to the buffer with Eastman-Kodak #910 adhesive.

1.3 Thermodynamic Calculations

Shock States Calculation for Porous Anhydrite

The equation of state of porous anhydrite had not been measured. In order to calculate the shock pressure in the porous anhydrite, its Hugoniot equation of state was constructed theoretically using literature data for solid polycrystalline anhydrite [Simakov et al., 1974] and the Grüneisen equation of state as discussed below. We start from the conservation relations for a shock wave propagating into a material at rest, they are as follows:

conservation of mass:

$$\rho_o U_S = \rho_h (U_S - U_p) \tag{1.8}$$

conservation of momentum:

$$P_h=\rho_o U_s U_p \tag{1.9}$$

conservation of energy:

$$E_h-E_o=P_h(V_o-V_h)/2 \tag{1.10}$$

where U_s is shock wave velocity, U_p is particle velocity behind the shock, P_h is shock pressure, V_o and V_h are the initial and shock state specific volumes, respectively. ρ_h is shock state density, E_h is shock state internal energy, ρ_o and E_o are initial density and internal energy, respectively. E_o is usually chosen as zero for convenience.

With these conservation equations, the Grüneisen equation of state is used to obtain values for the porous Hugoniot states, P_d and E_d, using the solid Hugoniot state (P_h, V) at volume, V, as the reference:

$$E_d-E_h=(V/\Gamma)(P_d-P_h) \tag{1.11}$$

where Γ is Grüneisen parameter. The porous Hugoniot in the P-V plane can be found as [Zeldovich and Raizer, 1966]:

$$P_d=P_h[(V_{oc}-V)/2-V/\Gamma)]/[(V_{od}-V)/2-V/\Gamma)] \tag{1.12}$$

where V_{oc} is initial specific volume of crystal anhydrite, V_{od} is initial specific volume of porous anhydrite. The crystal density anhydrite Hugoniot was determined by Simakov et al. [1974]. Here V/Γ is assumed as a constant during the calculation [Rice et al., 1958].

The shock wave velocity, U_s, and particle velocity, U_p, can be found as:

$$U_s=V_{od}[P_d/(V_{od}-V)] \tag{1.13}$$

$$U_p=[P_d(V_{od}-V)]^{1/2} \tag{1.14}$$

Values of U_s and U_p were calculated for porous anhydrite from the data of Simakov et al. for crystal anhydrite in the pressure range of 10 to 25 GPa.

For solids, in regions of no phase change, the shock wave velocity, U_s, and particle velocity, U_p, has a linear relationship as [Ruoff, 1967]:

$$U_s= C_o+SU_p \tag{1.15}$$

where C_o and S are material constants. C_o equals the bulk sound speed at zero pressure for crystal density materials. Using U_s and U_p obtained from Eqs. 1.13 and 1.14, values

Table 1.2 Shock States of Porous Anhydrite Samples

Shot No.	ρ_o (Kg/m^3)	P_h (GPa)	E_h (MJ/Kg)	ΔS_h (KJ/Kg/K)	R_f (%)
975	2120±40	12.9±0.5	0.75±0.03	1.31±0.11	0.0
971	2090±30	25.2±1.1	1.76±0.08	2.04±0.16	0.0
970	2090±30	37.5±1.6	2.85±0.13	2.52±0.21	24.9±2.1
294	2090±40	75.9±3.2	6.43±0.29	4.12±0.35	100

ρ_o is initial density, P_h is Hugoniot pressure, E_h is Hugoniot energy, ΔS_h is entropy increase, R_f is percentage of reacted material.

Table 1.3 Shock Equation of State Parameters

Material	ρ_0 (g/cm^3)	C_0 (km/sec)	S	Γ_0	ν_0	Y_0 (GPa)	Refs.
W	19.2	4.04±0.01	1.23±0.004	1.54	0.28	2.4	a
Cu	8.924	3.91±0.01	1.51±0.01	1.96	0.34	0.2	a
304 S. S.	7.87±0.02	4.58±0.01	1.49±0.01	2.2	0.29	0.2	a, b
Al6061	2.683±0.003	5.35±0.06	1.34±0.02	2.1	0.34	0.2	a
LiF	2.64±0.02	5.15±0.03	1.35±0.01	1.6	0.22	0.2	a
Lexan	1.19±0.01	2.42±0.03	1.32±0.11	1.64	-	-	a
Anhydrite (Low-Pressure-Phase)	2.97	3.60±0.06	1.75±0.05	2.50	-	-	c
Anhydrite (High-Pressure-Phase)	3.68	3.25±0.11	1.72±0.03	2.44	-	-	c
Anhydrite (Porous)	2.09±0.04	2.41±0.08	2.16±0.04	2.50	-	-	d

ρ_0 is density, C_0 and S are shock wave equation of state (EOS) constants, Γ_0 is Grüneisen parameter, ν_0 is Poisson's ratio, and Y_0 is yield strength. References: a, Marsh [1980], b, Duffy [1992]; c, Simakov et al. [1974]; d, this study; densities for crystal anhydrite (high- and low-pressure phases) are from Simakov et al. [1974] and Γ_0 is obtained using Eq. 1.28.

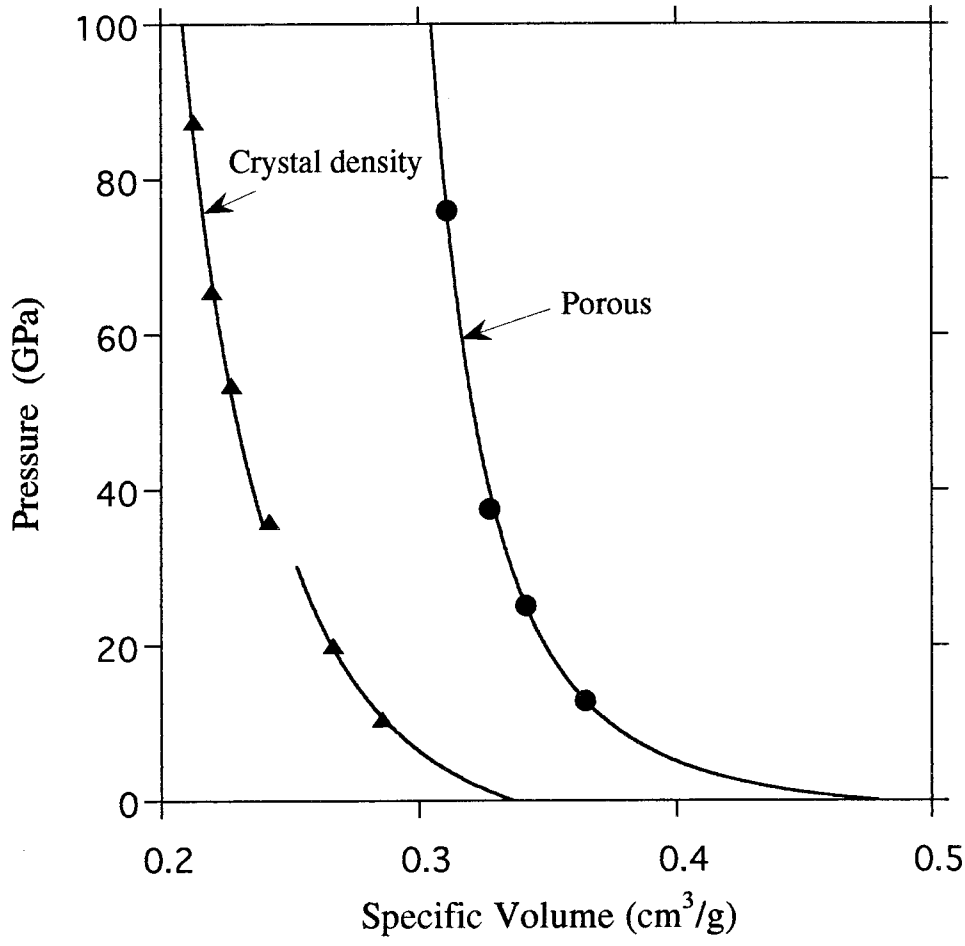

Figure 1.4 Hugoniot relation of porous and crystal density anhydrite in P-V plane. Parameters used to calculate Hugoniot curves are given in Table 1.1 and 1.3. Circles represent experiments (Table 1.2) and triangles are data from Simakov et al. [1974]. LPP refers to low-pressure-phase and HPP to high-pressure-phase.

C_0 and S were obtained by fitting Eq. 1.15. However, for porous media, C_0 and S have no simple physical meaning and Eq. 1.15 is a poor approximation for porous media. Although this is the case, and a phase change in the solid occurs, we used the parameters listed in Table 1.3 in the present study.

The impedance match method [Ahrens, 1987] was used to calculate the shock state parameters in the sample from the measured flyer-plate velocity and equation-of-state (EOS) parameters of the flyer plate, driver plate and the sample. Shock states for the present experiments are given in Table 1.2 and the EOS parameters used are listed in Table 1.3. Figure 1.4 shows both Hugoniots of crystal and porous anhydrite in P-V plane. The circles represent the calculated states accessed by the present experiments.

Incipient and Complete Reaction Criteria Calculations

In the study of shock-induced vaporization (or reaction), the incipient and complete reaction criteria are of great interest. Unfortunately, there are no previous measurements of the release path of the shocked anhydrite. Thus the thermodynamic parameters along the release path are not directly available. However, the entropy method [Zeldovich and Raizer, 1966; Ahrens, 1972] can be applied. This method calculates entropy along the Hugoniot and then compares it with the entropy required to initiate and completely vaporize a material at ambient pressure and high temperature. The latter data are usually tabulated (e.g., Robie et al., 1979). The assumptions of this method are that all the entropy production takes place during the shock process, and during the rarefaction process the specific entropy remains constant.

The reaction we considered is:

$$CaSO_4 \rightarrow CaO + SO_2 \uparrow + \frac{1}{2} O_2 \uparrow \qquad (1.16)$$

Since the gas phases, SO_2 and O_2, are more stable, at 10^5 Pa and high temperature, than that achieved by the reaction:

$$CaSO_4 \rightarrow CaO + SO_3 \uparrow \qquad (1.17)$$

at 10^5 P_a and high temperature, we consider reaction 1.16 rather than 1.17 [Robie et al., 1979].

The entropy increase required for incipient reaction is:

$$S_{IR} = \int_{T_o}^{T_{IR}} \frac{C_p}{T} dT \qquad (1.18)$$

where T_o is ambient temperature, T_{IR} is the incipient reaction temperature at which the sums of Gibbs formation energies for the reactants and products are equal, C_p, which is a function of temperature, is the heat capacity at atmospheric pressure [Robie et al., 1979].

The excess entropy required for complete reaction is:

$$S_{CR} = S_{IR} + \Delta S \qquad (1.19)$$

where ΔS is the entropy difference between products and reactants at T_{IR}.

The entropy calculation along the Hugoniot is illustrated in Figure 1.5, entropy gain in the shocked state (and in the post-shock state assuming isentropic release) is:

$$\Delta S_h = \Delta S_{tr} + \int_{T_s}^{T_h} \frac{C_v}{T} dT \qquad (1.20)$$

where ΔS_{tr} is the entropy change from low pressure phase (LPP) to high pressure phase (HPP) at zero pressure (path I) and is given by:

$$\Delta S_{tr} = S_{HPP} - S_{LPP} \qquad (1.21)$$

$$T_s = T_o \exp[\Gamma(1 - V/V_o)] \qquad (1.22)$$

where T_s is the temperature of isentropic compression from initial volume V_{oh} (HPP) at temperature T_o to Hugoniot volume V_h at isentropic pressure P_s (path II), Γ is the Grüneisen parameter, and Γ/V=constant is assumed.

The Hugoniot temperature is determined by (path III):

$$\int_{T_s}^{T_h} C_v dT = E_h - E_s - \Delta E_{tr} \qquad (1.23)$$

where ΔE_{tr} is phase transition energy at ambient pressure and temperature corresponding to the change in entropy, ΔS_{tr}.

The Hugoniot energy is given by (path IV):

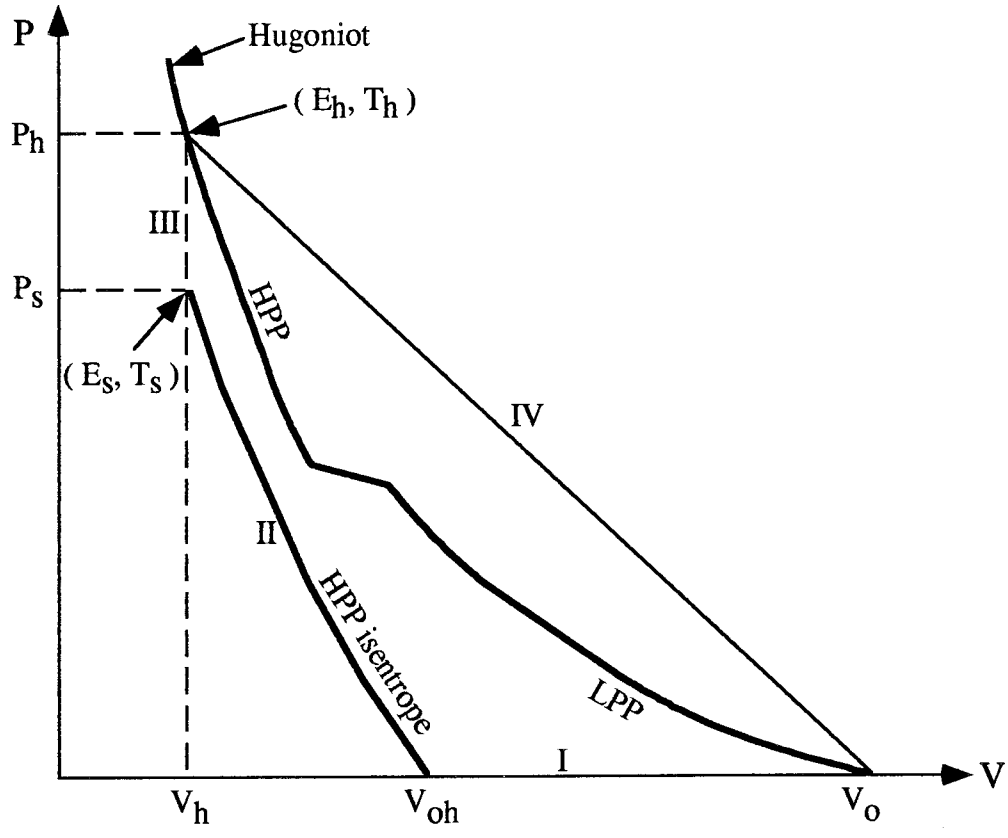

Figure 1.5 Thermodynamic calculation paths in P-V plane.

$$E_h = \frac{1}{2} P_h (V_o - V_h) \tag{1.24}$$

The isentropic energy is given by (path II):

$$E_s = -\int_{V_{oh}}^{V_h} P_s dV \tag{1.25}$$

The isentropic pressure is given by the Murnaghan equation (path II):

$$P_s = \frac{K_{os}}{K'_{os}} [(\frac{V_{oh}}{V_h})^{K'_{os}} - 1] \tag{1.26}$$

And the Hugoniot pressure is given by:

$$P_h = \frac{C_o^2 \eta / V_o}{(1 - S\eta)^2} \tag{1.27}$$

where $\eta = 1 - V/V_o$, K_{os} is crystal density bulk modulus and $K_{os}'=(\partial K/\partial P)_{s,\ p=0}$, their values are determined using the data of Simakov et al. [1974] as 38.5 GPa and 6.0 for low-pressure-phase (LPP), 161.8 GPa and 4.4 for high-pressure-phase (HPP) employing also the theoretical relations [Ruoff, 1967]:

$$K_{os}=\rho_{oc} C_o^2 \tag{1.28}$$

$$K'=4S-1 \tag{1.29}$$

The reaction fraction is given by

$$R_f=(\Delta S_h - S_{IR})/(S_{CR} - S_{IR}) \tag{1.30}$$

In the above formulation, it should be pointed out that no chemical reaction is taken into account, i.e., the Hugoniot energy is used to compress and heat the sample only, no energy is used to break the chemical bonds from the initial state to the compressed state on the Hugoniot. This is turns out to probably not be reasonable since once the shock temperature reaches the incipient reaction temperature, T_{IR}, chemical bonds will start to break, and the Hugoniot energy, in part, is consumed by breaking bonds rather than just heating up the sample. A simple and reasonable first-order approach is to assume that, during the calculation, once the Hugoniot temperature reaches T_{IR}, it will remain constant and all the unused Hugoniot energy, ΔE_{TIR}, will be consumed

only by chemical dissociation until the dissociation is completed. The entropy increase, ΔS_{TIR}, during this stage, is calculated by:

$$\Delta S_{TIR}=\Delta E_{TIR}/T_{IR} \qquad (1.31)$$

It is clear that from this equation, for the same point on Hugoniot (or the same amount of Hugoniot energy), more entropy will be generated in this sample than the case in which the Hugoniot energy is only consumed by heating the sample and the temperature rises continuously.

Radousky et al. [1986] has, in N_2 shock compression experiments, observed the Hugoniot temperature increase slowed down as N_2 molecules start to dissociate as shock pressure increase. Their result supports use of the present approach in which a constant breakdown temperature is assumed. Since, in reality, the Hugoniot temperature rises slowly instead of remaining constant in their experiments for pressures above the point where N_2 starts to dissociate, our constant temperature assumption provides a upper bound to the entropy increase. In this study, two computational approaches are employed and compared. The first method does not take the chemical dissociation into account and the second method does. We define these two methods as no-break-down and break-down method, respectively.

However, we recognize that rather than chemical dissociation or breakdown occurring, melting, probably incongruent, may instead be taking place. The entropy of melting of simple substances (e.g., monatomic substances consisting of particles having quasi-spherically symmetric atomic interactions) is associated with a fusion entropy change of on the order of the gas constant R (8.314 J/K/mole) [Stishov, 1974, 1988]. If we apply this simple rule to anhydrite, the entropy of melting of anhydrite at high pressure is about 0.37 KJ/Kg/K. This value is ~10% of the total entropy of vaporization and thus is relatively small compared to the entropy gain due to modest shock compression (Table 1.2). Thus shock melting may also be occuring and could be called upon to partially explain our experimental results. A hypothetical solid-liquid phase

boundary in the $CaSO_4$ is shown in Figure 1.6. The phase boundary is determined by connecting the incipient reaction points of porous and crystal density anhydrite and then extrapolating into the low- and high-pressure regions.

The incipient and complete reaction criteria for both crystal and porous anhydrite were calculated. For the porous case, we neglect possible phase changes for lack of data and assume $\Delta S_{tr}=0$. For crystal density anhydrite, shock experiments [Simakov et al., 1974] showed that there is a phase change starting at 30 GPa that is completed at 35 GPa along the Hugoniot. ΔS_{tr} of this phase change is estimated as 0.24 KJ/Kg/K. The estimation method is illustrated in Figure 1.7 using the isentropes of LPP and HPP. The thermodynamic path is chosen as V_{oc1}-A-B-C-V_{oc2}-V_{oc1}. V_{oc1}-A is isentropic compression along the LPP isentrope to 30 GPa, A-B is compression at constant pressure of 30 GPa, B-C-V_{oc2} is isentropic release along the isentrope of HPP, and V_{oc2}-V_{oc1} is from HPP to LPP at ambient pressure. The energy required for the phase change is the area surrounded by ABC since release from B-C is isentropic. It is 0.085 MJ/Kg (ΔE_{tr}) and the entropy change is estimated as $\Delta E_{tr}/T_s$, where T_s is the average temperature at A and B calculated using Eq. 1.22. Compared with the break-down energy, 13.2 MJ/Kg (Table 1.4), the phase transition energy, ΔE_{tr}, is very small.

Since there is no specific heat, C_v, data available at high pressure, the Dulong-Petit value, 3nR (where n is the number of atoms in one molecule of $CaSO_4$, R is the gas constant and its value is 8.31441 J/mol/K), was used in the calculation. The uncertainties introduced by this treatment were estimated by comparing the Dulong-Petit value with the tabulated values of C_p [Robie et al., 1979] at ambient pressure. The Dulong-Petit value (1.099 KJ/Kg/K) is larger than experimental values at low temperatures (0.732 KJ/Kg/K at 298.15 K) but smaller at high temperature (1.531 KJ/Kg/K at 1400 K).

The calculated incipient and complete reaction entropy, shock pressure are listed in Table 1.4. The incipient vaporization pressure of crystal anhydrite is 81±7 GPa. Compare to the recovery experimental data by Chen et al. [1994], this result is consistant

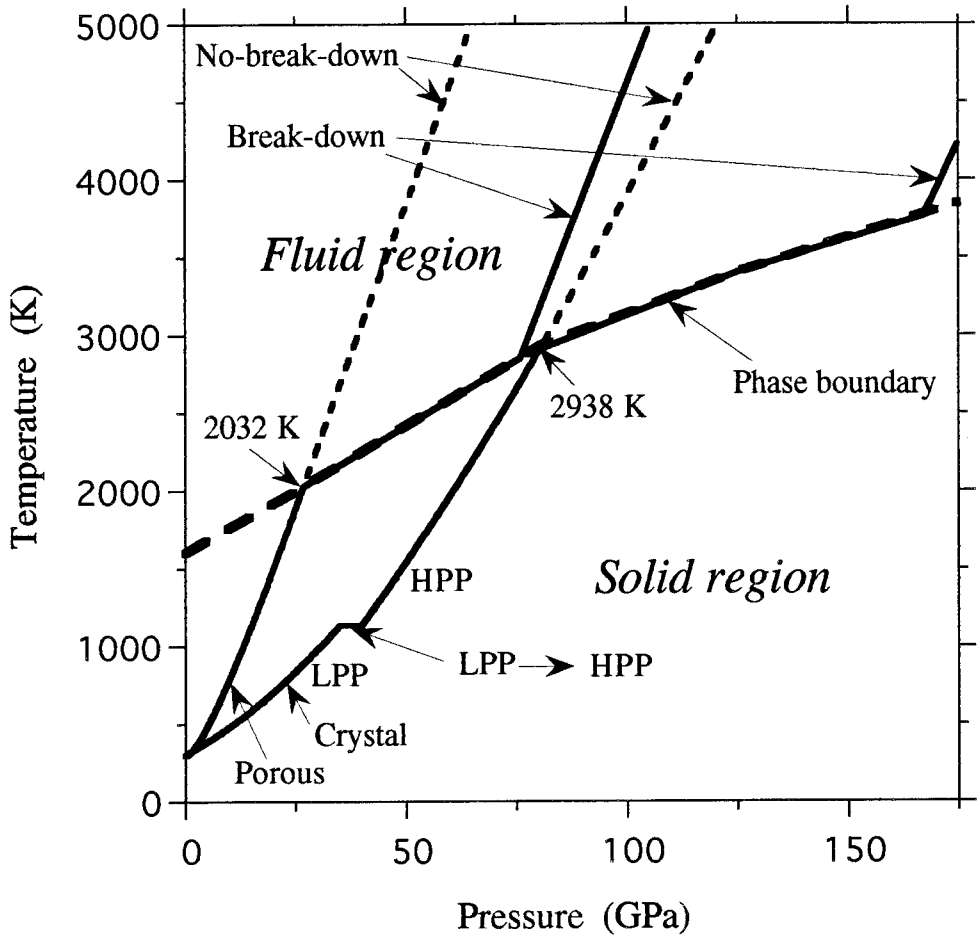

Figure 1.6 Shock temperature versus shock pressure of porous and crystal anhydrite. Break-down refers to calculation method taking into account chemical dissociation, no-break-down (dashed curves) refers to calculation without taking into account chemical dissociation.

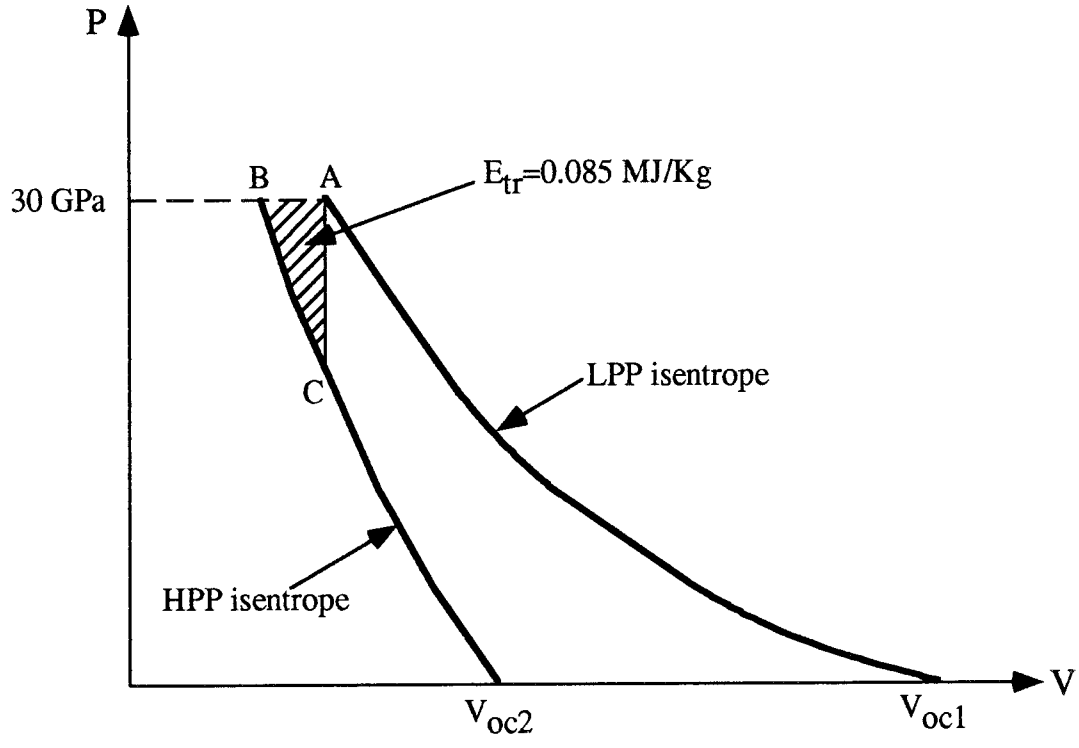

Figure 1.7 Estimation of entropy change from low-pressure-phase (LPP) to high-pressure-phase (HPP) anhydrite.

Table 1.4 Incipient and Complete Reaction Parameters

Material	ρ_O (Kg/m^3)	P_{hIR} (GPa)	P_{hCR} (GPa)	$(E_H-E_S)_{IR}$ (MJ/Kg)	$(E_H-E_S)_{CR}$ (MJ/Kg)	S_{IR} (KJ/Kg/K)	S_{CR} (KJ/Kg/K)
Anhydrite (Crystal)	2970	81.0±6.5	155±13	3.43±0.15	16.6±0.7	2.12±0.08	3.73±0.14
Anhydrite (Porous)	2090±40	26.9±1.1	67±6	1.91±0.09	5.25±0.24	2.12±0.08	3.73±0.14

ρ_O is initial density, P_{hIR} is incipient reaction Hugoniot pressure, P_{hCR} is complete reaction Hugoniot pressure, E_H is Hugoniot energy, E_S is isentropic energy, S_{IR} is incipient reaction entropy, S_{CR} is complete reaction entropy.

since they found no vaporization up to 42 GPa. Unfortunately, there is no recovery experimental results available above 42 GPa.

Figure 1.8 shows the calculated results of entropy gain versus Hugoniot pressure for both porous and crystal density anhydrite. The break-down method yields a steeper increase of entropy gain than the no-break-down method after the entropy gain reaches the incipient reaction value. The circles and crosses represent states calculated via impedance match method for the present experiments. Figure 1.9 shows the reaction percentage, R_f, versus shock pressure. It is clear that the no-break-down method yields a much higher shock pressure for complete reaction for both porous and crystal anhydrite. Circles and crosses represent the experiments and values obtained using break-down method are given in Table 1.2.

The uncertainties of shock pressure, shock energy (Table 1.2) come from the uncertainties of the initial density, equation of constants (Table 1.3) and the use of Dulong-Petit value for C_v. The uncertainties of the incipient and complete vaporization entropy (Table 1.4, Figure 1.8) are relatively small since they are obtained from well determined experimental data [Robie et al., 1979]. However, the actual uncertainties, could be larger because of the validity of assumptions in our thermodynamic calculations are not easily testable with regard to entropy increase calculations.

1.4 Results and Discussions

Velocity History Profiles

Four shots were conducted for porous anhydrite samples, the pressure ranged from 13 to 76 GPa, and the calculated reaction fraction from 0 to 100% (Table 1.2). Due to the complex wave interaction and chemical dissociation of the sample, the velocity profiles recorded have complex structures. Figure 1.10 shows all the profiles. The experimental

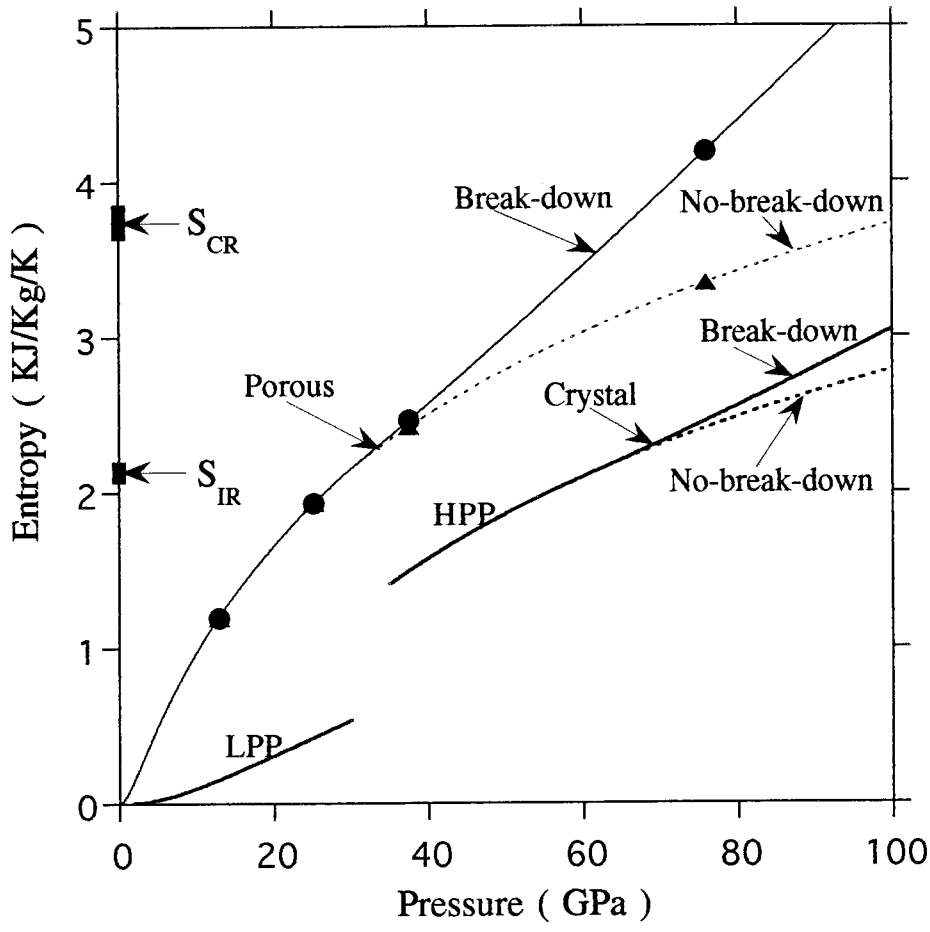

Figure 1.8 Porous and crystal density anhydrite entropy gain versus shock pressure. Break-down refers to calculation method where after entropy reaches incipient reaction entropy value (Table 1.4), shock temperature will not increase until the complete reaction entropy criteron is reached. No-break-down refers to method where shock temperature will continue to increase after entropy reaches incipient reaction value. Circles used break-down method, triangles used no-break-down method.

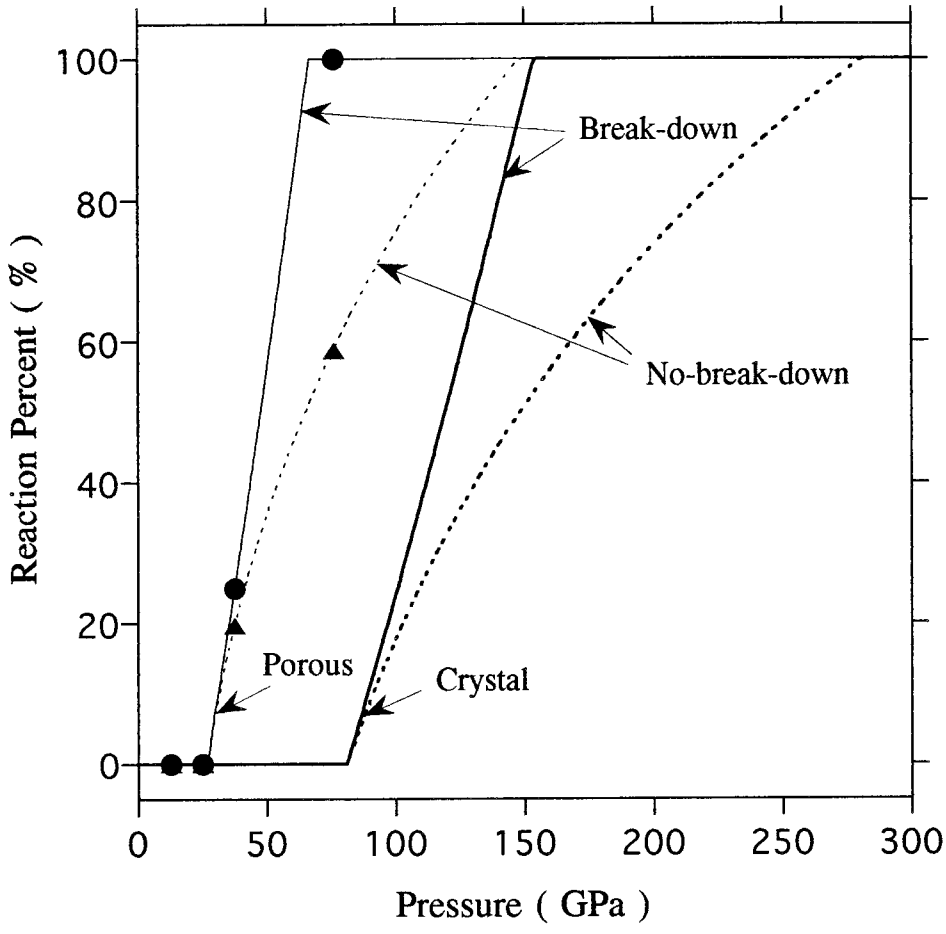

Figure 1.9 Reaction percent versus shock pressure for porous and crystal anhydrite. Break-down and no-break-down cases are shown.

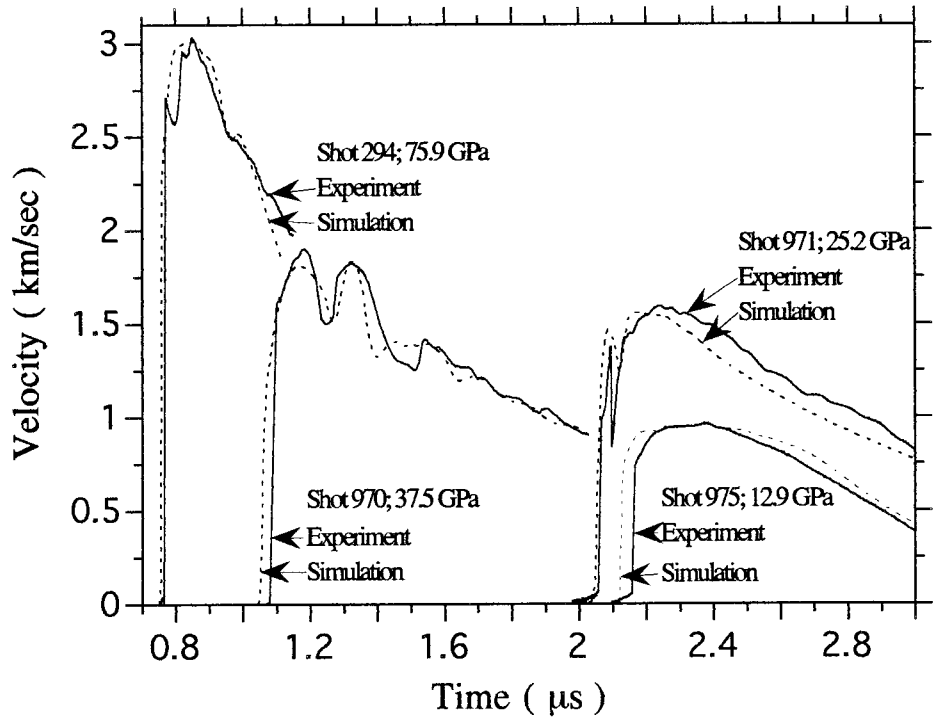

Figure 1.10 Experimental and numerical simulation for anhydrite. Times of experimental profiles are shifted to best present the results. The time of the simulation is uncertain by about ±50 ns.

conditions, shock states, and equation of states parameters are given in Table 1.1, 1.2 and 1.4.

Numerical Simulations

In order to better understand the dynamic behavior of anhydrite and to test whether the calculated thermodynamic criteria provide good descriptions for the impact process, numerical simulations were carried out using the one-dimensional Lagrangian finite difference wave code WONDY [Kipp and Lawrence, 1982]. This program solves finite difference approximations to the equations of conservation of mass, momentum, and energy together with an appropriate constitutive law. For simulating plate impact experiments, a rectilinear geometry with free boundary conditions is used. Descriptions of each material layer are entered into the code. These include the thickness, velocity, and the mesh dimensions as well as material parameters such as the density, Hugoniot relations, Grüneisen parameter, Poisson's ratio and yield strength required by elastic-plastic mechanical constitutive law. Discontinuities in pressure, particle velocity, and density associated with shock fronts are treated by the method of artificial viscosity. In general, the stress, σ, consists of a pressure (volumetric) term, P, and a deviatoric term, σ'

$$\sigma=P+\sigma' \tag{1.32}$$

where both stresses and pressures are taken to be positive in compression. The volumetric portion is described by the Grüneisen equation:

$$P=P_h+(\Gamma/V)(E-E_h) \tag{1.33}$$

The reference state is taken to be the Hugoniot:

$$P_h=\rho_o C_o^2\eta/(1-S\eta)^2 \tag{1.34}$$

$$E_h=P_h\eta/(2\rho_o) \tag{1.35}$$

where C_o is initial bulk sound velocity, η is given by:

$$\eta=1-\rho_o/\rho \tag{1.36}$$

The Grüneisen parameter variation with density is modeled as [Rice et al., 1958]:

$$\rho\Gamma=\rho_o\Gamma_o \tag{1.37}$$

The bulk sound speed is given by:

$$V_B^2=(\partial P/\partial\rho)_s \tag{1.38}$$

and the shear modulus is :

$$G=[3(1-2\nu)]/[2(1+\nu)]\rho V_B^2 \tag{1.39}$$

where ν is Poisson's ratio. Detailed description of the code can be found in Kipp and Lawrence [1982].

In our simulation, an elastic-perfect plastic model is used for the flyer plate, driver plate, aluminum buffer and LiF window. The yield strength, Y_o (Table 1.3), is held constant. The von Mises yield condition

$$(\sigma_i')^2\leq(2/3)Y_o^2 \tag{1.40}$$

is used. Since these materials were subject to pressure values far in excess of their yield strengths, the strength effects are very small and this simple model can give a good description of their behaviors. Parameters used for the simulations are given in Table 1.3.

For the anhydrite experiments, the calculated criteria of Table 1.4 is applied during the simulation. Since WONDY does not calculate entropy values for each mesh, equivalent energy criteria (Table 1.4) were applied. This practice may actually lower the criteria values, or overestimate the entropy gain, because part of the energy gain during the complex wave interactions after the sample impacting upon the buffer may come from isentropic compression. To avoid the complication of describing a mixture mesh during the simulation, a mesh is considered solid until its entropy gain is in excess of the complete reaction entropy criterion. Once the complete reaction criterion is reached in a mesh, this mesh is immediately treated as vaporized products and its internal energy is reduced by the amount needed to completely vaporize (or break the chemical bonds of) the materials in this mesh. The vaporized products is then described by a new equation of state. The energy change in this mesh will cause a change in pressure and thus introduce a

disturbance in the flow field on top of the reverberation wave motion between different material layers of the experiments. These two effects are the cause of the complex wavy profile we observed at the Al-LiF interface. Whether these effects are large enough to be observed is determined by material type, thickness, density, impact velocity, vaporization criteria, etc.. The mesh size used is around 0.1 mm. The size is determined by the stability requirement of the simulation [Kipp and Lawrence, 1982].

The approximation that only after mesh meets the complete vaporization criterion it is treated as vapor may underestimate the amount of vaporization of the whole sample. A treatment which can describe the properties of a mixed mesh (mixture of solid $CaSO_4$, CaO, SO_2 and O_2) may be more desirable. Unfortunately, such an equation of state is not available. In the present experiments, the mid-shock pressure shocked sample has ~25% vaporization before it impacts the Al buffer and completely vaporized after it impacts the Al buffer. Therefore, the approximation is less a problem than the case 90% of the sample is vaporized before it impacts the Al buffer. However, it is difficult to quantify the effects.

The equation of state used for the unvaporized anhydrite is the Grüneisen equation (Table 1.3). For the vaporized sample, the equation used is:

$$P=(\gamma-1)\rho E \qquad (1.41)$$

where γ is a constant and was adjusted in the simulation to fit the experimental velocity profiles. Figure 1.10 shows the simulated profiles together with the experimental ones. Reasonably good fits were obtained. For shot 294, the sample was completely vaporized by the first shock wave, and the value of γ used in the simulation is 2.5. For shot 970, the thermodynamic calculation indicates, only 25±2% (Table 1.2) of the sample was vaporized by the first shock wave loading. But after the sample impact onto the buffer, it was completely vaporized upon being subjected to the reflected shock. The value of γ used is 1.73. For shot 971, the entropy gain of the sample from the first shock was less than the incipient reaction value, after the sample impacted the buffer, ~30% of the

sample adjacent to the buffer was vaporized. The γ used is also 1.73. Table 1.5 summaries the results. For shot 975, no vaporization occurred, the simulation initially yields a longer pressure plateau than the experiment. At relatively lower pressure, the experiment profiles suggest, once the shock wave reached the sample's free surface, a layer of sample is ejected from the free-surface as separated solid particles. These particles impact the buffer incoherently. As a result, the buffer-LiF window, that is monitored with the VISAR, does not respond to these particles as it does to the impact of a layer of material. The slow ramp increase of the velocity at the beginning of the experimental profile (Figure 1.10) may be the indication of this kind of bombardment. This effect will reduce the effective thickness of the sample. Upon reducing the sample thickness by 10% in the simulation, an improved fit is obtained and which is shown in Figure 1.10.

All the simulations shown in Figure 1.10 used the criterion calculated using the break-down method. The break-down method appears to provide a good description of shock devolatilization. In order to further test the model's validity and its sensitivity to input parameters, a series of simulations has been conducted. Shot 970 was used as a base-line case, parameters were perturbed in the test simulations to study sensitivity of the fits to variation in material properties. Only one parameter is changed for one simulation.

Figure 1.11 shows the experimental profile with simulation results for break-down and no-break-down criteria. The break-down criterion yields a better agreement with the experimental profile.

Figure 1.12 shows the experimental profile with simulation results for different incipient reaction criteria. The incipient reaction threshold is perturbed by ±50% relative to the break down threshold S_{IR}=2.12 KJ/Kg/K. It is clear that increase or decrease of the incipient reaction criterion gives no better fits to the experiment. This shows that the thermodynamically calculated incipient reaction value represents the data fairly well.

Table 1.5 Values of γ Used in Simulations of Vapor Equation of State

Shot No.	Ph (GPa)	γ
971	25.2±1.1	1.73
970	37.5±1.6	1.73
294	75.9±3.2	2.5

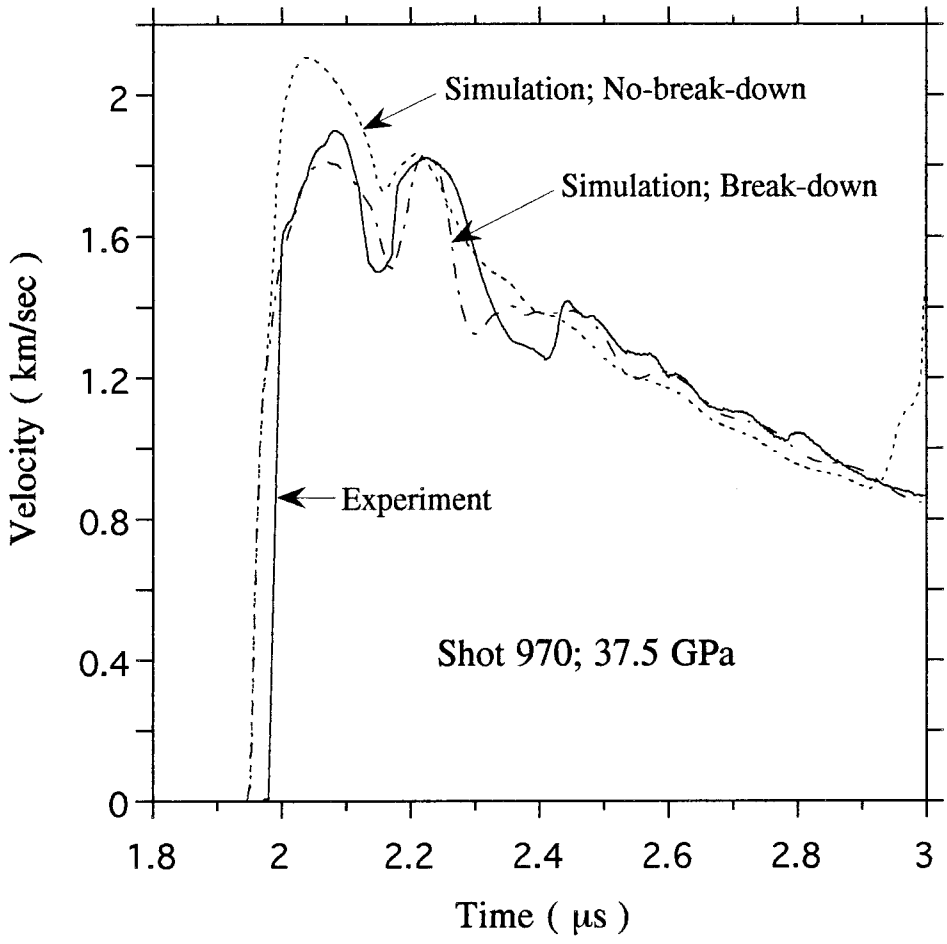

Figure 1.11 Experimental result and numerical simulations for anhydrite, shot 970. Break-down and no-break-down cases are showed.

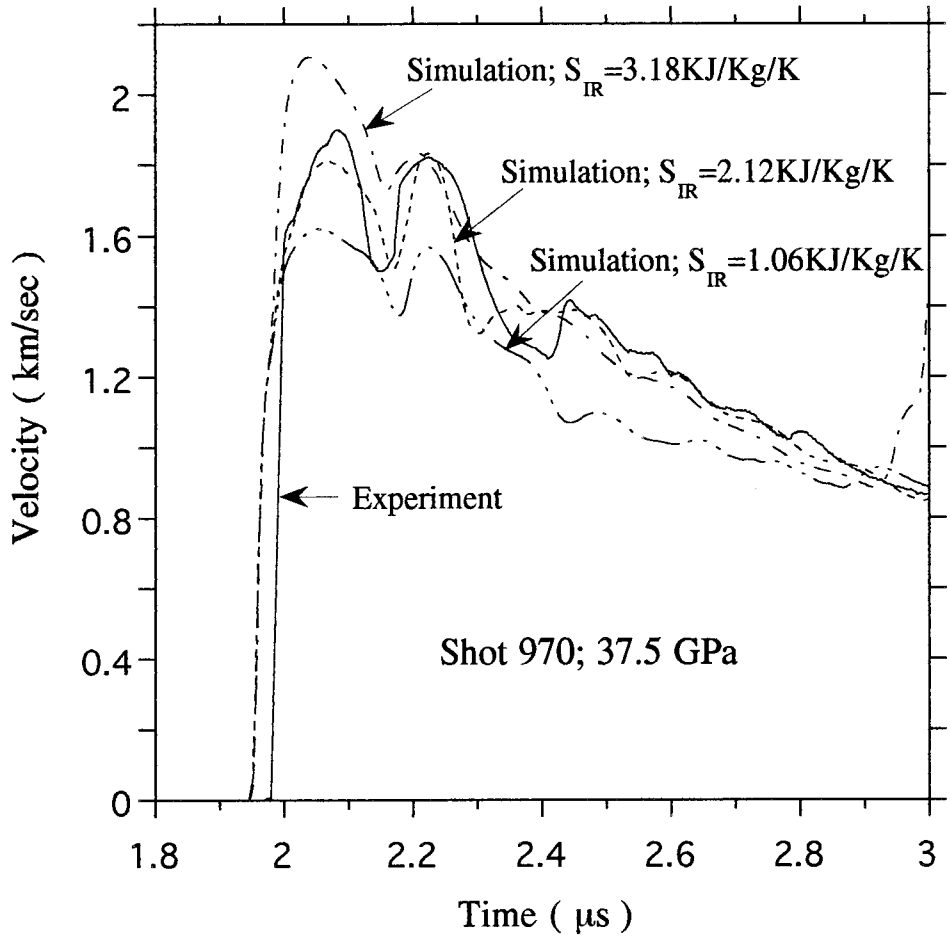

Figure 1.12 Experimental result and numerical simulations for anhydrite, shot 970. The incipient reaction criterion, S_{IR} (Table 1.4), was purposely perturbed by 50% in numerical simulations.

In Figure 1.13, the entropy difference of products and reactant, ΔS, or S_{CR}-S_{IR} is perturbed by ±50%. It also shows that the break-down criterion fits better. Since increase ΔS is equivalent to the no-break-down case, we thus conclude that the break-down criterion is a better approach than the no-break-down approach.

The fact that in the laser vaporization experiments of Gerasimov et al. [1994] much more SO_3 is produced than SO_2 may be explained by that the laser pulse induced a high pressure and temperature condition so that it favors the formation of SO_3 rather than SO_2 which is favored at ambient pressure and temperature. This may also explain why different γ values are needed to best fit the experimental results at different shock pressures.

It is understandable that different γ values are needed for different shots (or pressure), since the gas from $CaSO_4$ and CaO dust behave differently at different pressure ranges and deviate greatly from ideal gases' behavior. In addition, the composition of vaporized products is a mixture of solid and gas and their proportion may change as pressure changes. Studies of detonation products, that also are a mixture of gas and solid particles (CO_2, CO, C, H_2O, N_2 etc.), produced from high explosives at high pressures can be described well by relation of the form of Equation 1.38 with γ changing as release pressure changes. For example, upon detonation of RDX ($C_3H_6N_6O_6$), γ equals 2.48 and 2.98 at 11 GPa and 35 GPa, respectively [Zhang et al., 1979]. Figure 1.14 shows some simulation results of shot 970 with different γ to demonstrate its effects.

The sample density, thickness, impact velocity, and the LiF window density were each altered by ±5%, no dramatic change of the simulation profiles has been found. Since the uncertainties of these parameters are less than 5%, we conclude that the simulation is stable. These results are illustrated in Figure 1.15-1.18.

The incipient reaction pressure we predict for crystal density anhydrite is 81±6.5 GPa (Table 1.4). This is consistant with the shock recovery experiments of Chen et al. [1994]. They found no signs of dissociation up to peak shock pressure of 42 GPa. A

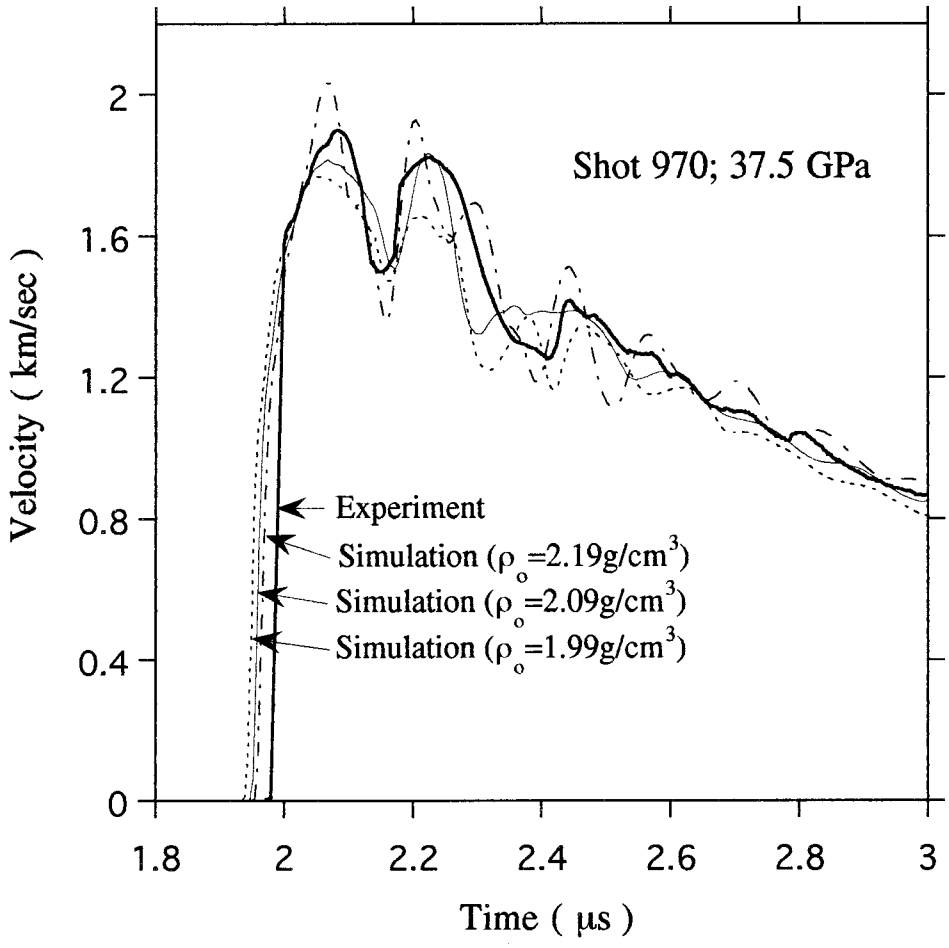

Figure 1.13 Experimental result and numerical simulations for anhydrite, shot 970. The difference of complete reaction criterion , S_{CR}, and incipient reaction criterion, S_{IR} (Table 1.4), was purposely perturbed by 50% in numerical simulations.

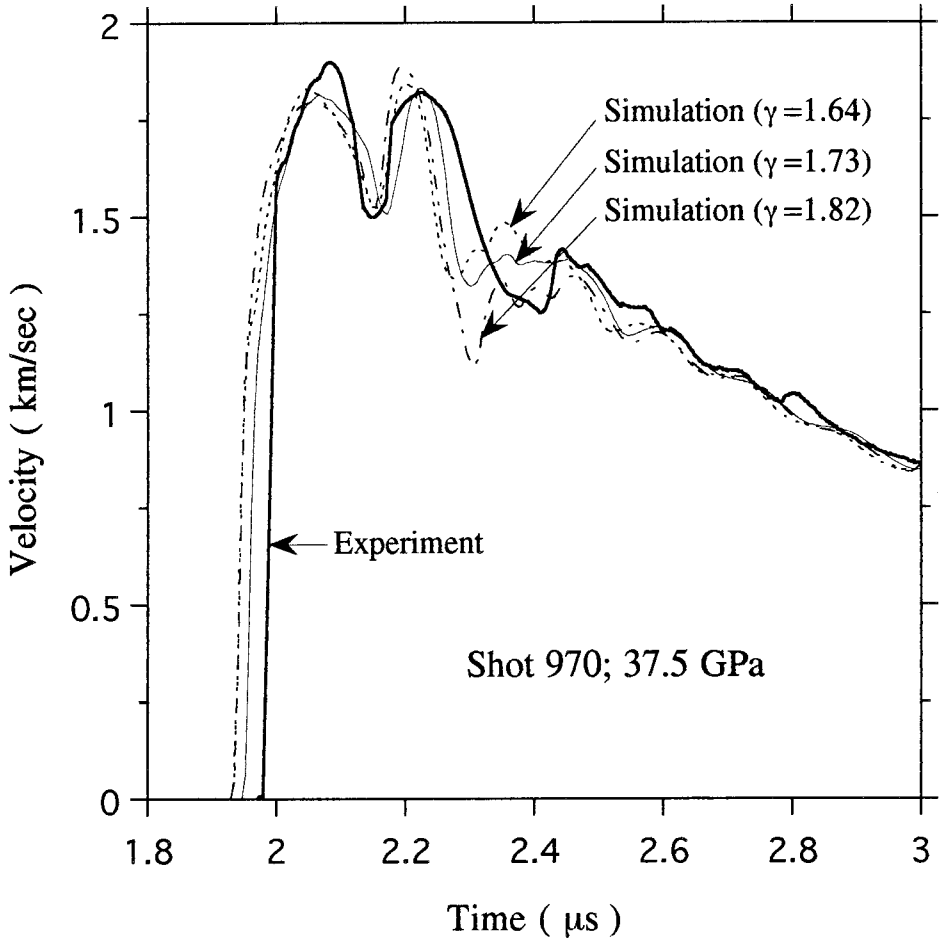

Figure 1.14 Experimental result and numerical simulations for anhydrite, shot 970. Value of γ was perturbed by 5% to demonstrate its effect in numerical simulations.

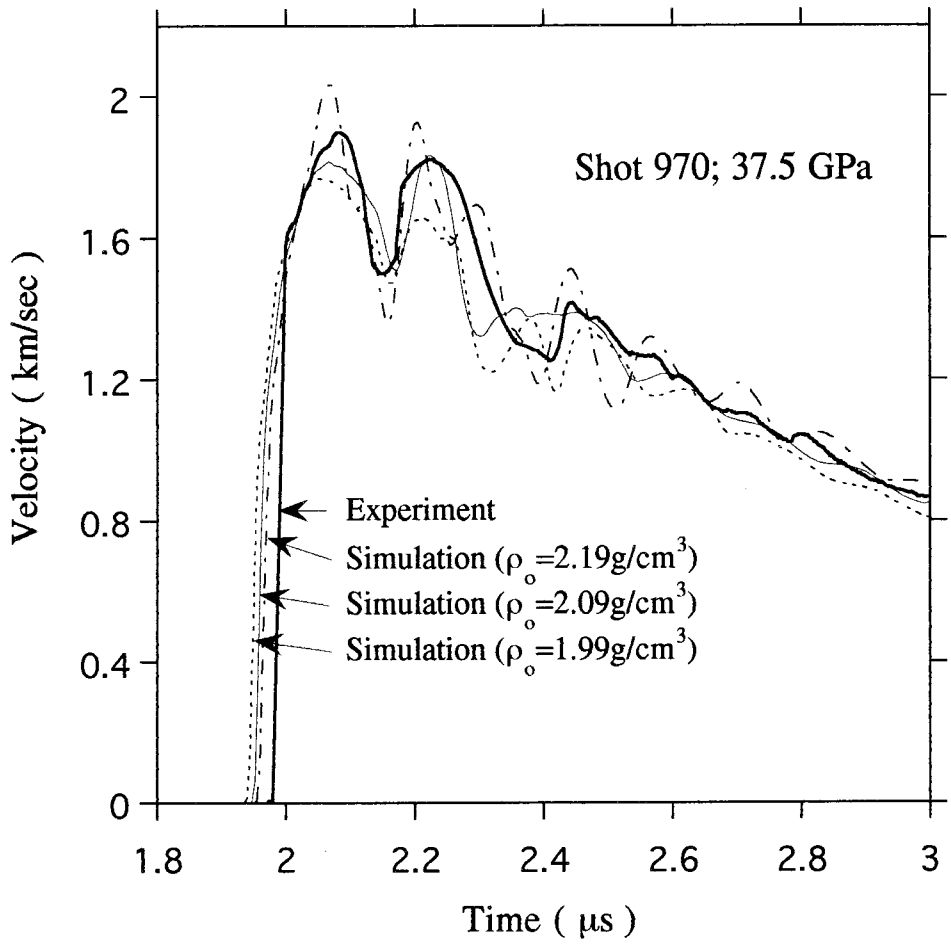

Figure 1.15 Experimental result and numerical simulations for anhydrite, shot 970. Anhydrite sample density is perturbed by 5% in numerical simulations.

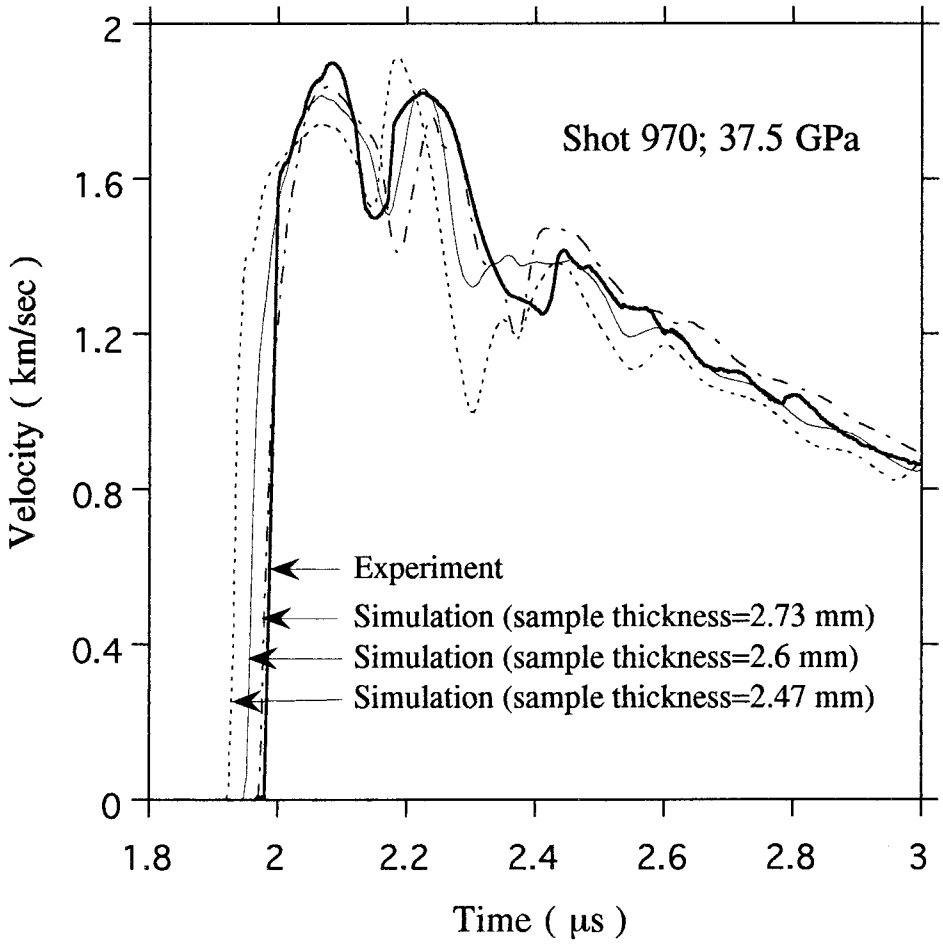

Figure 1.16 Experimental result and numerical simulations for anhydrite, shot 970. Anhydrite sample thickness is perturbed by 5% in numerical simulations.

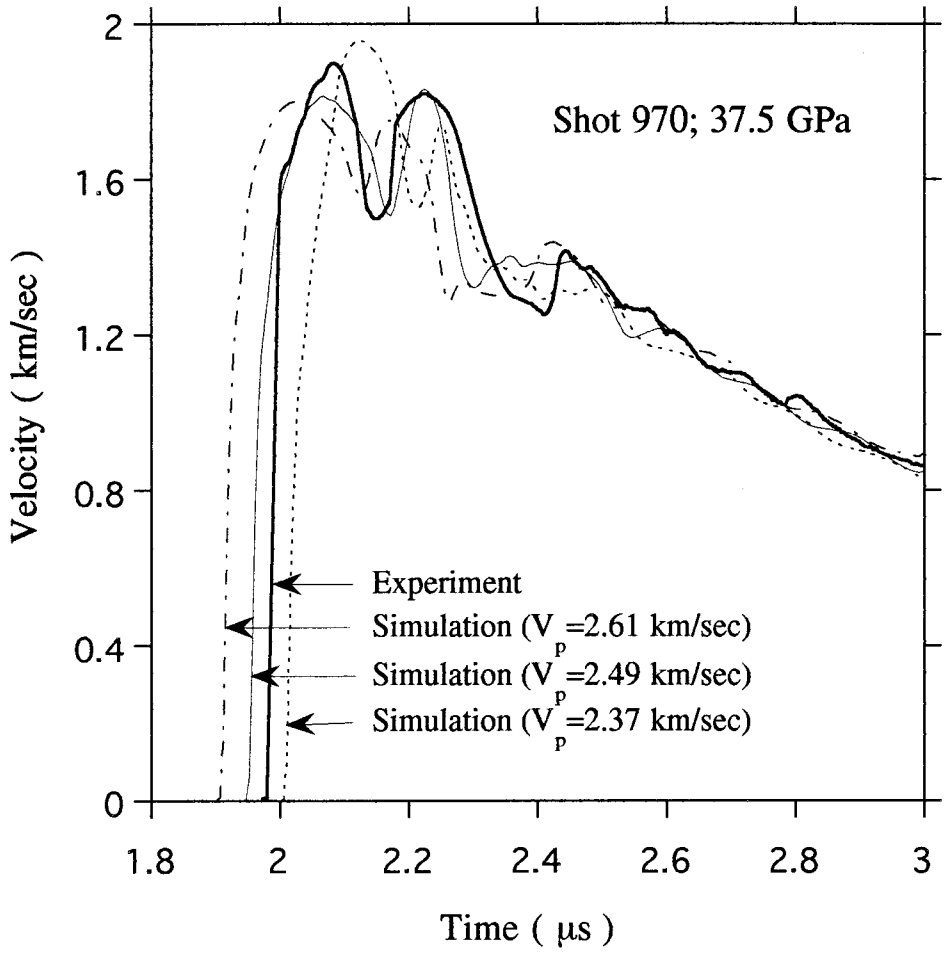

Figure 1.17 Experimental result and numerical simulations for anhydrite, shot 970. Flyer plate velocity is perturbed by 5% in numerical simulations.

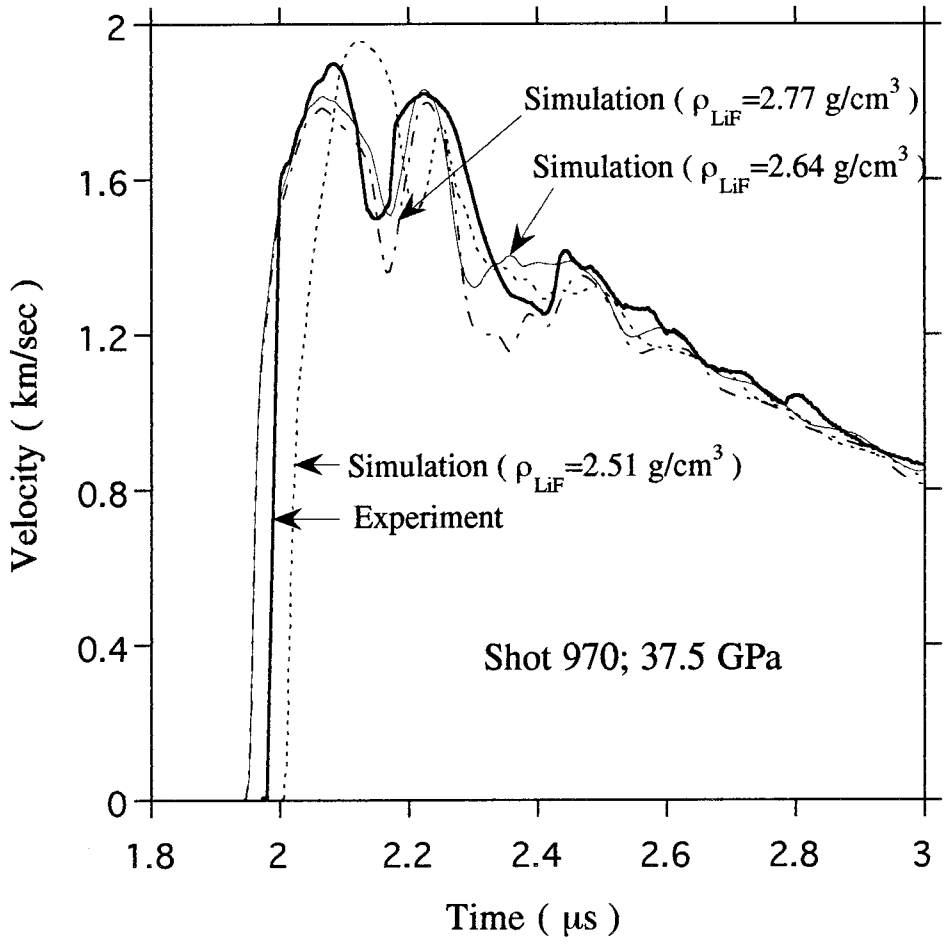

Figure 1.18 Experimental result and numerical simulations for anhydrite, shot 970. LiF window density is perturbed by 5% in numerical simulations.

direct measurement of the shock temperature of anhydrite crystal versus shock pressure may provide more insights of its vaporization mechanism. Figure 1.6 shows the calculated shock temperature versus shock pressure of porous and crystal density anhydrite for both break-down and no-break-down cases. A solid-liquid phase boundary is also suggested based on our experiments and the simple estimation of entropy of melting at high pressure [Stishov, 1974, 1988]. This may be useful in planning future shock temperature experiments.

To show that the complex velocity profile is due to the geometry and chemical dissociation, the sample thickness in a numerical simulation of shot 970 (Figure 1.19) is increased 77% while other parameters remain unchanged. The complex features are still displaced but the position and amplitude have changed. Figure 1.20 shows a simulation of shot 970 in which the sample is crystal density anhydrite with the same mass per unit area as the sample in the experiment while all other parameters are the same. It shows clearly that the wave reverberations caused the major oscillation features of the particle velocity profile since the crystal density anhydrite does not vaporize in this simulation. Thus we conclude that the complex profile comes from the wave reverberations plus the effect of chemical dissociation.

Since equation (1.41) is in the form of an ideal gas equation of state and appears simple to describe the vaporized mixture, the Tillotson equation of state [Melosh, 1989] is used to determine whether it can give a better fit of the experimental profile. In the compressed region ($\rho/\rho_O \geq 1$) and for the cold expanded states where the energy density is less than the incipient vaporization, $E<E_{iv}$, the Tillotson EOS takes the form as

$$p = \left[a + \frac{b}{(E/(E_o\eta^2)+1)}\right]\rho E + A\mu + B\mu^2 \qquad (1.42)$$

where $\eta=\rho/\rho_O$, $\mu=\eta-1$, and a, b, A, B, and E_O are the Tillotson parameters. It is easy to see that (a+b) is the Grüneisen parameter at zero pressure,

$$(a+b) = \Gamma_o \qquad (1.43)$$

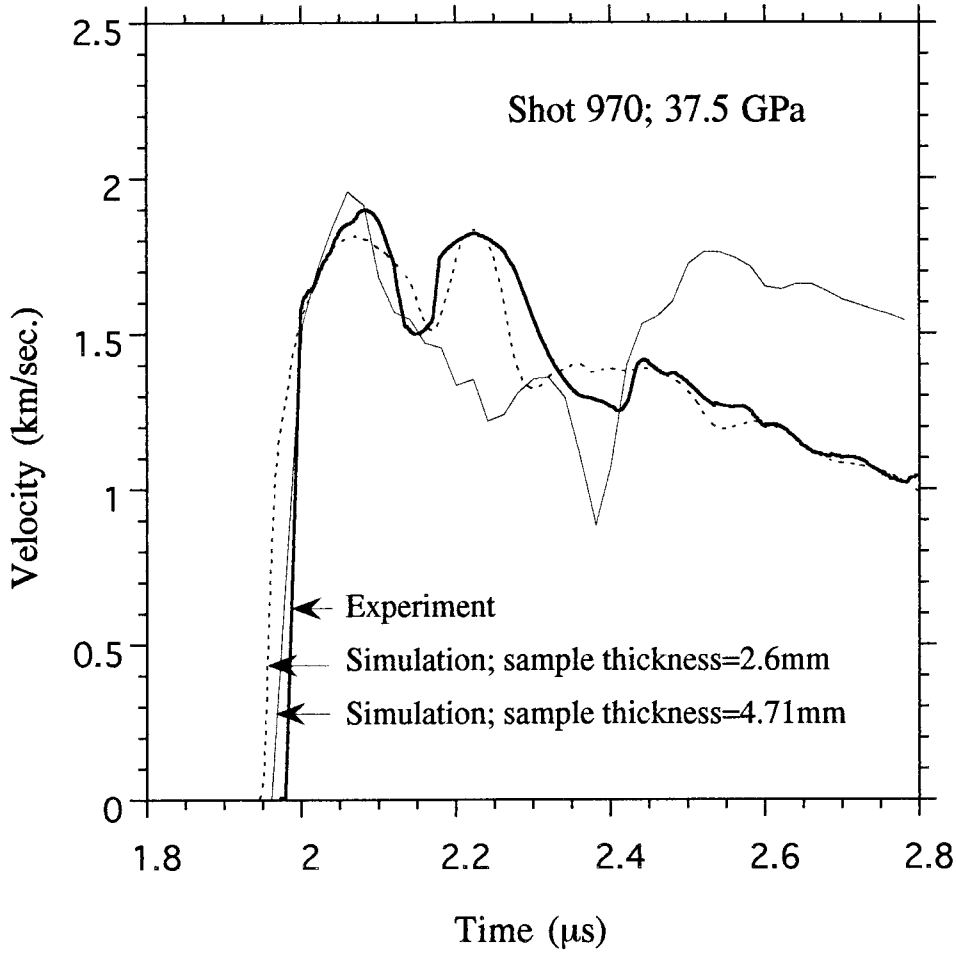

Figure 1.19 Experimental result and numerical simulations for anhydrite, shot 970. Anhydrite sample thickness is increased by 77% in one numerical simulation. The time of this simulation is shifted to compare with each other.

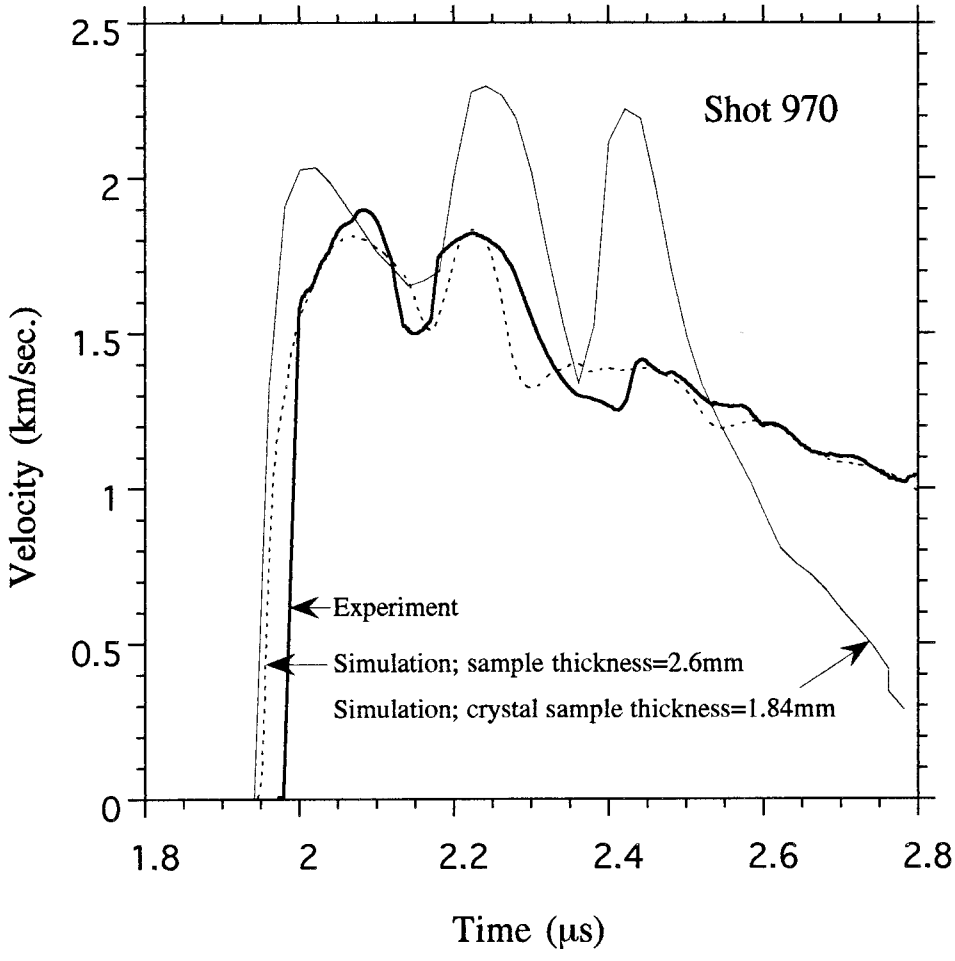

Figure 1.20 Experimental result and numerical simulations for anhydrite, shot 970. Crystal density anhydrite sample is used in one numerical simulation. The time of this simulation is shifted to compare with each other.

a is usually chosen to equal 0.5 to give a better simulation result instead of the high-pressure limit value 0.6 [Zeldovich and Raizer, 1966]. The C_O and S parameters of the linear shock-particle velocity model can be expressed in terms of the Tillotson parameters by

$$C_o = (A/\rho_o)^{1/2} \tag{1.44}$$

$$S = 1/2[1 + B/A + (a+b)/2] \tag{1.45}$$

In the expanded state, $\rho/\rho_O \leq 1$, when the internal energy exceeds the energy of complete vaporization $E > E_{CV}$, the pressure is given by

$$p = a\rho E + \left\{ \frac{b\rho E}{(E/(E_o\eta^2)+1)} + A\mu e^{-\beta(\rho_o/\rho - 1)} \right\} e^{-\alpha(\rho_o/\rho - 1)^2} \tag{1.46}$$

where α and β are constants that control the rate of convergence of this equation to the perfect gas law. In the partial vaporization regime when $\rho/\rho_O < 1$ and $E_{iV} < E < E_{CV}$, the pressure is computed from a hybrid formula to make a smooth transition from equation (1.42) to (1.46). The hybrid formula is

$$p = [(E - E_{iv})p_E + (E_{cv} - E)p_C]/(E_{cv} - E_{iv}) \tag{1.47}$$

where p_E is computed from equation (1.46) and p_C is computed from equation (1.42).

The parameters a, b, A, B are determined from equations (1.43) to (1.45). E_O is determined by fitting equation (1.42) to experimental Hugoniot data. α and β are chosen as 5. Parameters used for shot 970 simulation are listed in Table 1.6. The simulated velocity profile is shown in Figure 1.21 and compared with the experimental profile and the simulation result using equation (1.41). The Tillotson equation gives a more oscillatory profile and does not match the experimental profile as well as equation (1.41) did. Other values of α and β (e.g., $\alpha=\beta=1.0$) were also tested, but the result changed little. The oscillatory profile is in part induced by using different expressions of the Tillotson EOS in varying energy and density ranges.

To gain more insight of the vaporization process and how the different equation of states describe the materials behaviors, isentropic curves in the P-V plane are calculated

Table 1.6 Parameters of Tillotson Equation of States of Anhydrite

Material	ρ_o (Kg/m^3)	a	b	A (GPa)	B (GPa)	E_o (MJ/Kg)	E_{iv} (MJ/Kg)	E_{cv} (MJ/Kg)	α	β
Anhydrite (Porous)	2090±40	0.5	2.0	12.1	25.0	3.21	2.12	13.7	5.0	5.0

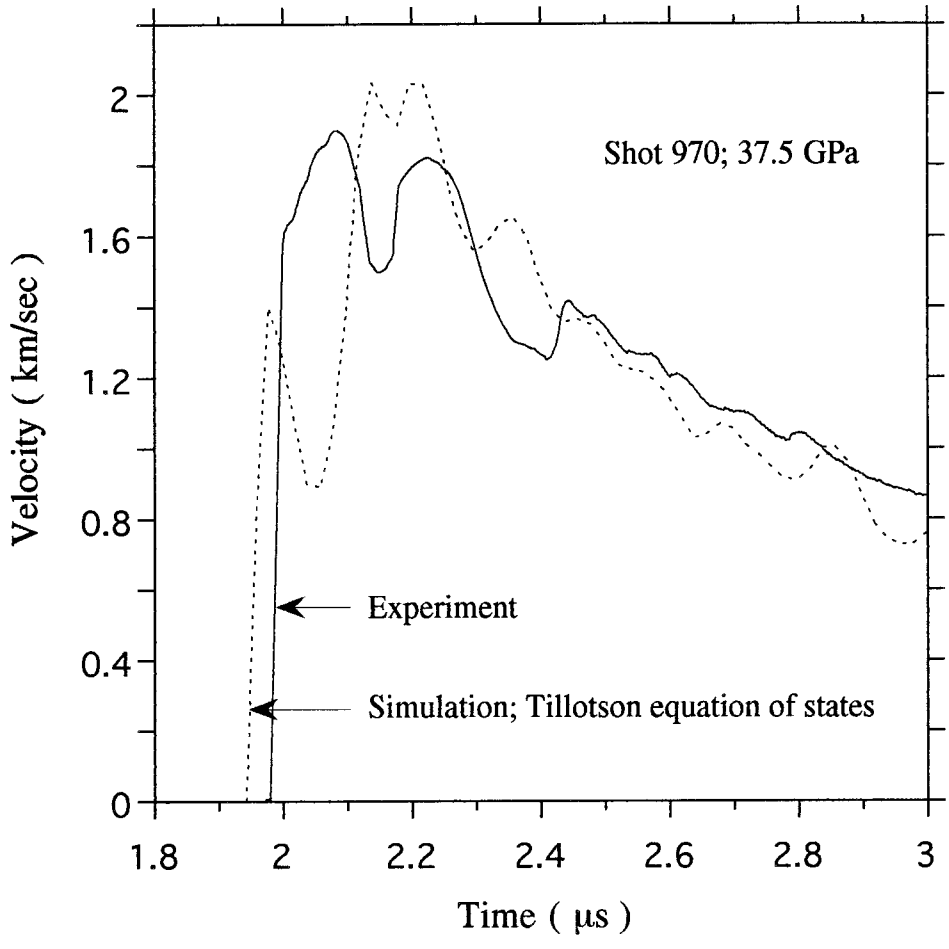

Figure 1.21 Experimental result and numerical simulation with Tillotson equation of states for anhydrite, shot 970.

for anhydrite experiment shot 294 (Figure 1.22) using equation (1.41) and Tillotson EOS. The data used are obtained from a mesh in the middle of the sample. To clearly see the characteristics of the release curves, the witness plate and LiF window are removed in these simulations to avoid the compression wave reflecting back into the sample after the vaporized products impact the witness plate. The Tillotson EOS gives a adiabatic curve similar to an isentropic release curve using Grüneisen EOS. Equation (1.41), however, gives a quite different behavior. Due to the large decrease of internal energy caused by the chemical dissociation, the pressure of the mesh immediately drops down from A to B. Then the mesh is compressed from B to C. From state C the pressure is released gradually down to state D. This demonstrates that the vaporization products are much more compressible than the initial reactant (porous anhydrite). The energy required to compress the material within the mesh from state B to state C upon reflection of the stress wave from the driver plate gives rise to the strong compression of the vaporized sample. It is this behavior that give rise, in part, to the oscillatory structure of the observed velocity profile.

1.5 Summary

Thermodynamic calculations of incipient and complete vaporization of $CaSO_4$ to CaO, SO_2 and O_2 criteria have been obtained using two methods. The first method is the one in which no shock-induced chemical bond break-down by the shock wave along the Hugoniot is taken into account, i.e., the no-break-down method. The second method assumes that the shock induces chemical bond break down of $CaSO_4$ to $CaO+SO_2+\frac{1}{2}O_2$ along the Hugoniot, the break-down method. Shock-induced melting is not likely to be an equivalent assumption to the break-down method. However, melting could also be occurring in the experiments. The no-beak-down method predicts a higher shock pressure value for complete reaction of crystal anhydrite of 280±23 GPa, whereas the break-down

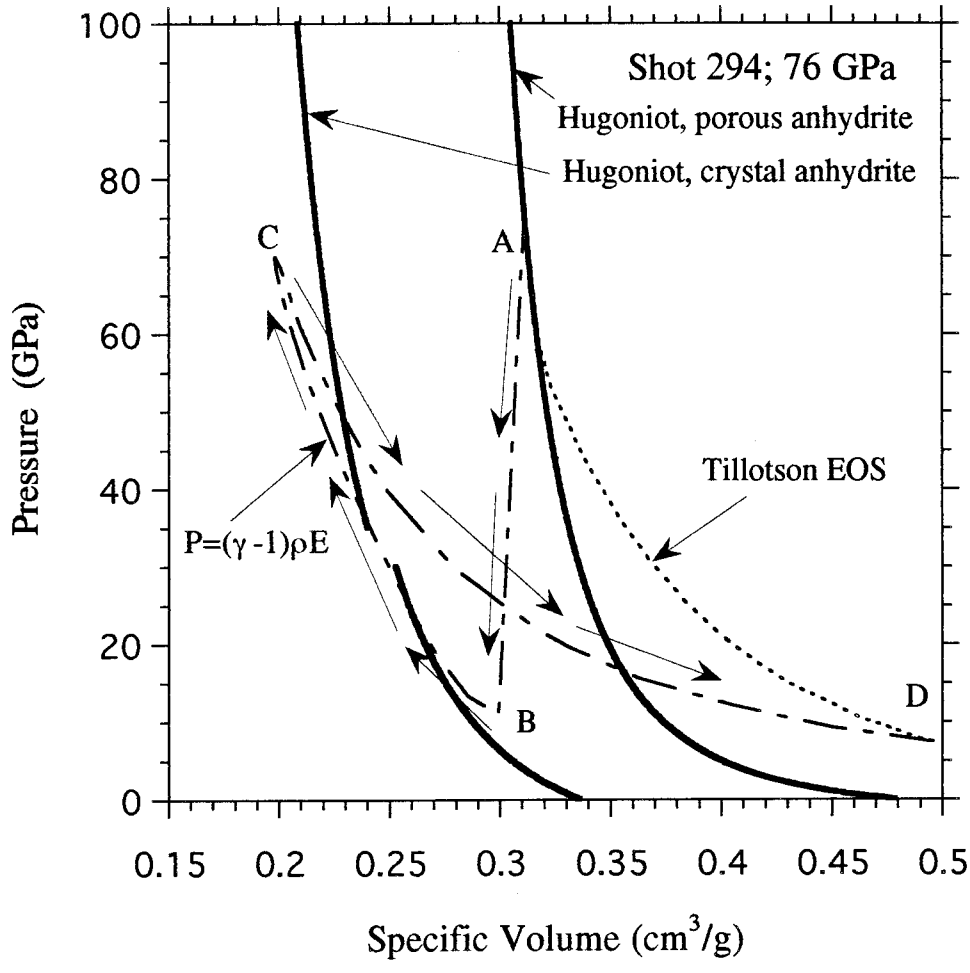

Figure 1.22 Adiabatic curves in P-V plane using Tillotson EOS and $p=(\gamma-1)\rho E$ for anhydrite, shot 294. The Tillotson parameters used are given in Table 1.6.

method predicts 155±13 GPa. The energy required for complete vaporization is 13.2±0.85 MJ/Kg for the break-down and 20.5±1.3 MJ/Kg for the no-break-down cases, respectively. Thus the no-break-down method induces less vaporization for a given impact velocity. This conclusion is not affected by the phase change at pressure 30-35 GPa as the estimated transition energy (0.09 MJ/Kg) is much less than the energy required to shock vaporize anhydrite at high pressure.

Shock vaporization experiments were carried out for porous anhydrite up to 76 GPa. Velocity histories of aluminum-LiF window interface were measured using velocity interferometer system for any reflector (VISAR) [Barker and Hollenbach, 1972].

A Lagrangian one-dimensional wave propagation code (WONDY) was used to simulate the measured velocity profiles. We found that the vaporization criteria calculated using the break-down method provides better agreement with the experimental profiles than could be obtained using the no-break-down method. The vaporized products can best be described by equation in the form $P=(\gamma-1)\rho E$, where γ varied from 1.73 to 2.5 for pressures of 25 to 76 GPa. Tillotson EOS has also been used to fit the experiemntal profile. It fits the experimental profile better than the no-break-down method but not as well as the break-down method. Since the Tillotson EOS simulates the transition from a solid to a gas gradually, it also demonstrates that the break-down method is a better approach to the description of the volatilization process.

Since the vaporization along the Hugoniot assumption yields numerical profiles in good agreement with observed profiles, we infer that the decomposition rate of the anhydrite is very fast, possibly occurring within a few nanoseconds after the complete reaction entropy criterion is reached.

The thermodynamics of the reaction $2CaSO_4=2CaO+2SO_2+O_2$ appears to closely describe the observed particle velocity profile and provide a reasonable decomposition mechanism at relatively low energy level (<6.43 MJ/Kg, Table 1.2) where the dominant

gas is SO_2, but the reaction $CaSO_4=CaO+SO_3$ may be dominant at high pressure, high energy level (>6.43 MJ/Kg, >76 GPa, Table 1.2) where the dominant gas is SO_3.

Chapter 2

Shock Vaporization of Porous Calcite

2.1 Introduction

Carbonate rocks are present in nearly all shallow marine sedimentary basins, or, their metamorphosed equivalents on the Earth. Thus it is not surprising that about 30% of all terrestrial impact structures have been formed in carbonate rocks [Grieve and Robertson, 1979]. Kieffer and Simonds [1980] postulate that the effect of the rapidly expanding CO_2, shock-induced from the carbonate during impact, leads to the dispersion and subsequent erosion of impact melt, resulting in the observed deficiency of impact melt layers in impact structures formed in carbonate rocks. Lange and Ahrens [1986] studied shock-induced CO_2 loss from single crystal calcite using solid recovery method up to peak pressure of 42 GPa, and found that incipient CO_2 loss started at as low as ~10 GPa due to shear band heating [Grady, 1977]. Extrapolating their data, they predict that the complete loss of CO_2 in calcite will occur at ~70 GPa. Using these experimental data and the results of numerical impact cratering simulations, O'Keefe and Ahrens [1989] proposed that the Cretaceous/Tertiary extinction bolide [Alvarez et al., 1980] would release a large amount of CO_2 which would cause a 2-10°C global greenhouse warming for a period of 10^4-10^5 years. The recent discovery of the Chicxulub impact structure and the dominance of calcium carbonate (calcite) and calcium sulfate minerals (anhydrite and gypsum) in the upper 3 km of the structure [Koeberl, 1993] has led to active research into

their devolatilization effect upon impact [Brett, 1992; Sigurdsson et al., 1992; Chen et al., 1994].

Previously, two low-pressure phase transitions in calcite, calcite II and III, were discovered by Bridgman [1939]. Later, compressive behavior of $CaCO_3$ under static and dynamic loading have been the subject of many studies [Jamieson, 1957; Adadurov et al., 1961; Ahrens and Gregson, 1964; Ahrens et al., 1966; Singh and Kennedy, 1974; Huang and Wyllie, 1976; Fiquet et al., 1994]. Above about 10 GPa, the single-crystal calcite [Ahrens and Gregson, 1964], polycrystalline calcite [Adadurov et al., 1961; Kalashnikov et al., 1973] and crystal aragonite [Vizgirda and Ahrens, 1982] Hugoniots are very similar, suggesting transformation to a similar high-pressure polymorph of $CaCO_3$. We designate this phase as $CaCO_3$ IV [see also Vizgirda and Ahrens, 1982]. Release isentropes for polycrystalline calcite rocks shocked to pressures up to about 40 GPa have been determined using laser interferometry [Schuler and Grady, 1977; Grady et al., 1978; Grady, 1983] and electromagnetic particle velocity gauges [Murri et al., 1975; Larson and Anderson, 1979]. Murri et al. [1975] employed electromagnetic particle gauges to determine release paths for selected carbonate rocks (porosity 0 and 15%) shocked to between 10 and 30 GPa. In this pressure range, the initial release paths lie at greater densities than the Hugoniot. Release paths for single-crystal aragonite shocked to pressures up to 40 GPa have been determined using buffer and inclined mirror techniques [Vizgirda and Ahrens, 1982]. For shock pressures up to about 13 GPa, the release paths are steep, and maximum post-shock densities are greater than the initial densities. For shock pressures between about 13 and 40 GPa, the release paths generally lie close to the Hugoniot, and maximum post-shock densities are less than or equal to the initial density. The steep release adiabats indicate reversal, upon unloading, of a phase transformation. This phenomenon has been observed for a number of silicates, including quartz [Grady et al., 1974], plagioclase feldspar [Ahrens et al., 1969a, b], and olivine [Jackson and Ahrens,

1979] and has been interpreted to indicate retention of the denser high pressure phase during the initial stages of unloading.

In this study, the results of vaporization experiments on porous calcite (Dover chalk, 54% crystal density) up to 19 GPa are reported. Porous calcite samples were shock loaded. An aluminum witness plate was placed at a distance behind the free-surface of the sample in vacuum. The velocity history of the aluminum witness plate accelerated by the shocked sample products was monitored by using a lithium fluoride (LiF) window using a velocity interferometer in an arrangement first described by Trucano and Asay [1987]. A one-dimensional Lagrangian finite difference wavecode, WONDY [Kipp and Lawrence, 1982], was used to fit the experimental results. Combined with thermodynamic calculational results, constraints on the shock-induced pressure and entropy required to induce incipient and complete vaporization, the vapor equation of state and the chemical decomposition rate are obtained.

2.2 Experiments

As illustrated in Figure 2.1, the target assembly is the same as in Chapter 1. The Dover chalk samples were cylindrical disks with a diameter of 25 mm and a thickness of 2-2.6 mm. The loading system and diagnostic system are also the same as described in detail in Chapter 1. Experimental parameters are listed in Table 2.1.

2.3 Thermodynamic Calculations

Shock States, Incipient and Complete Reaction Criteria Calculations

The same methods and formulations as used in Chapter 1 have been employed again in the calculations of this chapter.

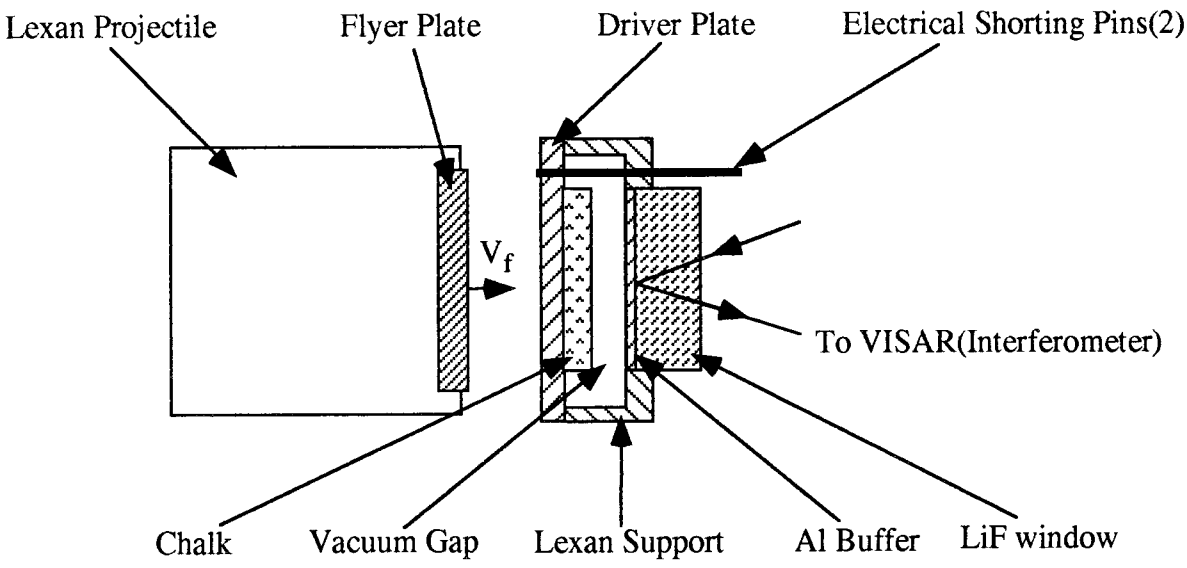

Figure 2.1 Experimental configuration, shock vaporization, chalk.

Table 2.1 Experimental Parameters of Chalk Experiments

Shot No.	Flyer Plate Thickness (mm) (Material)	Impact Velocity (km/sec)	Driver Plate Thickness (mm) (Material)	Sample Thickness (mm)	Sample Initial Density (g/cm^3)	Gap (mm)	Al6061 Buffer Thickness (mm)	LiF Window Thickness (mm)
976	3.790±0.003 (Al6061)	1.44±0.02	1.077±0.007 (Al6061)	2.619±0.016	1.448±0.004	1.407±0.020	0.8704±0.0012	11.999±0.001
973	3.863±0.003 (304 S. S.)	1.96±0.02	0.777±0.005 (304 S. S.)	1.989±0.007	1.455±0.017	2.037±0.007	0.9830±0.0075	1.989±0.002
972	3.929±0.003 (W)	2.42±0.03	2.037±0.002 (304 S. S.)	1.993±0.009	1.454±0.013	3.01±0.01	0.9703±0.0018	12.001±0.003

Shock states for the present experiments are given in Table 2.2 and the parameters used are listed in Table 2.3. Figure 2.2 shows both Hugoniots of crystal and porous calcite in P-V plane. The circles represent the experiments.

Figure 2.3 shows the phase diagram of $CaCO_3$ with the Hugoniots of crystal and porous calcite. The phase diagram is based on a theoretical model produced by Kerley [1989]. It is designed to agree with all available experimental phase boundaries [Johannes and Puhan, 1971; Irving and Wyllie, 1975] at low pressure range (up to 4 GPa). For break-down case, themodynamic calculations show that calcite breaks down before it melts for the shock states achieved in the present experiments. For no-break-down case, melting ocurrs at 14 and 96 GPa for porous and crystal $CaCO_3$, respectively. Thus, in present experiments, melting does not occur and cannot be used to explain the experimental profiles.

Vizgirda and Ahrens [1982], using the entropy method [see, e.g., Zel'dovich and Raizer, 1967; Ahrens and O'Keefe, 1972], calculated the incipient and complete vaporization criteria for calcite and aragonite. They found that the incipient vaporization shock pressures for calcite and aragonite are 40±5 and 66±7 GPa, respectively. The complete vaporization pressures for both calcite and aragonite are above 100 GPa. The previous calculations of the shock pressure required to achieve complete vaporization, however, did not taken into account the latent heat of vaporization. Using the entropy method, Tyburczy and Ahrens [1986] estimated the shock vaporization pressure requirements for Dover chalk and found that at ~10 GPa, about 90% chalk vaporized. In this section, the entropy method is again employed in a similar thermodynamic calculation. The possible chemical dissociation energy and entropy of calcite is also taken into account for the reaction:

$$CaCO_3 \rightarrow CaO + CO_2 \uparrow \qquad (2.1)$$

The incipient and complete reaction criteria for both crystal and porous calcite were calculated using both the break-down and no-break-down method (see Chapter 1).

Table 2.2 Shock States of Chalk Samples

Shot No.	P_h (GPa)	E_h (KJ/Kg)	ΔS_h (KJ/Kg/K)	R_f (%)
976	4.3±1.5	$(6.8\pm2.4)\times10^2$	1.3±0.4	0.0
973	8.7±3	$(1.5\pm0.5)\times10^3$	2.0±0.6	40±12
972	19±5	$(3.5\pm0.9)\times10^3$	3.6±0.9	100

ρ_o is initial density, P_h is Hugoniot pressure, E_h is Hugoniot energy, ΔS_h is entropy increase, R_f is percent reacted.

Table 2.3 Shock Equation of State Parameters

Material	ρ_0 (g/cm^3)	C_0 (km/sec)	S	Γ_0	ν_0	Y_0 (GPa)	Refs.
W	19.2	4.04±0.01	1.230±0.004	1.54	0.28	2.4	a
304 S. S.	7.87±0.02	4.58±0.01	1.49±0.01	2.2	0.29	0.2	a, b
Al6061	2.683±0.003	5.35±0.06	1.34±0.02	2.1	0.34	0.2	a
LiF	2.64±0.02	5.15±0.03	1.35±0.01	1.6	0.22	0.2	a
Lexan	1.19±0.01	2.42±0.03	1.32±0.11	1.64	-	-	a
Calcite (HPP)	3.10	5.58	1.25	1.183	-	-	c
Chalk	1.40±0.04	0.45±0.11	1.76±0.41	1.50	-	-	d

ρ_0 is density, C_0 and S are shock wave equation of state (EOS) constants, Γ_0 is Grüneisen parameter, ν_0 is Poison's ratio, and Y_0 is yield strength. References: a, Marsh [1980], b, Duffy [1992]; c, Ahrens et al. [1995]; d, Tyburczy and Ahrens [1986]; HPP - high-pressure-phase.

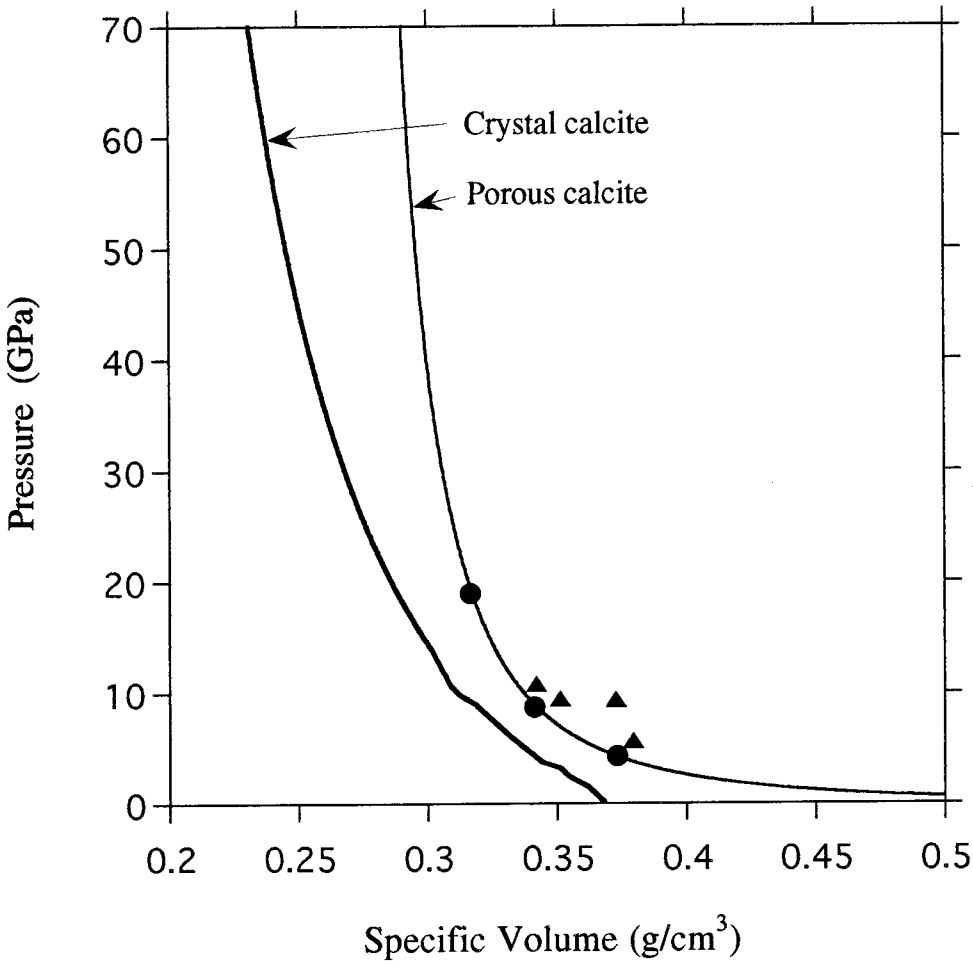

Figure 2.2 Hugoniot relation of porous and crystal density calcite in P-V plane. Parameters used to calculate Hugoniot curves are given in Table 2.1 and 2.3. Circles represent experiments (Table 2.2). Triangles are Dover chalk (initial density 1.40 g/cm^3). Data from Tyburczy and Ahrens [1986].

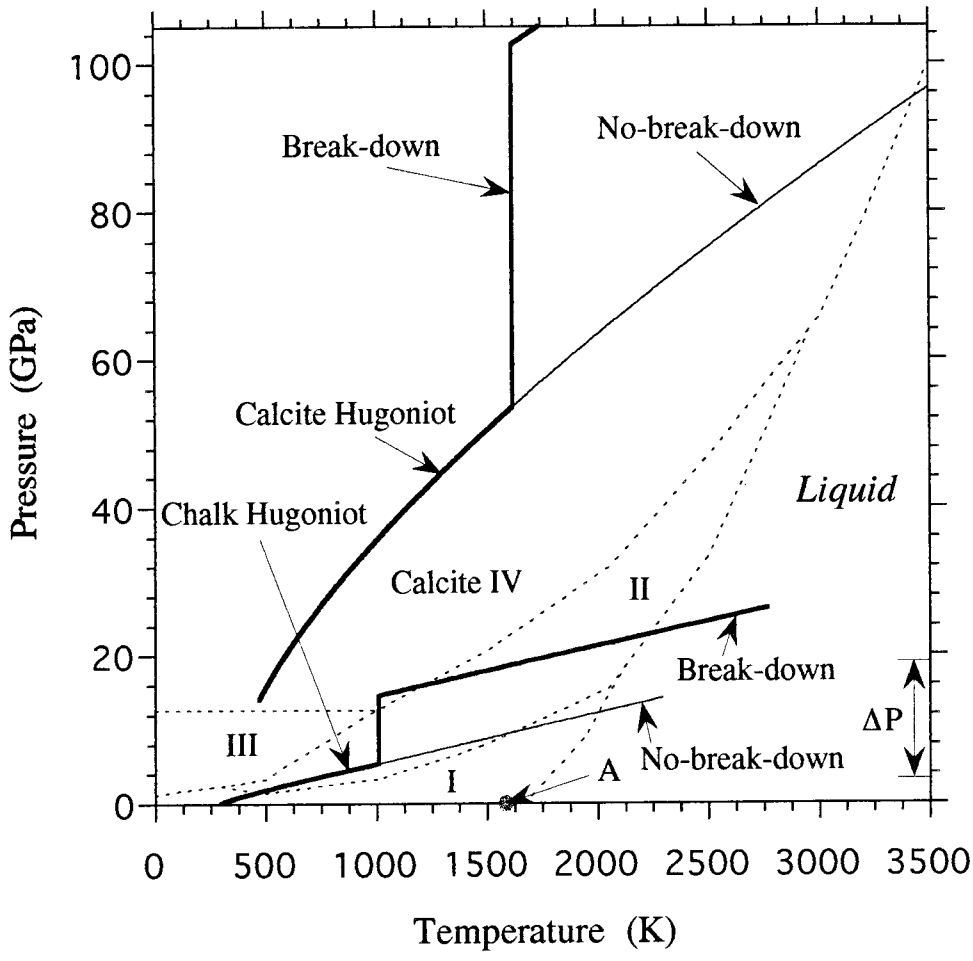

Figure 2.3 Hugoniot temperature of crystal and porous calcite superimposed on theoretical phase diagram by Kerley [1989]. Point A is the triple point of Calcite I, liquid and vapor. It occurs at 40 bars and 1583K [Tyburczy and Ahrens, 1986]. ΔP is the pressure range of present experiments.

For porous calcite, the shock wave data shows no evidence of the phase changes observed in non-porous samples [Tyburczy and Ahrens, 1986], hence we assume $\Delta S_{tr}=0$. For crystal density calcite, the equation of state (EOS) parameters, $\rho_{oc}=2701$ Kg/m^3, $K_{os}=71.7\pm1.8$ GPa and $K'=4.42\pm0.6$, for low pressure phase (LPP, calcite I) are employed. These values were chosen from averaging the highly consistent results by many authors [Bridgman, 1925; Dandekar, 1968; Singh and Kennedy, 1974; Fiquet et al., 1994]. For pressures above 14 GPa (high pressure phase, calcite IV), EOS parameters were chosen from available data by Fiquet et al. [1994], Vizgirda and Ahrens [1982], and Ahrens et al. [1995]. We used, $\rho_{oc}=3100$ Kg/m^3, $K_{os}=96.5$ GPa, $K'=4.0$, $\Gamma_o=1.183$, $\Delta E_{tr}=0.02$ MJ/Kg. We thus calculated that $\Delta S_{tr}=0.067$ KJ/Kg/K.

Since there are no specific heat, C_v, data available at high pressure, the Dulong-Petit value, 3nR (where n is the number of atoms in one molecule, R is the ideal gas constant and its value is 8.31441 J/mol/K), was used in the calculation. The uncertainties introduced by this treatment were estimated by comparing the Dulong-Petit value with the tabulated values, C_p, at ambient pressure [Robie et al., 1979]. The Dulong-Petit value (1.246 KJ/Kg/K) is larger than experimental value at room temperature (0.834 KJ/Kg/K at 298.15 K) but somewhat less than the high temperature value (1.304 KJ/Kg/K at 1200 K).

The calculated incipient and complete reaction entropies and corresponding Hugoniot pressures are listed in Table 2.4. Figure 2.4 shows the calculated results of entropy gain versus Hugoniot pressure for both porous- and crystal-density calcite. The break-down method gives a steeper increase of entropy gain than the no-break-down method after the entropy gain reaches the incipient reaction value. The circles and crosses represent the experiments. Figure 2.5 gives the reaction percentage versus shock pressure. It is clear that the no-break-down method gives much higher shock pressure to complete reaction for both porous and crystal calcite. Circles and crosses represent the experiments and values obtained using the break-down method are given in Table 2.2.

Table 2.4 Incipient and Complete Reaction Parameters

Material	ρ_o (g/cm^3)	P_{hIR} (GPa)	P_{hCR} (GPa)	$(E_H\text{-}E_S)_{IR}$ (KJ/Kg)	$(E_H\text{-}E_S)_{CR}$ (KJ/Kg)	S_{IR} (KJ/Kg/K)	S_{CR} (KJ/Kg/K)
Calcite	2.701	54±6	103±12	$(1.40\pm0.16)\times10^3$	$(4.01\pm0.43)\times10^3$	1.47±0.07	2.91±0.13
Chalk	1.45±0.02	5.4±1.9	14.6±3.8	$(0.87\pm0.3)\times10^3$	$(2.33\pm0.6)\times10^3$	1.47±0.07	2.91±0.13

ρ_o is initial density, P_{hIR} is incipient reaction Hugoniot pressure, P_{hCR} is complete reaction Hugoniot pressure, E_H is Hugoniot energy, E_S is isentropic energy, S_{IR} is incipient reaction entropy, S_{CR} is complete reaction entropy.

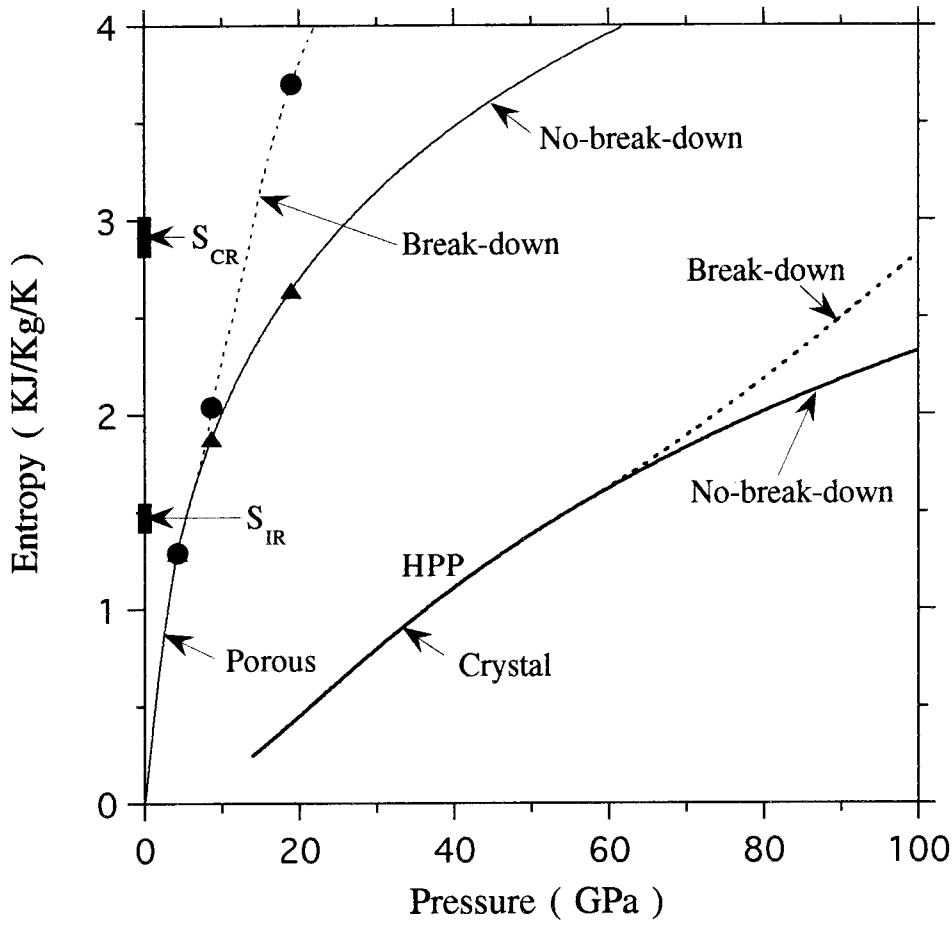

Figure 2.4 Entropy gain versus shock pressure for porous and crystal density calcite. Break-down refers to calculation method where after entropy reaches incipient reaction entropy (Table 2.4), shock temperatures do not increase until the complete reaction entropy criteron is reached. No-break-down refers to calculational method where shock temperature will continue to increase after entropy reaches incipient reaction value. Circles used break-down method, triangles used no-break-down method. HPP refers to high-pressure phase (Calcite IV).

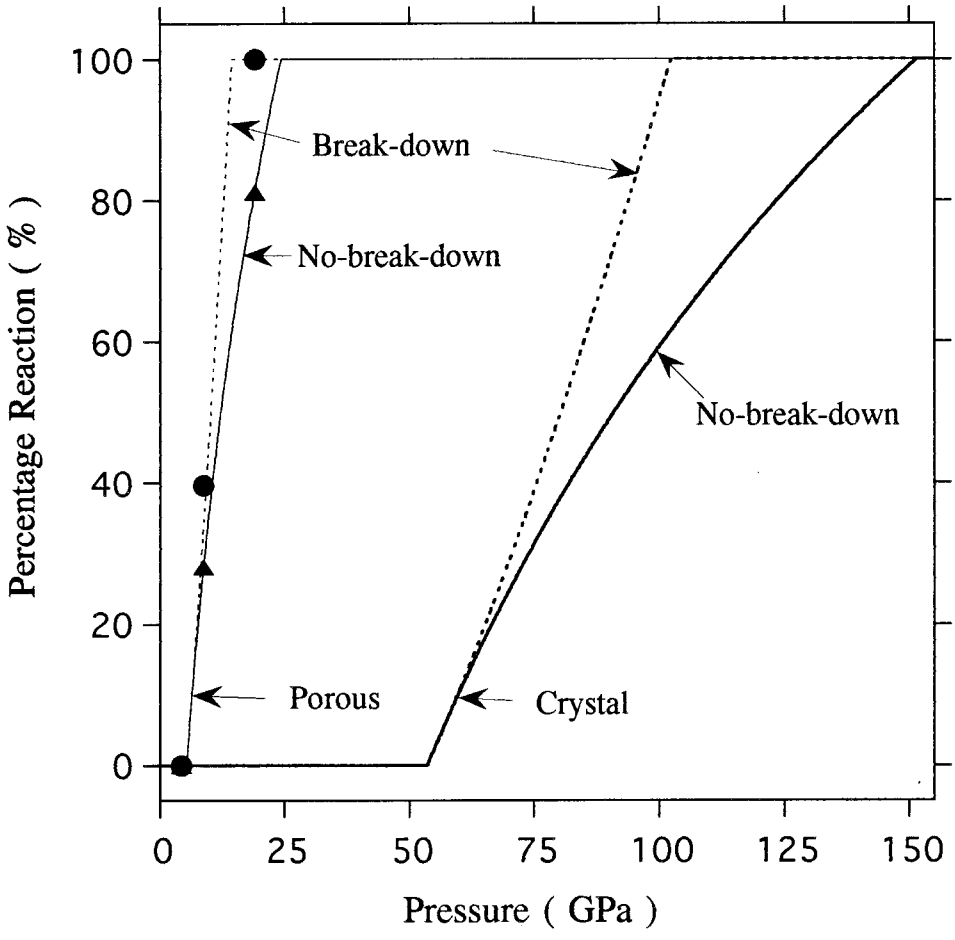

Figure 2.5 Porous and crystal density calcite percentage reaction versus shock pressure. Break-down refers to calculation method where after entropy reaches incipient reaction entropy value (Table 2.4), shock temperature will not increase until the complete reaction entropy criteron is reached. No-break-down refers to method where shock temperature will continue to increase after entropy reaches incipient reaction value. Circles used break-down method, triangles used no-break-down method.

The uncertainties of shock pressure, shock energy (Table 2.2) are calculated from the uncertainties of the initial density, equation of constants (Table 2.3) and the use of Dulong-Petit value approximation for C_v. The uncertainties of the incipient and complete vaporization entropy (Table 2.4, Figure 2.4) are relatively small since they are obtained from well determined experimental data [Robie et al., 1979]. The actual uncertainties, however, could be much larger because of the uncertainties of shock pressure and energy, that are used in performing the entropy increase calculation.

2.4 Results and Discussions

Velocity Profiles and Numerical Simulations

Three shots have been conducted for porous calcite samples, the pressure ranges from 4 to 19 GPa, and the calculated reaction percentage is from 0 to 100% (Table 2.2). Figure 2.6 shows all the profiles. The experimental conditions, shock states, and equation of states parameters can be found in Tables 2.1-2.3.

In order to better understand the dynamic behavior of calcite and to test whether the thermodynamically calculated criteria provide good descriptions for the impact process, numerical simulations were carried out using the one-dimensional Lagrangian finite difference wavecode WONDY [Kipp and Lawrence, 1982] of Chapter 1.

In our simulation, an elastic-perfectly plastic model is again used for the flyer plate, driver plate, buffer and LiF window. The yield strength, Y_o (Table 2.3), is held constant. The von Mises yield condition is used. Since these materials were subject to pressure values far in excess of their yield strengths, strength effects are very small and this simple model provides a good description of their behavior. Parameters used for the simulations are given in Table 2.3.

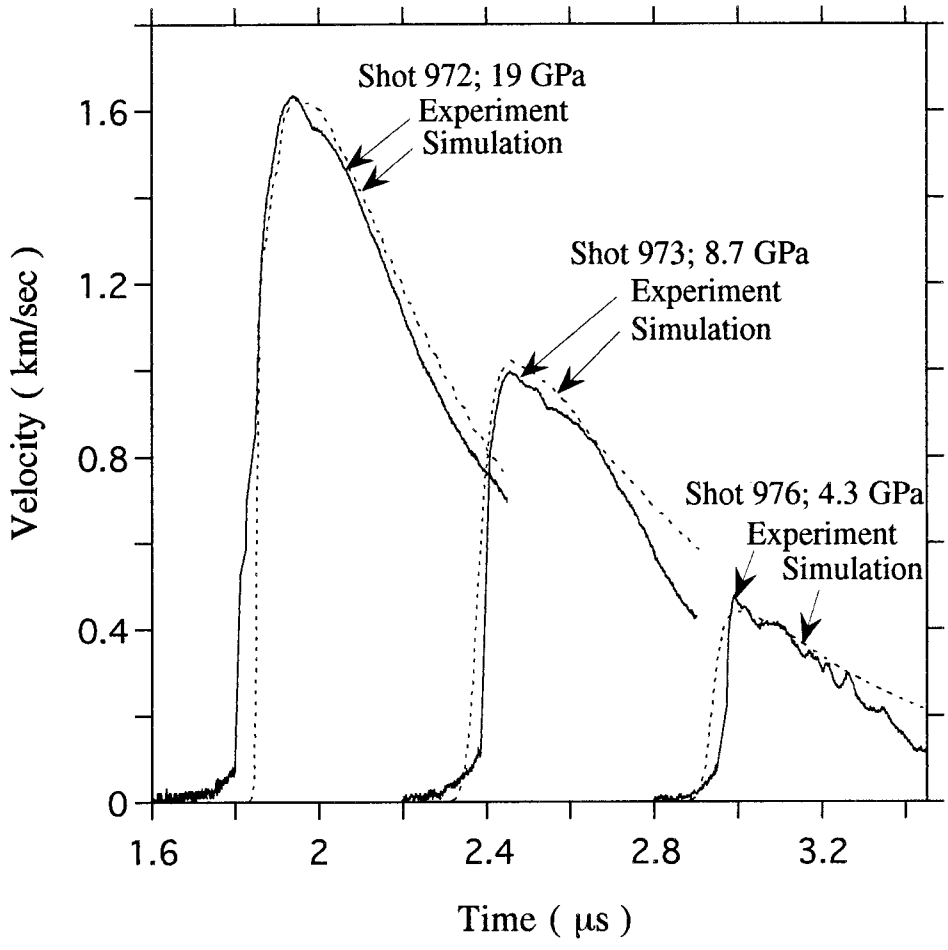

Figure 2.6 Experimental and numerical simulation for calcite. Times of experimental profiles are shifted to best present the results. The time of the simulation are uncertain by about ±50 ns.

For porous calcite experiments, the calculated criterion is applied during the simulation. Since WONDY does not calculate entropy values explicitly for each mesh, approximately equivalent energy criteria were applied (see Table 2.4), instead. This practice may actually lower the criteria values, or overestimate the entropy gain, because part of the energy gain during the complex wave interactions after the sample impacting upon the buffer may arise from isentropic compression.

To avoid the complication of describing a mixture mesh during the simulation, just like in Chapter 1, a mesh is not treated as vaporized until its entropy gain is in excess of the complete reaction entropy value. Once the complete reaction criterion is reached in a mesh, this mesh is immediately treated as vaporized products and described by a new equation of state. The mesh size used is determined by the stability requirement of the simulation [Kipp and Lawrence, 1982].

The equation of state used for the unvaporized sample is the linear shock velocity-particle velocity and Grüneisen equation of state (Table 2.3). For the vaporized sample, the equation of state used is:

$$P=(\gamma-1)\rho E \qquad (2.2)$$

where γ is a constant and was adjusted in the simulation to fit the experimental velocity profiles. Figure 2.6 shows the simulated profiles together with the experimental ones. Reasonably good fits were obtained for shot 972 and 973. For shot 972, we calculate that the sample was completely vaporized by the first shock wave, and the value of γ used in the simulation is 3.4. For shot 973, a thermodynamic calculation shows, about 40% (Table 2.2) of the sample was vaporized by the first shock wave loading. However, after the sample translates across the 2 mm gap and impact the Al6061 buffer, the sample is completely vaporized, as it is subjected to further shock compression. The value of γ used is 5.4. For shot 976, no vaporization occurrs, the simulation fits the experimental profile poorly due to the lack of knowledge of the failure mechanism of very porous (~46%) material at relatively low pressure. The sample thickness of shot 976 was reduced 30% in

the simulation by assuming that particles are ejecting at the sample free-surface upon internal reflection of the initial shock, this reduces the sample's effective thickness. The experiment profiles thus suggest, that once the shock wave reaches the sample's free surface, a layer of sample material is ejected from the free-surface as discrete solid particles. These particles impact the buffer incoherently. As a result, the buffer-LiF window, that is monitored with the VISAR, does not respond to these particles as it does to the impact of a layer of material. The slow ramp increase of the velocity at the beginning of the experimental profile (Figure 2.6) may be the indication of this kind of bombardment. This effect will thus reduce the effective thickness of the sample.

All the simulations shown in Figure 2.6 used the criteria calculated using the break-down method. The break-down method gives a fairly good description of the particle velocity profiles. In order to further test the model's validity and its sensitivity to input parameters, additional simulations were conducted. Shot 972 was used as an example, in which parameters were purposely altered. One parameter is perturbed at a time.

Figure 2.7 shows the experimental profile with simulation results for break-down and no-break-down criteria. The break-down criterion yields a better agreement with the experimental profile. The poor match between the experimental profile and simulation at the front of the profile may be caused by the fact that there is a thin layer of sample material at the sample's free-surface which does not vaporize as the peak break-down pressure is not reached.

Figure 2.8 shows the experimental profile with simulation results for different incipient reaction criteria. The incipient reaction threshold is perturbed by 50% relative to the break-down threshold S_{IR}=1.47 KJ/Kg/K. It is clear that increase or decrease the incipient reaction criterion gives no better fits to the experiment. Thus thermodynamically calculated incipient reaction entropy value fits the data, the present experiments are insensitive to this parameter.

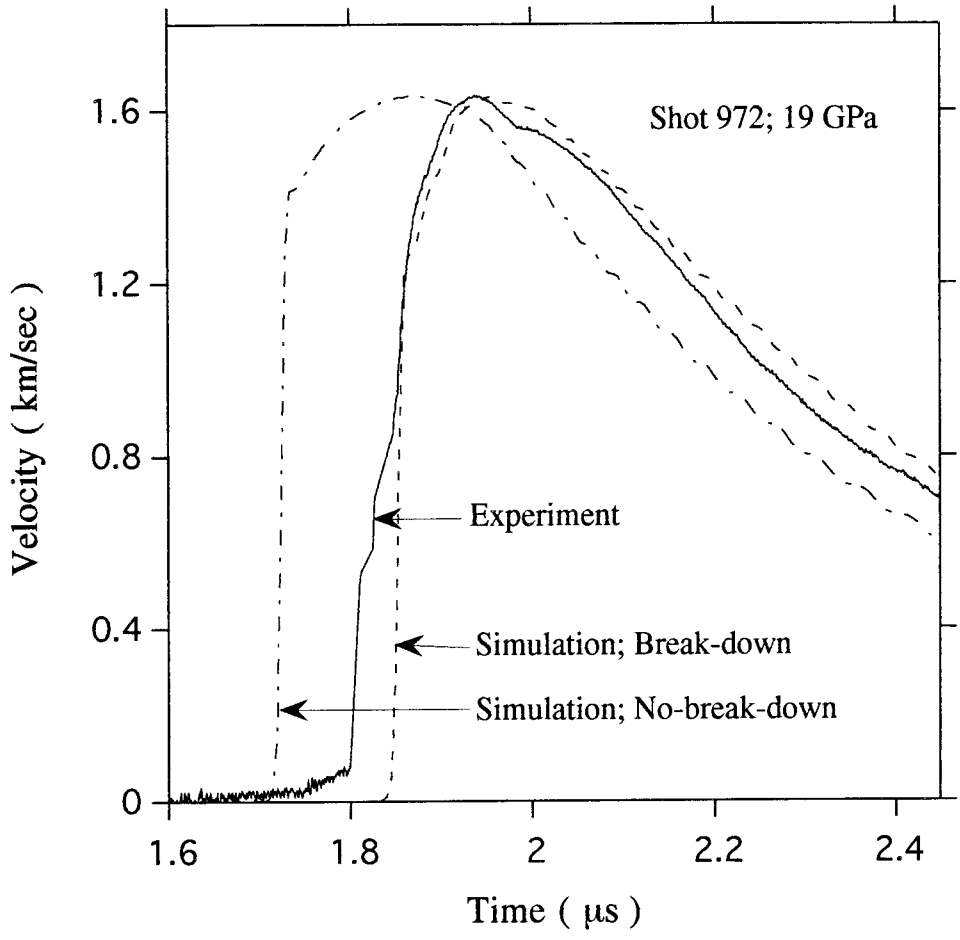

Figure 2.7 Experimental result and numerical simulations for chalk, shot 972. Break-down and no-break-down cases are showed.

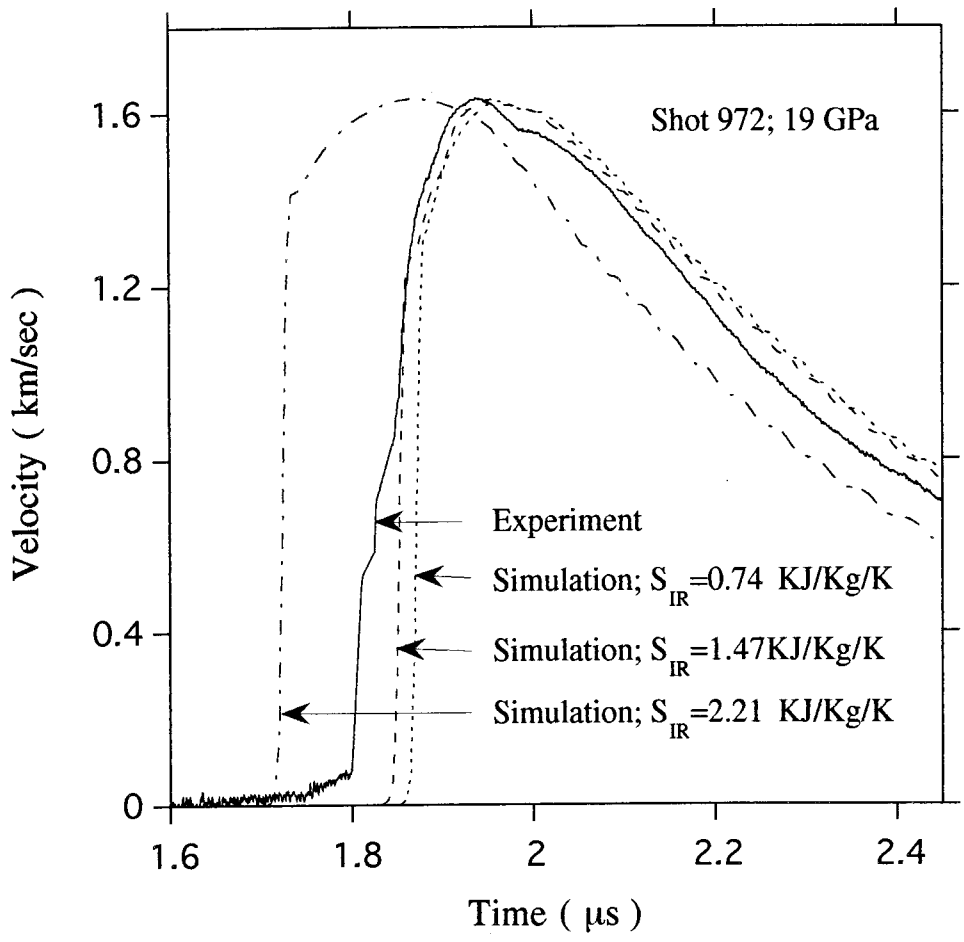

Figure 2.8 Experimental result and numerical simulations for chalk, shot 972. The incipient reaction criterion, S_{IR} (Table 2.4), was purposely perturbed by 50% in numerical simulations.

In Figure 2.9, the entropy difference of products and reactant, ΔS, or $S_{CR} - S_{IR}$ is perturbed by 50%. This comparison also shows that the break-down criterion fits better. Since increase ΔS is equivalent to the no-break-down case, we thus conclude that the break-down criterion is a better approach than the no-break-down approach. Although our calculated incipient reaction pressure (54±6 GPa, Table 2.4) for crystal calcite is much higher than the value obtained from solid shock recovery experiments [Lange and Ahrens, 1986], the complete reaction pressure (103±12 GPa) agrees fairly well with the extrapolated value (~70 GPa) from solid recovery data [Lange and Ahrens, 1986]. The incipient vaporization pressure, 54±6 GPa, is fairly close to that obtained by Vizgirda and Ahrens [1982].

The previous solid recovery experiments tend to over-estimate the amount of devolatilization [Lange and Ahrens, 1986], and their extrapolation also introduce some error. We note that the simulation using the calculated complete reaction criterion fits the experiments reasonably well. Therefore we conclude that the thermodynamically calculated value for the complete reaction pressure of 103±12 GPa is a more accurate value. This value is much lower than the no-break-down value, 151 GPa.

A direct measurement of the shock temperature of calcite crystal versus shock pressure may provide more insight of its vaporization mechanism. However, the shear band heating effect previously observed in calcite [Grady, 1977; Kondo and Ahrens, 1983] may cause some problems in interpretation of such data.

It is understandable that different γ values are needed for different shots (or pressure), since the gas molecules behaves differently at different pressure ranges and deviate greatly from ideal gases. In addition, the composition of vaporized products is a mixture of solid and gas whose composition is expected to vary with varying pressure. For example, high explosive detonation products, which are also a mixture of gas and solid particles (CO_2, CO, C, H_2O, N_2 etc.), can be adequately described by Equation 1.38 using a constant value of γ for release from variant pressures. For example, upon

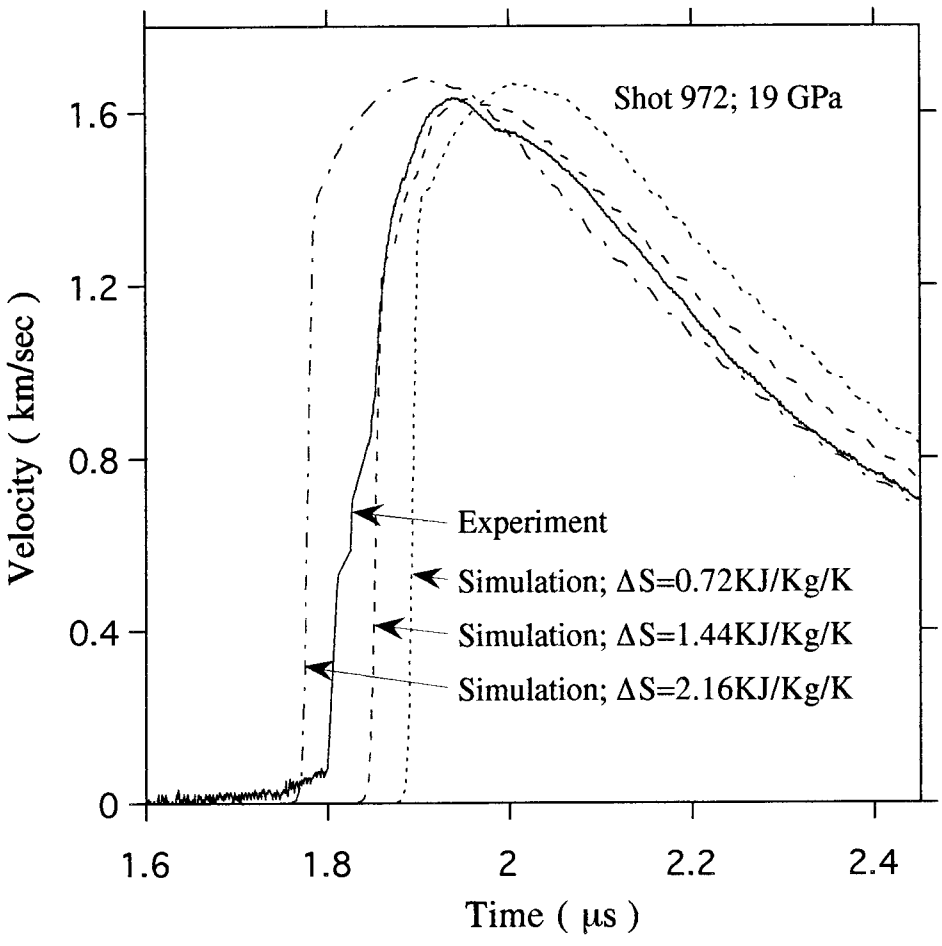

Figure 2.9 Experimental result and numerical simulations for chalk, shot 972. The difference of complete reaction criterion , S_{CR}, and incipient reaction criterion, S_{IR} (Table 2.4), was purposely perturbed by 50% in numerical simulations.

detonation of RDX ($C_3H_6N_6O_6$), γ of the products are equal to 2.48 and 2.98 at 11 GPa and 35 GPa, respectively [Zhang et al., 1979]. Figure 2.10 shows some simulation results for shot 972 using different values of γ to demonstrate its effect.

The sample density, thickness, impact velocity, and the LiF window density are each altered by 2-10%, resulting in no dramatic changes of the simulation profiles. These results are illustrated in Figure 2.11-2.14. Figure 2.15 shows theoretical shock temperatures. These may be used in future shock temperature experiments as initial estimates of expected values.

As in Chapter 1, Tillotson equation of state is also used for chalk to fit the velocity profile. The parameters used are listed in Table 2.5. The velocity profile for Shot 972 is shown in Figure 2.16. The Tillotson equation of state gives a slightly better fit than the no-break-down simulation but not as good as the break-down simulation which uses Equation (2.2) for vaporized products.

Adiabatic release curves in the P-V plane are also calculated and showed in Figure 2.17. Shot 972 is used as an example. The data used are obtained from a mesh in the middle of the sample. To clearly see the characteristics of the release curves, the witness plate and LiF window are removed in these simulations to avoid the compression wave reflecting back after the vaporized products impact the witness plate. Again, the behavior of the vaporized materials, Equation (2.2), gives a different adiabatic curve than Tillotson equation of state. The pressure drops from state A to state B, and then is recompressed to state C and released to D. One may expect this would cause the oscillation of the particle velocity at the Al-LiF interface as in the case of the experiments on $CaSO_4$, but we do not see obvious oscillations both from the experimental observation and numerical simulation (Figure 2.16). The reason for this is that the oscillations caused by stress reverberation as in the case of anhydrite are smoothed out by the porous calcite and the expanding vaporized products before the vaporized materials impact the Al witness plate. To show that stress reverberations do cause oscillations at the Al-LiF

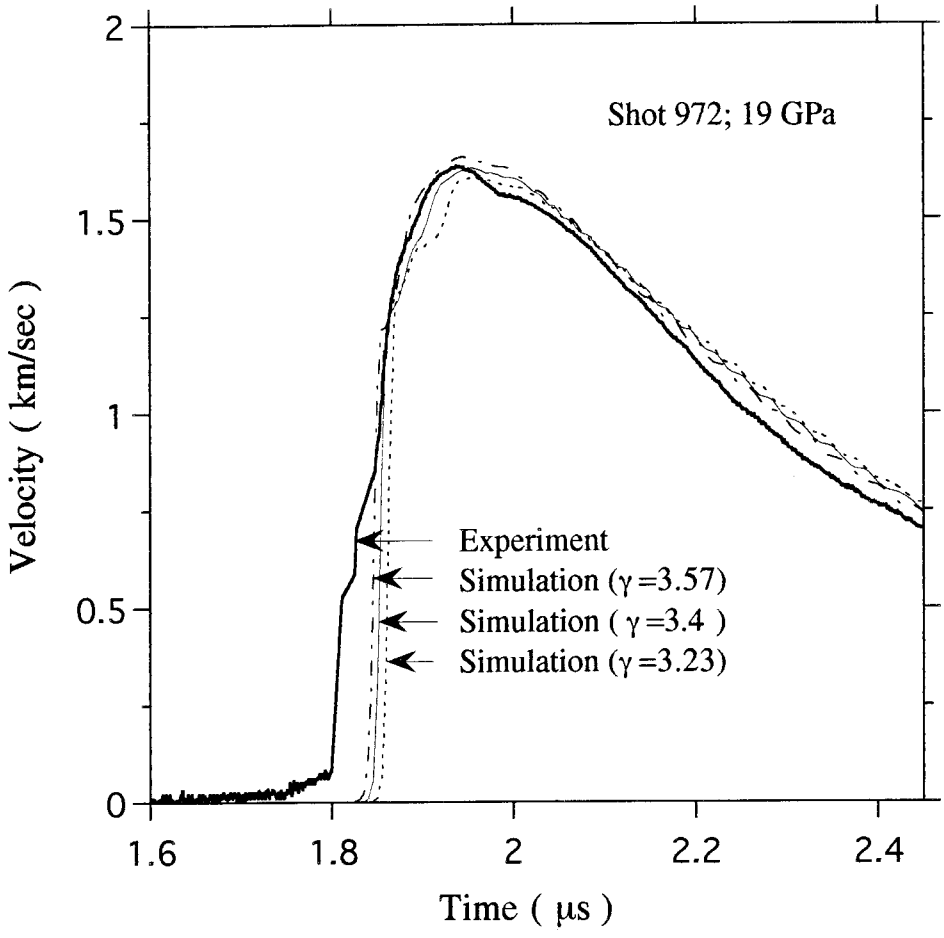

Figure 2.10 Experimental result and numerical simulations for calcite, shot 972. Value of γ was perturbed by 5% to demonstrate its effects in numerical simulations.

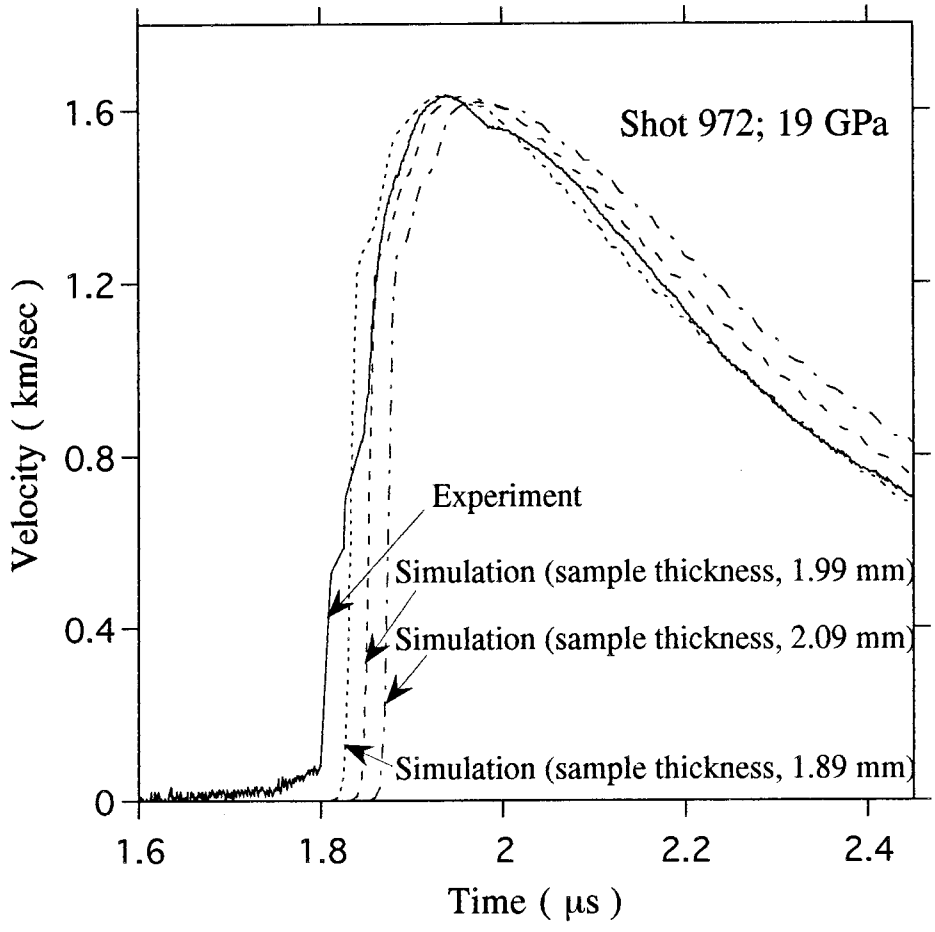

Figure 2.11 Experimental result and numerical simulations for chalk, shot 972. Calcite sample thickness was perturbed by 5% in numerical simulations.

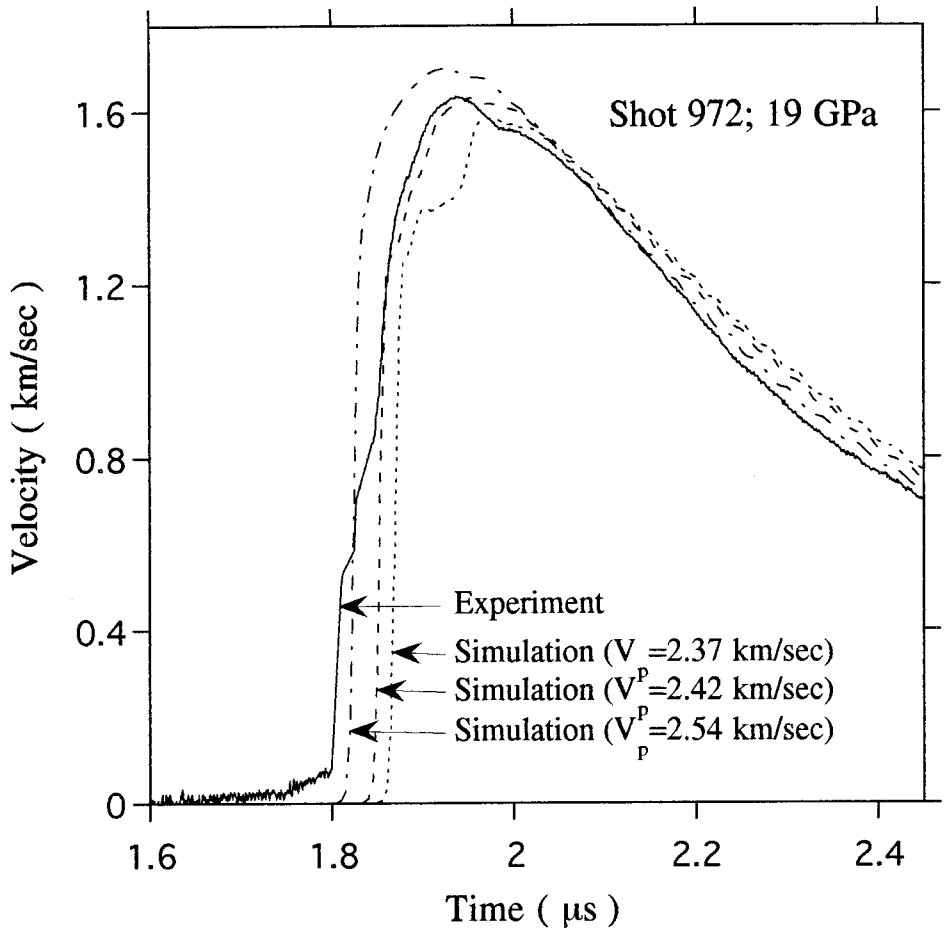

Figure 2.12 Experimental result and numerical simulations for chalk, shot 972. Impact velocity was perturbed by 5% in numerical simulations.

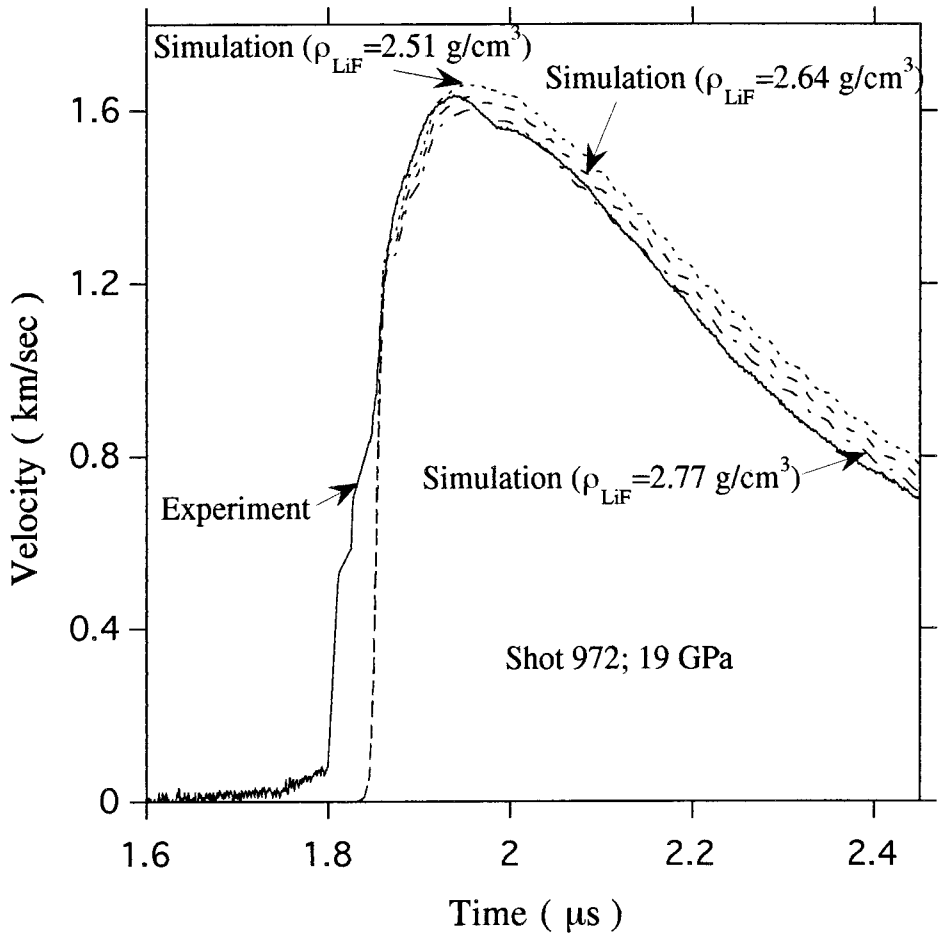

Figure 2.13 Experimental result and numerical simulations for chalk, shot 972. LiF window's density was perturbed by 5% in numerical simulations.

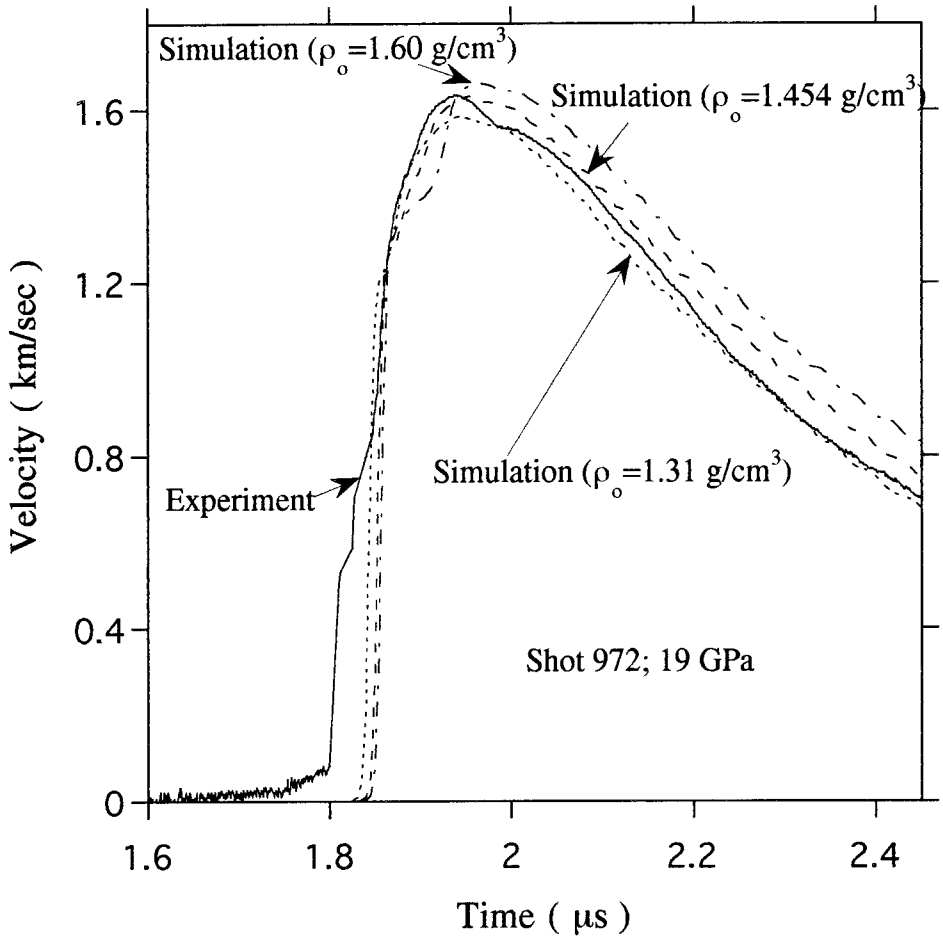

Figure 2.14 Experimental result and numerical simulations for chalk, shot 972. Calcite sample density was perturbed by 10% in numerical simulations.

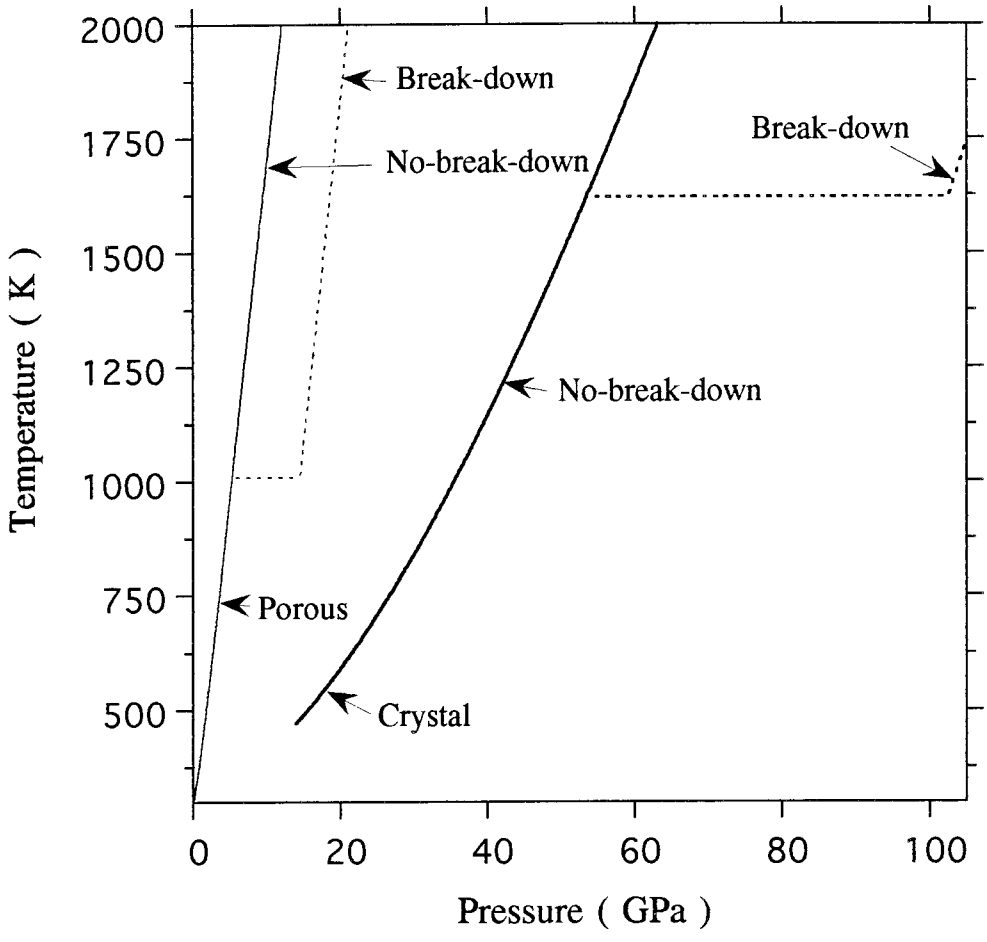

Figure 2.15 Shock temperature versus shock pressure of porous and crystal calcite. Break-down refers to calculation method taking into account chemical dissociation, no-break-down refers to calculation without taking into account chemical dissociation.

Table 2.5 Parameters of Tillotson Equation of States of Chalk

Material	ρ_o (Kg/m^3)	a	b	A (GPa)	B (GPa)	E_o (MJ/Kg)	E_{iv} (MJ/Kg)	E_{cv} (MJ/Kg)	α	β
Chalk	1400±40	0.5	1.0	0.65	0.72	3.61	0.97	4.64	5.0	5.0

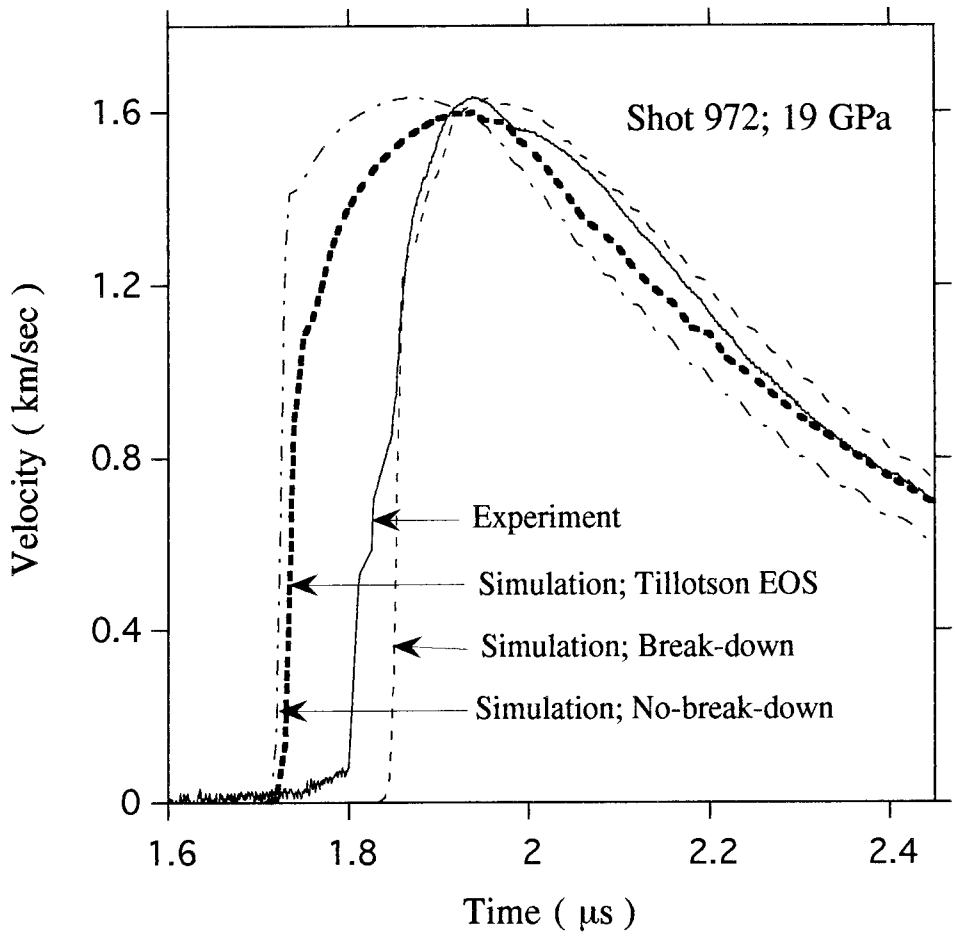

Figure 2.16 Experimental result and numerical simulations for porous calcite, shot 972. Different equation of states have been used in simulations.

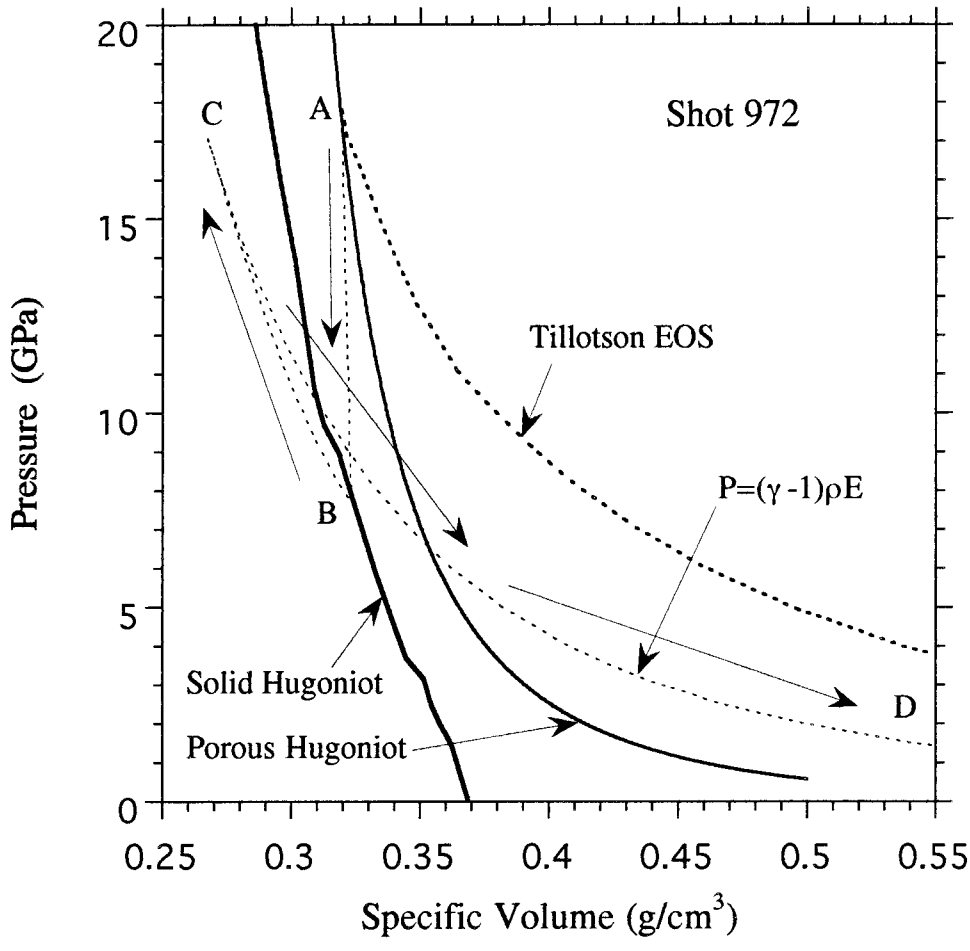

Figure 2.17 Adiabatic curves on P-V plane using different equation of states for porous $CaCO_3$ in relation to crystal Hugoniot. Tillotson parameters used are listed in Table 2.5

interface, crystal density calcite instead of porous calcite is used in the simulation of Shot 972 (Figure 2.18). The thickness of the crystal calcite (0.97mm) is determined by keeping the mass per unit area the same as the porous sample. Other dimensions are kept the same. It is clear that the wave reverberations causes oscillations but they are smoothed out by the porous sample and the vaporized product expansion.

2.5 Summary

Thermodynamic calculations of the shock states achieved upon loading either porous or crystal $CaCO_3$ demonstrate that melting does not occur upon loading and melting cannot be used to explained the present experimental results. Incipient and complete reaction criteria for porous and crystal density calcite to vapor and CaO have been carried out using two methods. The first method is the one previously used by many authors in which no chemical bonds are assumed to break upon compression along the Hugoniot, vaporization occurrs upon adiabatic release. The second method assumes incongruent break down of $CaCO_3$ to CaO and CO_2 along the Hugoniot. The first method predicts much higher shock pressure values for devolatilization upon isentropic release. The shock pressure required for complete reaction of crystal calcite to CaO and CO_2 is 151±18 GPa using first (no-break-down) method while the second (break-down) method predicts 102±12 GPa which is close to previous calculations based on shock recovery data [Lange and Ahrens, 1986]. The energy required to complete vaporize crystal calcite is 2.6 MJ/Kg, which is much larger than the Calcite I—Calcite IV phase change energy, ΔE_{tr} (0.02 MJ/Kg). For porous calcite (54% crystal density), the incipient and complete vaporization pressure are 5.4±1.9 and 14.6±3.8 GPa, respectively.

Shock vaporization experiments were carried out for porous calcite up to 19 GPa. Velocity histories of aluminum-LiF window interface were measured using velocity

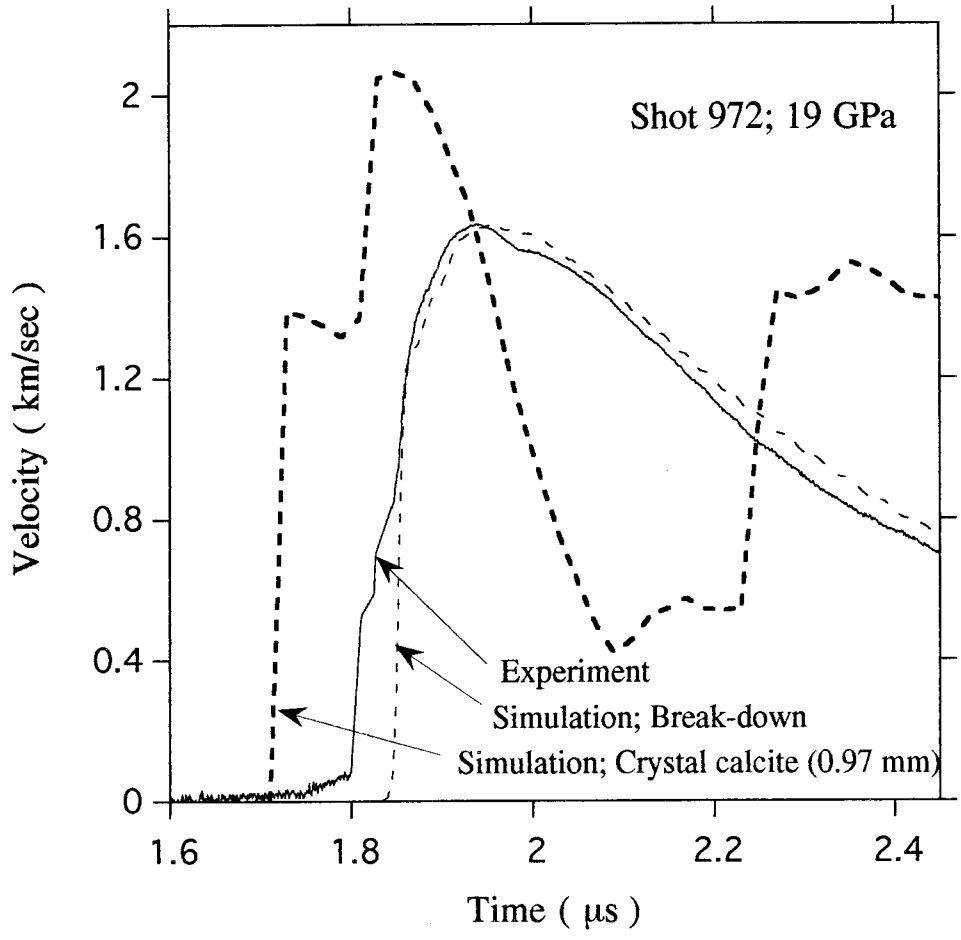

Figure 2.18 Experimental result and numerical simulations for porous calcite, shot 972. Crystal density sample has been used in one simulation.

interferometer system for any reflector (VISAR) [Barker and Hollenbach, 1972] to study the shock vaporization mechanism and dynamic properties of the products.

A Lagrangian one-dimensional wave propagation code (WONDY) was used to simulate the measured velocity profile. We found that the vaporization criteria calculated using the break-down method provides better agreement with the experimental profiles than the ones obtained using the no-break-down method. The vaporized products can be described by equation in the form $P=(\gamma-1)\rho E$, where γ is a constant whose value varied from 5.4 to 3.4 upon release from shock pressures of 8.7 to 19 GPa.

Since the immediate vaporization assumption fits the data well in the simulation, we infer that the decomposition rate of the calcite is very fast, possibly a few nanoseconds after the complete reaction criterion is reached.

Chapter 3

On the Global Effects of the Chicxulub Impact with New Shock Wave Data

3.1 Introduction

3.1.1 Background

Alvarez et al. [1980] proposed that a global, impact-induced , dust cloud from the impact of an asteroid or comet drastically reduced solar radiation, and this caused the previously recognized mass extinctions of some 80% marine and terrestrial genera at the Cretaceous/Tertiary (K/T) boundary. This proposal has led to extensive studies of various impact-induced extinction mechanisms. Extinction mechanisms that have been proposed are: impact-generated H_2O and/or CO_2-inducing greenhouse global warming [Emiliani et al., 1982; O'Keefe and Ahrens, 1989], dust-induced global cooling [Alvarez et al., 1980; Pollack et al., 1983], nitric acid rain [Crutzen, 1987; Prinn and Fegley, 1987], global forest fires inducing solar insolation from soot [Wolbach et al., 1985], severe global radiative heating upon reentering of impact ejecta [Melosh et al., 1990] and global cooling from stratospheric H_2SO_4 aerosols induced by volatilization of SO_2 and SO_3 from anhydrite and gypsum at the impact site, Chicxulub, Yucatan, Mexico [Brett, 1992; Sigurdsson et al., 1992; Pope et al., 1994].

The Chicxulub impact structure has recently been recognized as the leading candidate for the crater(s) associated with the Cretaceous/Tertiary bolide [Hildebrand et al., 1991; Sigurdsson et al., 1991a; Sigurdsson et al., 1991b; Blum and Chamberlain, 1992; Swisher et al., 1992]. Strong supporting evidences relating the Chicxulub, Yucatan, crater with the world-wide extinction include the following:

(1) Tektites, presumably representing fused target material, from Beloc, Haiti and Mimbral, Mexico, K-T sections show the glass source terrane is likely to be a continental margin [Sigurdsson et al., 1991a, 1991b]. This environment contains sediments rich in carbonate and sulfate, which is consistent with Chicxulub stratigraphy. Oxygen and strontium isotope analyses [Blum and Chamberlain, 1992] also indicate the Chicxulub crater as the source for the tektite-like glassy ejecta, which, in most locations throughout the world, has been weathered to various clays.

(2) The tektites and Chicxulub melt rock have been dated by $^{39}Ar/^{40}Ar$ and found to be coeval within 0.1 m.y. at 65 m.y. [Swisher III et al., 1992]. Moreover, the Manson, Iowa, impact structure which previously believed to have a 65 m.y. age, and a possible K/T bolide induced crater has been recently redated at 74 m.y. [Izett et al., 1993]. Thus, at the present time, the Chixulub crater is the only known crater site of the K/T extinction bolide.

(3) Tsunami deposits exactly at the K-T boundary [Bourgeois et al., 1988; Smit et al., 1992], predicted by O'Keefe and Ahrens [1982], which have now been recognized to occur around the present Gulf of Mexico. This supports the hypothesis of a nearby impact site.

The dominance of calcium carbonate (calcite) and calcium sulfate minerals (anhydrite and gypsum) in the upper 3 km of the Chicxulub section (in the sequence of limestone, anhydrite-dolomite conglomerates, limestone-dolomite and anhydrite-gypsum layers [Koeberl, 1993]) has prompted active research on the effects of their

devolatilization upon impact [Chen et al., 1994; Brett, 1992; Sigurdsson et al., 1992; Pope et al., 1994; Alvarez et al., 1995].

3.1.2 Previous Studies of Shock and Compression Effects in Carbonates

Previously, two low-pressure phase transitions in calcite, calcite II and III, were discovered by Bridgman [1939]. Later, compressive behavior of $CaCO_3$ under static and dynamic loading have been the subject of many studies [Jamieson, 1957; Adadurov et al., 1961; Ahrens and Gregson, 1964; Ahrens et al., 1966; Singh and Kennedy, 1974; Huang and Wyllie, 1976; Fiquet et al., 1994]. Above about 10 GPa, the single-crystal calcite [Ahrens and Gregson, 1964], polycrystalline calcite [Adadurov et al., 1961; Kalashnikov et al., 1973; van Thiel et al., 1977] and crystal aragonite [Vizgirda and Ahrens, 1982] Hugoniots are very similar, suggesting transformation to a similar high-pressure polymorph of $CaCO_3$ we designate as $CaCO_3$ IV [Vizgirda and Ahrens, 1982] in the present study. Release isentropes for polycrystalline calcite rocks shocked to pressures up to about 40 GPa have been determined using laser interferometry [Schuler and Grady, 1977; Grady et al., 1978; Grady, 1983] and electromagnetic particle velocity gauges [Murri et al., 1975; Larson and Anderson, 1979]. Murri et al. [1975] employed electromagnetic particle gauges to determine release paths for selected carbonate rocks (porosity 0 and 15%) shocked to between 10 and 30 GPa. In this pressure range, the initial release paths lie at greater densities than the Hugoniot. Release paths for single-crystal aragonite shocked to pressures up to 40 GPa have been determined using buffer and inclined mirror techniques [Vizgirda and Ahrens, 1982]. For shock pressures up to about 13 GPa, the release paths are steep, and maximum post-shock densities are greater than the initial densities. For shock pressures between about 13 and 40 GPa, the release paths generally lie close to the Hugoniot, and maximum post-shock densities are less than or equal to the initial density. The steep release adiabats indicate an onset of a phase

transformation. This phenomenon has been observed for a number of silicates, including quartz [Grady et al., 1974], plagioclase feldspar [Ahrens et al., 1969a, b], and olivine [Jackson and Ahrens, 1979] and has been interpreted to indicate retention of the denser high pressure phase during the initial stages of unloading.

3.1.3 Present Results

In this study, the first complete impact vaporization experimental results for $CaCO_3$ and $CaSO_4$ [Chapter 1 and 2] are used to develop criteria for incipient and complete reaction criteria for calcite and anhydrite. The amount of CO_2 and SO_2 degassed during the Chicxulub impact were reestimated and their effects on the global climate are discussed.

3.2 Incipient and Complete Vaporization Criteria for Calcite and Anhydrite

Experiments

Crystal density calcite shock recovery experiments [Lange and Ahrens, 1986] have demonstrated that calcite crystal starts to lose CO_2 at ~10 GPa and total vaporization occurs at ~70 GPa. For anhydrite, however, no SO_2 loss was found up to 42 GPa in solid recovery experiments [Chen et al., 1994].

Impact vaporization experiments on porous calcite (Dover chalk, ~54% crystal density) and anhydrite (70% crystal density) have been conducted recently [Chapter 1 and 2]. In these experiments, a velocity interferometer (VISAR) [Duffy, 1992; Barker and Hollenbach, 1972] was used to record the velocity history imparted to witness plates which are accelerated by the solid and gaseous decomposition products produced by shock loading. Numerical modeling of the velocity profiles demonstrated that the onset of

vaporization upon unloading from shock pressures for porous calcite (56% crystal density) and anhydrite (70% crystal density) are 5.4±1.9 and 26.9±1.1 GPa, respectively, and complete vaporization occurs at 14.6±3.8 and 67±6 GPa, respectively. These values are in good agreement with thermodynamic calculations. Thermodynamic calculations using a revised version of the entropy method [Zeldovich and Raizer, 1966; Ahrens, 1972; Vizgirda and Ahrens, 1982] shows that incipient and complete vaporization occurs in crystal density calcite and anhydrite over the ranges 54-103 GPa and 81-155 GPa, respectively. The calculation method is illustrated briefly in the next section. Detailed description of the vaporization experiments, numerical simulation and thermodynamic calculations can be found in Chapter 1 and 2.

Thermodynamic Calculations

In the study of shock-induced vaporization (or reaction), the incipient and complete reaction criteria are of great interest. Vizgirda and Ahrens [1982], using the entropy method [see, e.g., Zel'dovich and Raizer, 1967; Ahrens and O'Keefe, 1972], calculated the incipient and complete vaporization criteria for calcite and aragonite. The entropy method compares the entropy value along the release path with the entropy of vaporization at 1 bar. Since release is an isentropic process, the entropy at a release pressure of 1 bar is the same as that of the Hugoniot state. In turn, the entropy along the Hugoniot relative to standard state entropy can be determined by thermodynamic calculation. Vizgirda and Ahrens [1982] found that the incipient vaporization shock pressures for calcite and aragonite are 40±5 GPa and 66±7 GPa, respectively. The complete vaporization pressures for both calcite and aragonite are above 100 GPa. During the calculation of complete vaporization, however, the chemical reaction effect was not taken into account, which will be explained in the following. Tyburczy and Ahrens [1986], using the entropy method, estimated the shock vaporization of Dover chalk and

found that at ~10 GPa, about 90% chalk vaporized. In this section, the entropy method is again employed during the thermodynamic calculation and the chemical dissociation effect is taken into account.

The reactions we considered here are:

$$CaCO_3 \rightarrow CaO + CO_2 \uparrow \quad (3.1)$$

$$CaSO_4 \rightarrow CaO + SO_2 \uparrow + \frac{1}{2} O_2 \uparrow \quad (3.2)$$

The entropy excess required for incipient reaction is:

$$S_{IR} = \int_{T_o}^{T_{IR}} \frac{C_p}{T} dT \quad (3.3)$$

where T_o is ambient temperature, T_{IR} is the incipient reaction temperature at which the sums of Gibbs formation energies for the reactants and products are equal, C_p is the heat capacity at atmospheric pressure [Robie et al., 1979].

Excess entropy required for complete reaction is:

$$S_{CR} = S_{IR} + \Delta S \quad (3.4)$$

where ΔS is the entropy difference between products and reactants at T_{IR} , 1 bar pressure.

The entropy calculation along the Hugoniot is illustrated in Figure 3.1, entropy gain in the shocked state (and in the post-shock state assuming isentropic release) is:

$$\Delta S_h = \Delta S_{tr} + \int_{T_s}^{T_h} \frac{C_v}{T} dT \quad (3.5)$$

where ΔS_{tr} is the entropy change from low pressure phase (LPP) to high pressure phase (HPP) at zero pressure (path I) and is given by:

$$\Delta S_{tr} = S_{HPP} - S_{LPP} \quad (3.6)$$

$$T_S = T_O \exp[\Gamma(1 - V/V_O)] \quad (3.7)$$

T_s is the temperature of isentropic compression from initial volume V_{oh} (HPP) at temperature T_o to Hugoniot volume V_h at isentropic pressure P_s (path II), Γ is the Grüneisen parameter. Γ/V=const. is assumed in deriving this equation.

The Hugoniot temperature is determined by (path III):

$$\int_{T_s}^{T_h} C_v dT = E_h - E_s - \Delta E_{tr} \quad (3.8)$$

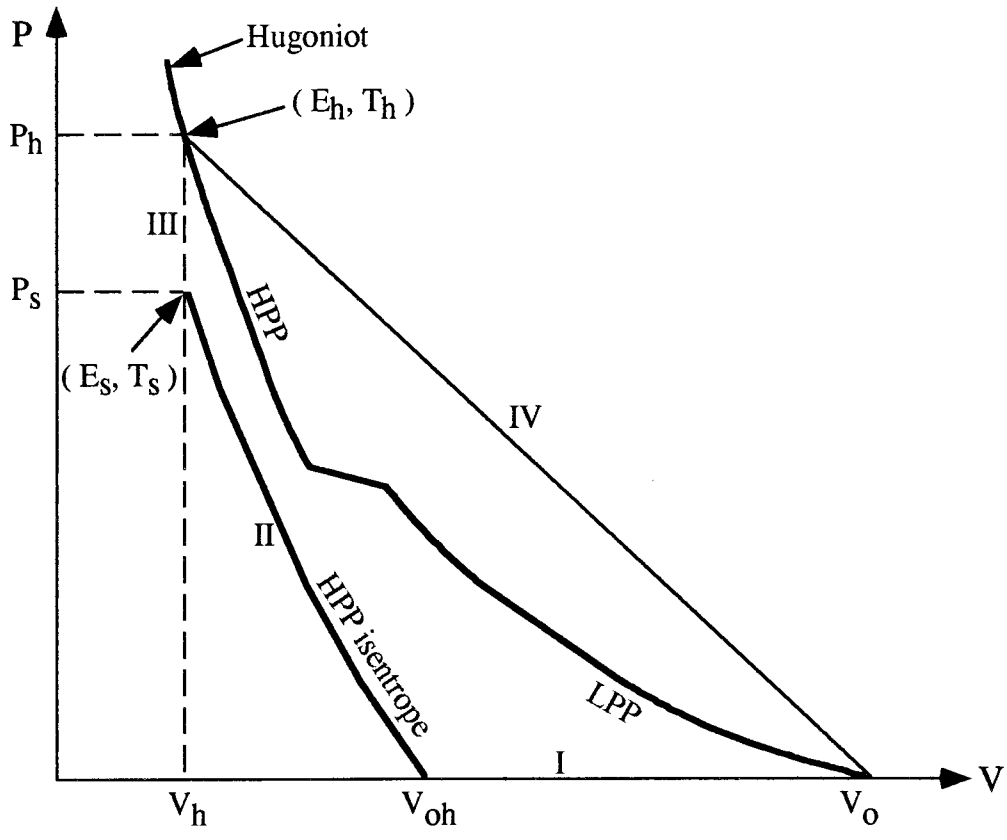

Figure 3.1 Thermodynamic calculation paths on P-V plane.

The Hugoniot energy is given by (path IV):

$$E_h = \frac{1}{2} P_h (V_o - V_h) \tag{3.9}$$

The isentropic energy is given by (path II):

$$E_s = -\int_{V_{oh}}^{V_h} P_s dV \tag{3.10}$$

The isentropic pressure is given by the Murnaghan equation (path II):

$$P_s = \frac{K_{os}}{K_{os}'} [(\frac{V_{oh}}{V_h})^{K_{os}'} - 1] \tag{3.11}$$

And the Hugoniot pressure is given by:

$$P_h = \frac{C_o^2 \eta / V_o}{(1 - S\eta)^2} \tag{3.12}$$

where ΔE_{tr} is phase transition energy at ambient pressure and temperature corresponding to the change in entropy, ΔS_{tr}. K_{os} is crystal density bulk modulus and $K_{os}'=(\partial K/\partial P)_{s, p=0}$, C_o and S are material constants for shock wave in solids, $\eta = 1 - V/V_o$, the constants used are given in Table 3.1.

The reaction fraction is given by:

$$R_f = \frac{\Delta S_h - S_{IR}}{S_{CR} - S_{IR}} \tag{3.13}$$

In the above formulation, it should be point out that no chemical reaction is taken into account. This may not be reasonable since once the shock temperature reaches the incipient reaction temperature T_{IR}, chemical bonds will start to break down, and the Hugoniot energy, in part, will be consumed by breaking bonds instead of just heating up the sample. A simple and reasonable first-order approach is to assume that after the Hugoniot temperature reaches T_{IR}, the temperature will be kept constant and all the Hugoniot energy increase, ΔE_{TIR}, will be consumed only by chemical dissociation until the dissociation is completed. Thus the entropy increase, ΔS_{TIR}, is calculated by:

$$\Delta S_{TIR} = \Delta E_{TIR} / T_{IR} \tag{3.14}$$

Radousky et al. [1986] has, in N_2 shock compression experiments, observed the Hugoniot temperature increases less rapidly with increasing shock pressure as N_2

Table 3.1 Constants for Shock Thermodynamic Calculations

Material	ρ_O (g/cm^3)	K_{OS} (GPa)	K_{OS}'	C_O (km/sec)	S	Γ_O	ΔE_{tr} (MJ/Kg)	ΔS_{tr} (MJ/Kg/K)	Refs.
Calcite (LPP)	2.701	71.7±1.8	4.76±0.6	3.71±0.03	1.435±0.013	1.53			a
Calcite (HPP)	3.100	96.5	4.0	5.58	1.25	1.183	0.02	0.067	a
Anhydrite (LPP)	2.97	38.5±1.3	6.0±0.2	3.60±0.06	1.75±0.05	2.5			b
Anhydrite (HPP)	3.68	162±11	4.4±0.1	3.25±0.11	1.72±0.03	2.44	0.085	0.24	b, c

LPP-low pressure phase; HPP-high pressure phase; a, Ahrens et al., 1995; b, Simakov et al., 1974; c, Chapter 1.

molecules start to dissociate. In this study, two calculational methods are used and compared. We define these as: no-break-down and break-down method, respectively.

The calculated incipient and complete reaction entropy and corresponding pressures are listed in Table 3.2. Figure 3.2 and 3.3 show the calculated results of entropy gain versus Hugoniot pressure for both crystals. The break-down method gives a much steeper increase of entropy gain than the no-break-down method after the entropy gain reaches the incipient reaction value. Figure 3.4 and 3.5 give the percent reaction versus shock pressure. It is clear that the no-break-down method gives much higher shock pressure to complete reaction. Values obtained using the break-down method are given in Table 3.2. Since the calculated criteria values using the break-down method for porous calcite and anhydrite fits the experimental particle velocity profile closely [Chapter 1 and 2], we conclude that the break-down method provides a more accurate estimate at incipient and complete reaction criteria. When compared to the solid recovery experiments, the calculated results agrees fairly well with the experimental results. For calcite, the calculated complete reaction pressure, 103±12 GPa, is fairly very close to the extrapolated value, ~70 GPa, considering the fact that the recovery experiments tend to over estimate the amount of degassed volatile and thus gives a lower complete reaction pressure [Lange and Ahrens, 1986]. The discrepancy between the calculation and recovery experiment for incipient reaction pressure can be explained by shear band heating effect [Grady, 1977], which is caused by shear instability right behind the shock wave. These zones of intense heating would cause devolatilization to begin at much lower pressure than those calculated on the basis of continuum models. Further evidence for shear band heating are shock temperature measurements at 40 GPa on single-crystal calcite. These yield a color temperature of 3700 K, which is over twice the Hugoniot temperature from continuum thermodynamic models, with an emissivity of 0.0025 [Kondo and Ahrens, 1983]. The low emissivity implies that only a small fraction of the crystal is hot. Again this is in agreement with the shear band heating hypothesis.

Table 3.2 Incipient and Complete Reaction Parameters

Material	ρ_O (g/cm^3)	P_{hIR} (GPa)	P_{hCR} (GPa)	S_{IR} (KJ/Kg/K)	S_{CR} (KJ/Kg/K)
Calcite	2.701	54±6	103±12	1.47±0.07	2.91±0.13
Anhydrite	2.97	81.0±6.5	155±13	2.12±0.08	3.73±0.14

ρ_O is initial density, P_{hIR} is incipient reaction Hugoniot pressure, P_{hCR} is complete reaction Hugoniot pressure, S_{IR} is incipient reaction entropy, S_{CR} is complete reaction entropy.

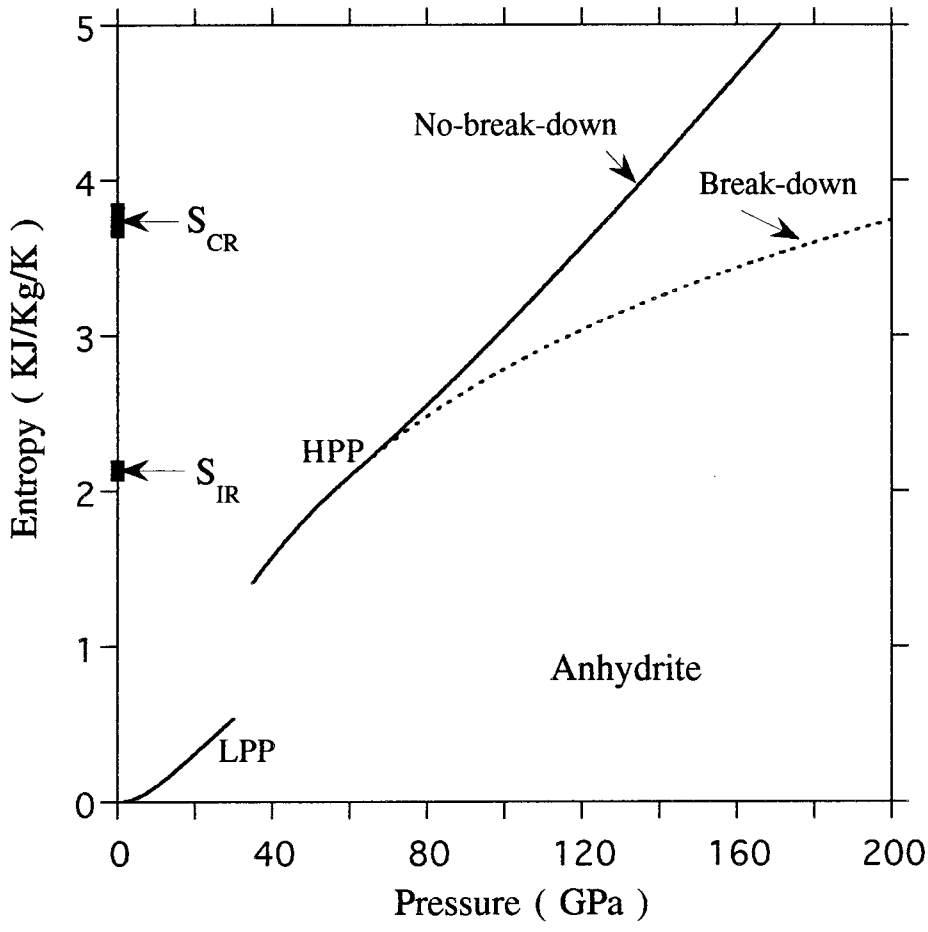

Figure 3.2 Entropy gain versus shock pressure along the Hugoniot for anhydrite using break-down and no-break-down methods, respectively.

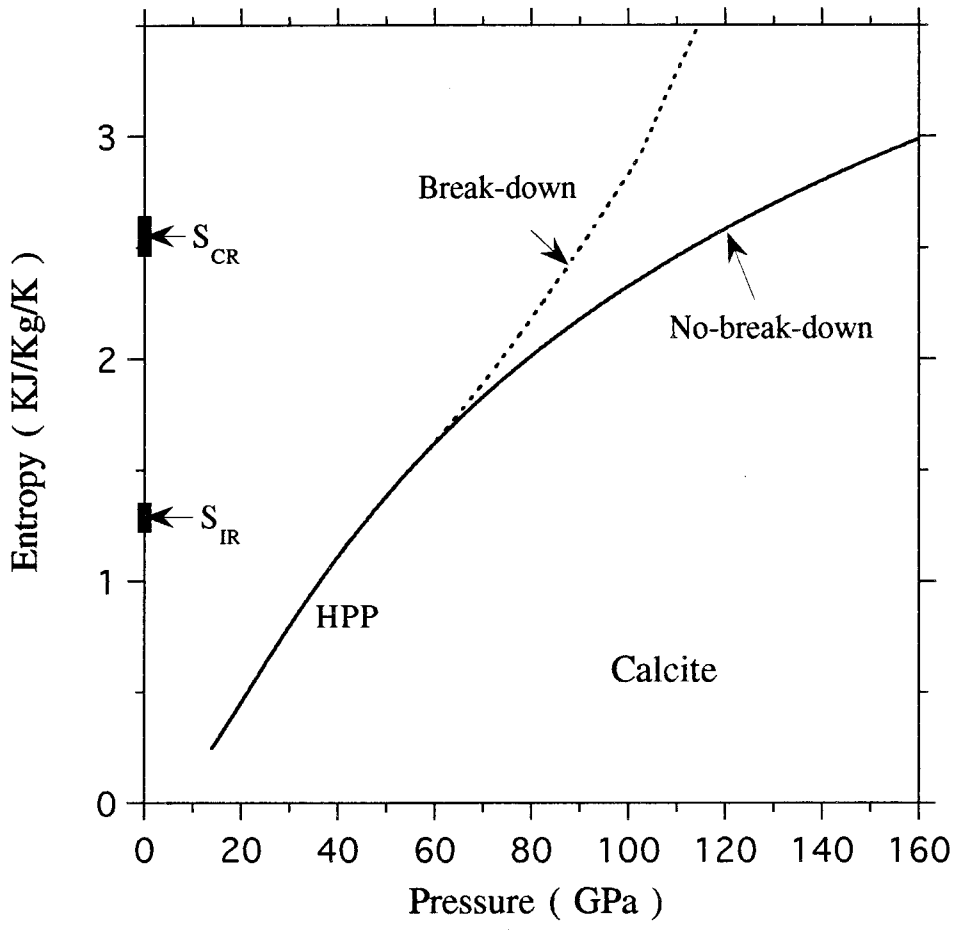

Figure 3.3 Entropy gain versus shock pressure along the Hugoniot for calcite using break-down and no-break-down methods, respectively.

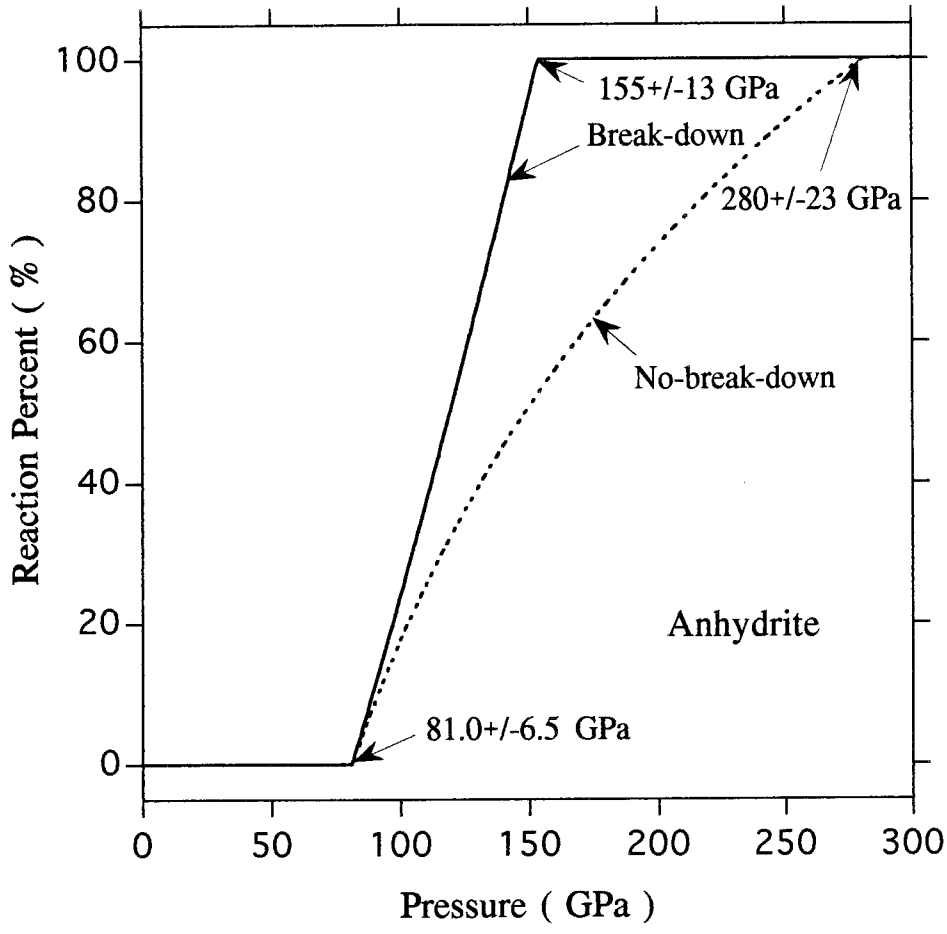

Figure 3.4 Reaction percent versus shock pressure along the Hugoniot for anhydrite using break-down and no-break-down methods, respectively.

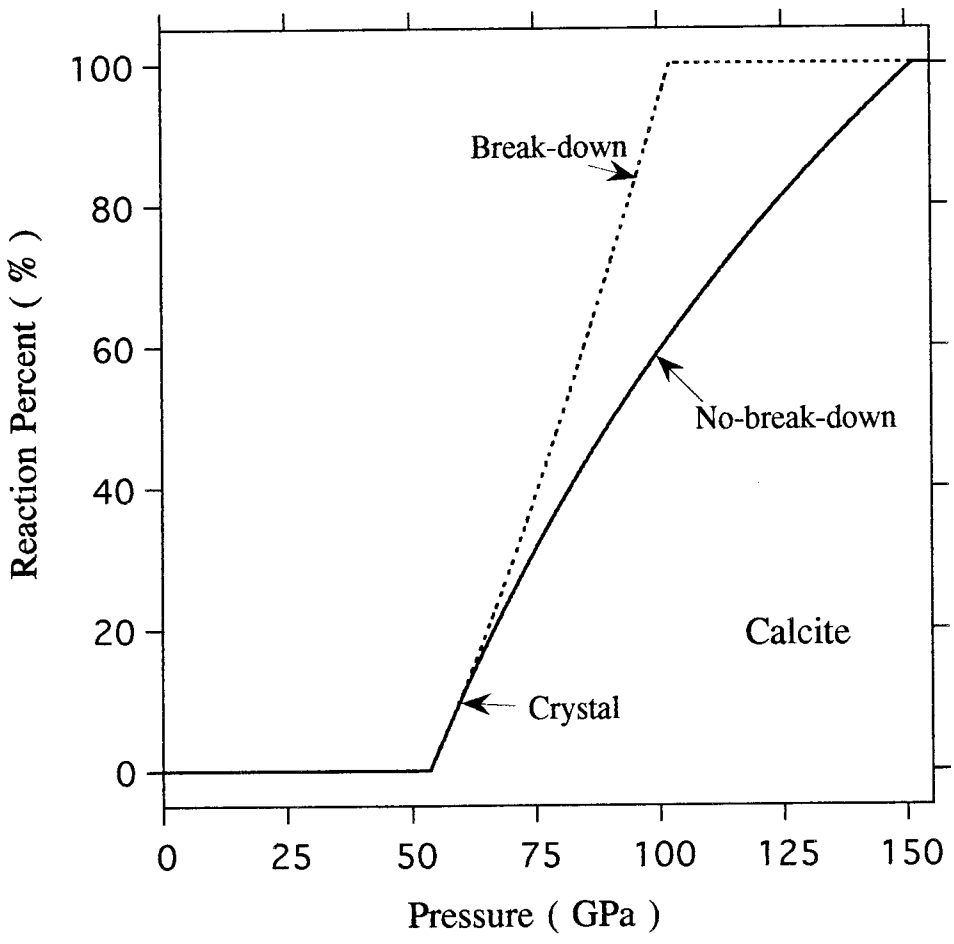

Figure 3.5 Reaction percent versus shock pressure along the Hugoniot for calcite using break-down and no-break-down methods, respectively.

For anhydrite, since recovery experiments up to 42 GPa yield no evidence of vaporization and shows no sign of shear band heating, we conclude that both the calculated incipient and complete reaction pressures of Table 3.2 a valid basis for anhydrite devolatilization calculations.

3.3 CO_2 and SO_2 Releases from Chicxulub Impact

Pressure Decay in the Transient Chicxulub Crater

Previous studies on crater formation mechanisms give formulae for pressure decay with distance R along the centerline in a transient crater [Ahrens and O'Keefe, 1977; O'Keefe and Ahrens, 1977; Holsapple, 1993]. For example, Ahrens and O'Keefe [1977] calculated the shock pressure decay for gabbroic anorthosite or iron meteorites cratering a planetary anorthosite target and fit their calculations with two branches using exponential functions of the form:

$$\log_{10}(P/\text{Mbar}) = a[\log_{10}(R/R_o)] + b \qquad (3.15)$$

where R_o is the radius of the meteorite and parameters a (<0) and b assume different values for different targets and in the near- and far-field. The Schmidt-Holsapple [Holsapple, 1993] scaling breaks down the pressure decay in large craters into four ranges: near source, strong shock, intermediate shock and material strength regimes. In each of these the peak shock pressure decays exponentially with normalized distance R/R_o and each range can be fit to equation (3.15) with different value of a (<0) and b. In evaluating the amount of devolatilization upon impact, it is important to establish the peak shock pressure contours. Due to the rarefaction waves propagating downward from the surface of the target, the peak pressure contours deviate from a hemispherical surfaces because of the attenuation resulting from rarefaction waves propagating from the free surface. This makes the evaluation more cumbersome. Chen et al. [1994] modified the

simple centerline peak shock pressure model, equation 3.15, by assigning each hemispherical shell an ' average ' pressure which is lower than the centerline pressure. The radii for the average pressure hemisphere were determined by choosing volumes of vaporized and melted rocks that were in agreement with the numerical simulation results for 10 km asteroid impact a gabbroic anorthosite target at 20 km/sec [O'Keefe and Ahrens, 1977]. The average pressure was fitted to the same form as equation 3.15. The values of a and b for near range ($R/R_o<2.7$) and far range ($R/R_o<2.7$) are listed in Table 3.3. Figure 3.6 shows the pressure profile calculated using equation (3.15).

Estimation of Degassed Carbon and Sulfur Mass

Two scenarios have been considered in our estimation. The first scenario is that a 10 km diameter chondritic asteroid bolide indued, via impact, the Chicxulub structure. We asume an initial velocity of 20 km/sec. The diameter was estimated by maintaining the global Ir anomaly constant (~$3.7x10^{10}$ g from the Gubbio section [Alvarez et al., 1980]). The second scenario assumes the bolide was a comet ($\rho_o \approx 1$ g/cm^3, $v \approx 60$ km/sec). Several Halley flybys by the Giotto and Vega spacecraft showed [Jessberger et al., 1989] that the element composition of the comet is similar (within a factor of 2) to CI chondrites for elements heavier than O. Comets appear to be more enriched in CHON elements and, as a result, the atomic concentrations of heavy elements are about one fourth of the corresponding values for chondrites. Since the average atomic weight is also lower for the comet (~9.6 as opposed to ~14.9 for chondrites), the comet/chondrite mass abundance ratio for heavy elements is about 0.4. To maintain the global Ir anomaly constant, the hypothetical comet's diameter, by this reasoning, must be around 14 km. The pressure decay profile for the comet impact case is obtained by shifting the asteroid pressure profile such that both have the same new impact shock pressure. Thus we assume that the

Table 3.3 Parameters Used to Estimated Average Pressures of the Chicxulub Crater

	Near-field	Far-field
a	-0.608	-1.97
b	0.192	0.772

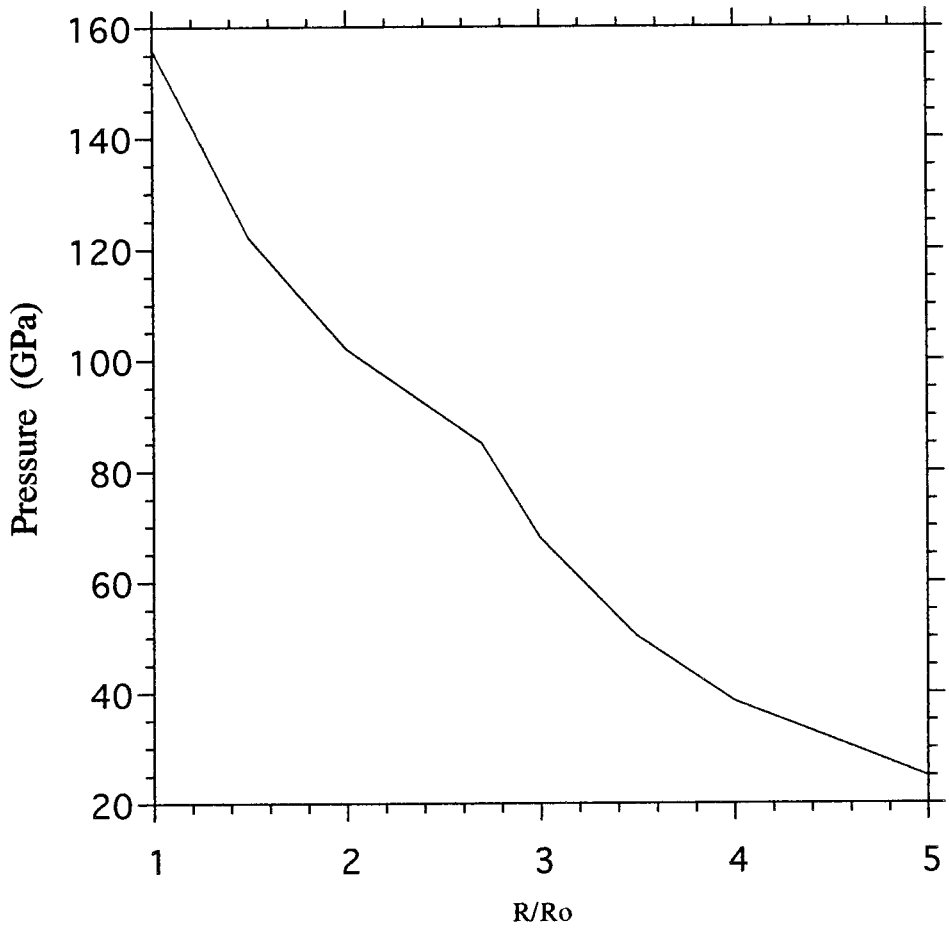

Figure 3.6 Shock pressure versus normalized radius.

peak shock pressure of ~700 GPa from a lower density comet impacting at 60 km/sec equals that induced by the impact of 2.7 g/cm^3 asteroid at 20 km/sec.

Based on geological information collected by Sharpton et al. [1993], we assume a 300 m thick 59% calcite and 50% anhydrite bed 1 km below the surface. Although the transient crater depth can be as deep as 45 to 60 km, only the top ~1 km contains carbonate and anhydrite [Sharpton et al., 1993]. The granitic basement is not involved in volatilization.Using the vaporization versus pressure curves and equation 3.15, the degassed carbon and sulfur masses were calculated and given in Table 3.4. The values for sulfur is an upper bound value since some (6.4×10^{15} gm) of S has apparently been entrained and mixed into shock-induced glass melts [Sigurdsson, 1992] and never was introduced into the atmosphere. The mass of carbon (CO_2), however, is a lower bound since the shear band heating effect may have caused degassing at less than the calculated value, 54±6 GPa, for crystal calcite [Lange and Ahrens, 1986]. Figure 3.7A shows the geological structure used in our calculation, Figure 3.7B shows the asteroid impact scenario, in which the incipient vaporization diameters for anhydrite and calcite are 10 and 20 km, and complete vaporization diameters are 29 and 34 km, respectively. Figure 3.7C shows the comet impact scenario, in which the incipient vaporization diameters for anhydrite and calcite are 51 and 61 km, and complete vaporization diameters are 67 and 86 km, respectively.

3.4 Global Effects

The theory of lofting large amount of impact-induced CO_2, SO_2 or SO_3 into the stratosphere and the resulting temperature increase (CO_2) or decrease (SO_2 and SO_3) is largely based on numerical simulation and extrapolation of volcanic eruption data. Due to the complexity of the global climate modeling, in general, the results from these simulations and extrapolations should be considered with great caution. The relation of

Table 3.4 Degassed Carbon and Sulfur Mass from the Chicxulub Impact

	Carbon ($x10^{16}$ g)			Sulfur ($x10^{16}$ g)		
Scenarios	Complete vapor region	Partial vapor region	Total	Complete vapor region	Partial vapor region	Total
Asteroid scenario	1.51	1.52	3.3	0.79	3.60	4.39* (23)†
Comet scenario	14.2	5.98	20.2	21.4	14.3	35.7* (770)†

† The values are estimated by Pope et al. [1994]. * Less the $0.64x10^{16}$ g discovered in impact melt.

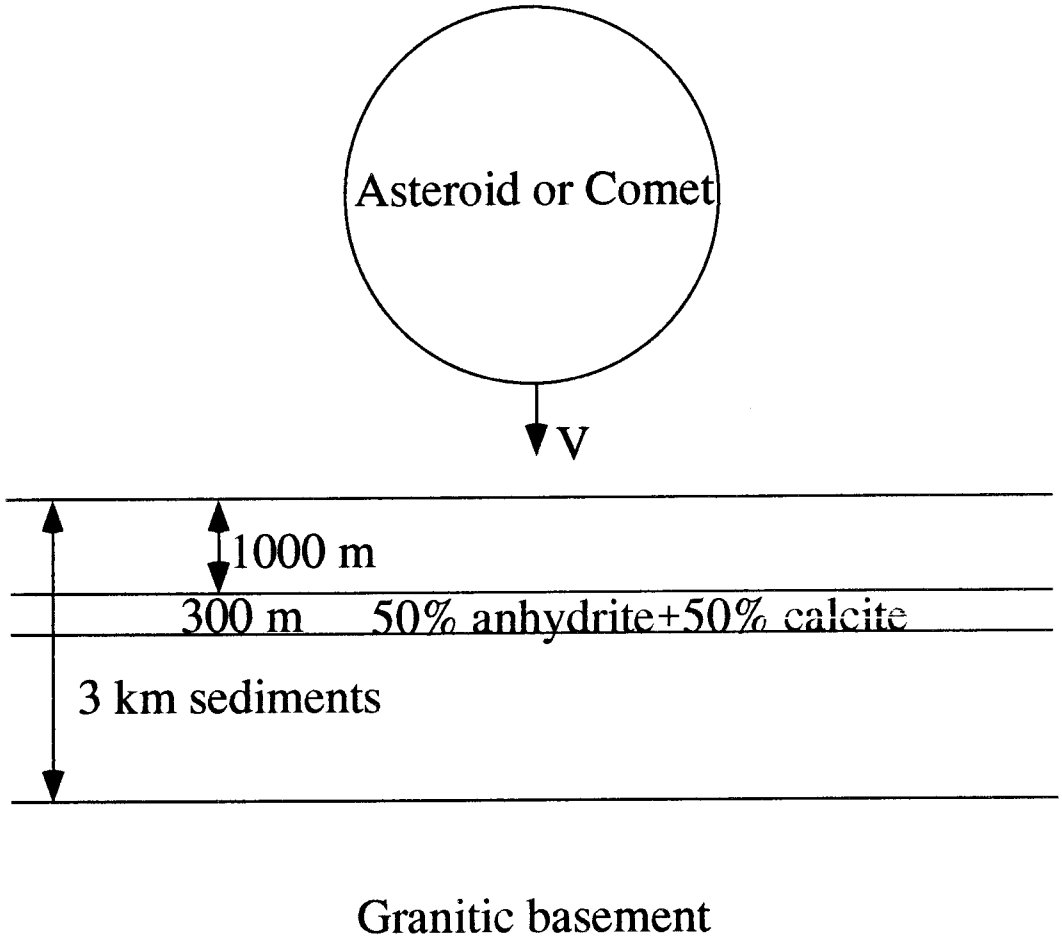

Figure 3.7A Geological structure used in calculation.

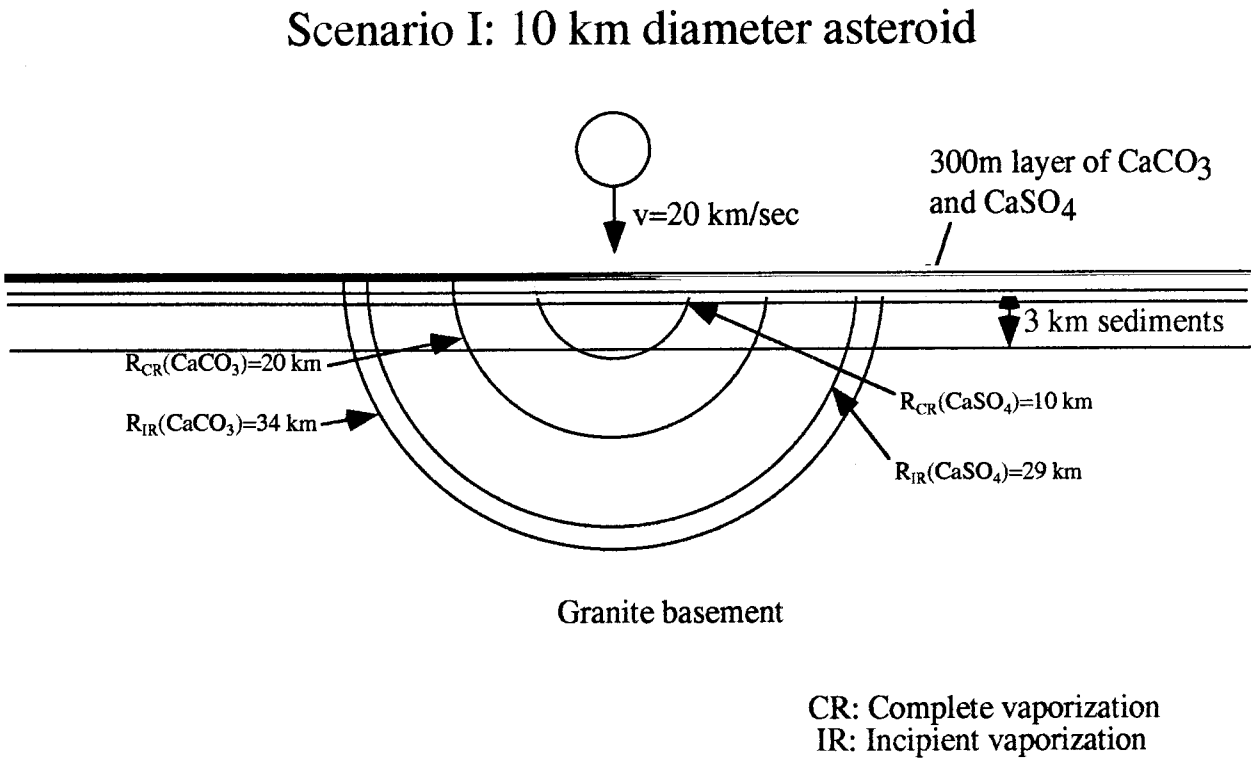

Figure 3.7B Scenario I, the10 km diameter, 20 km/sec speed asteroid impact.

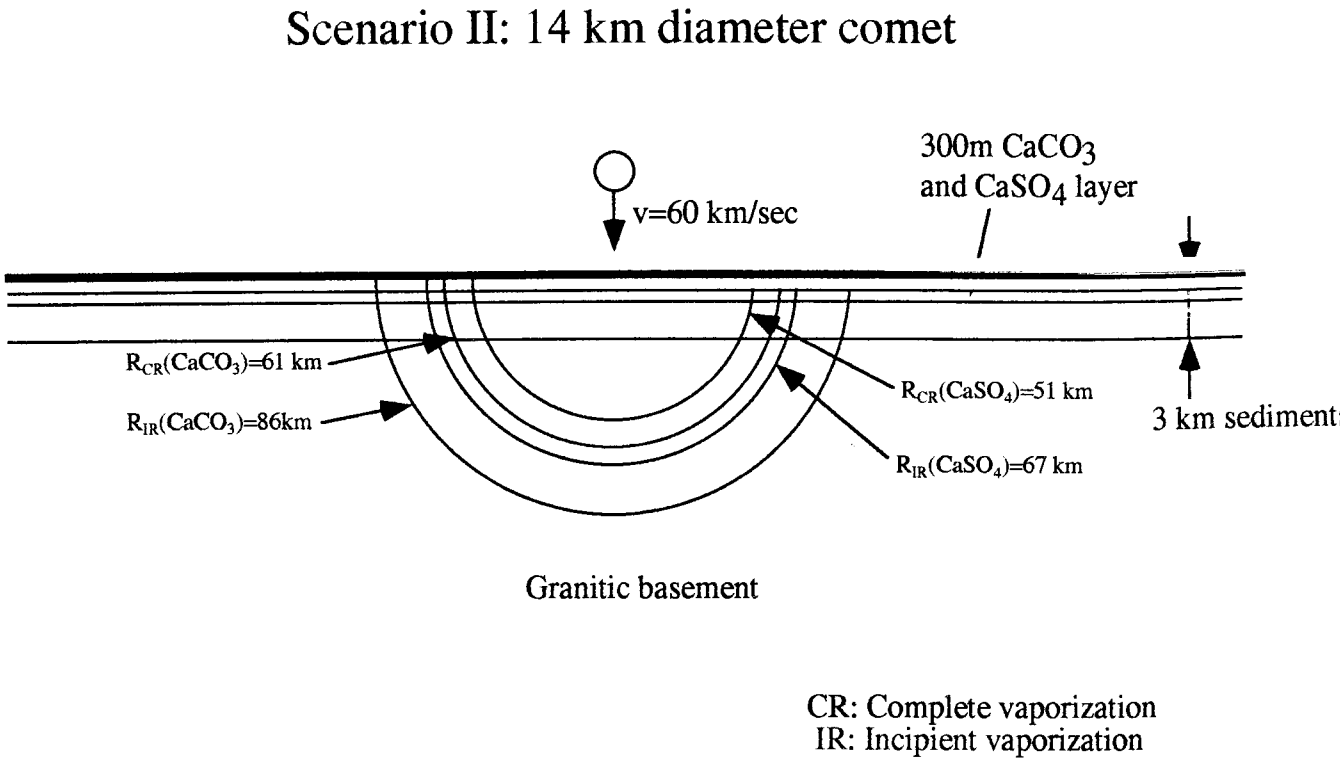

Figure 3.7C Scenario II, the 14 km diameter, 60 km/sec speed comet impact.

temperature increase due to CO_2's increase in the atmosphere given by [O'Keefe and Ahrens, 1989]:

$$\Delta T = 10[\log_{10}(1+\frac{\Delta m}{m_o})] \qquad (3.16)$$

where m_o=2.7x10^{18} g is the CO_2 mass in the normal atmosphere [Kasting and Ackerman, 1986], Δm is the CO_2 mass increase due to impact degassing. Using this relation and the degassed carbon (as CO_2) mass from the Chicxulub impact, a global warming of 0.2°C for the asteroid scenario and 1.1°C for the comet scenario would occur after the Chicxulub impact. This estimate is less than the 2-10°C suggested by O'Keefe and Ahrens [1989] since they used a much lower value (~10 GPa) of the shock pressure required for the onset of vaporization which from the present work which is 54±6 GPa.

Measurements of the $^{13}C/^{12}C$ ratio of the planktonic foraminifera after the K/T event demonstrated that ^{13}C was depleted for 10^4-10^5 years [Hsü and McKenzie, 1985] which is consistent with the time scale of mass extinction suggested by Hut et al. [1987]. This suggests a long term CO_2-enrichment of the atmosphere, in other words, a long term global warming after the K/T impact.

For sulfur, Sigurdsson [1990a] used the following empirical relation to correlate the volcanic sulfur mass yield, X, in grams, to observed temperature decreases after the eruptions:

$$\Delta T = 5.9 \times 10^{-5} X^{0.31} \qquad (3.17)$$

This formula gives a global cooling of 8.5 and 16°C for the asteroid and comet scenario, respectively. These average temperature decreases would have severely stressed the biotic environment. However, the largest historic volcanic eruption (Tambora, 1815, caused cooling of 0.7°C in the following two years [Sigurdsson, 1990b; Pinto et al., 1989]) degassed only 1-2x10^{14} gm SO_2, which is about three orders of magnitude smaller than our estimated values. Extrapolation of this relationship is probably not reliable.

Pope et al. [1994], using a one-dimensional radiative transfer model [Baines and Smith, 1990], studied the global cooling effects of the sulfuric acid aerosols produced by

impact released SO_2 or SO_3, and suggested that photosynthesis was halted by a drastic decrease in solar insulation in plants for 6-9 months after the Chicxulub impact and at least decades of global freezing followed the impact event. Sigurdsson et al. [1992] also favors a severe global cooling scenario. The amount of degassed sulfur mass in both previous studies were over-estimated due to the use of lower incipient and complete reaction pressure values (30 and 100 GPa [Pope et al., 1994], 40 GPa [Sigurdsson et al., 1992]).

There is actually little physical evidence supporting a severe global cooling event after the K/T impact. For example, $\delta^{18}O$ studies [briefly summarized in Sigurdsson et al., 1992] across the K/T boundary indicate no clear-cut trend of temperature anomaly. Taking into account of the self-limiting effects of sulfuric aerosol [Pinto et al., 1989], the impact-induced severe cooling event may be too short to be well recorded in the sedimentary record, as Sigurdsson et al. [1992] suggested.

Based upon our experiments, calculation and discussions above, we conclude that the impact-induced-sulfur-formed H_2SO_4, like the dust cloud originally proposed by Alvarez et al. [1980], may played a shorter and less important role in cooling the Earth for a short period during the 10^4-10^5 years [Hut et al., 1987] mass extinction period. Our present results which yield higher shock pressure required to shock volatize $CaSO_4$ tend to favor a short-term cooling event followed by long-term global warming event induced by CO_2. It is still unclear which of any of the major extinction mechanisms proposed dominated and produced the mass extinction at the K/T boundary.

3.5 Summary

Incipient and complete reaction criteria for shock vaporization of calcite and anhydrite have been determined using recent experimental results and revised thermodynamic calculational methods [Chapter 1 and 2]. For calcite, the shock pressures for incipient and

complete vaporization are 54±6 and 103±12 GPa, respectively. The complete vaporization pressure agrees with previous estimates from solid recovery experiments [Lange and Ahrens, 1986]. However, the incipient vaporization pressure is much higher than the solid recovery experimental value (~10 GPa [Lange and Ahrens, 1986]) probably due to shear band heating effect which accurs in single crystals of calcite [Grady, 1977; Kondo and Ahrens, 1983]. In the case of anhydrite, incipient and complete vaporization shock pressures are 81.0±6.5 and 155±13 GPa, respectively.

The amount of degassed carbon and sulfur have been estimated for the Chicxulub impact and their effects on the global temperature have been calculated and discussed. The calculated global warming induced by the degassed CO_2 is 0.2-1.1°C and the global cooling resulting from a decrease in solar insolation introduced by the degassed SO_2 (forming stratospheric aerosols of H_2SO_4) is 8.5-16°C for the Chicxulub impact. We conclude that impact-induced sulfuric acid aerosols may caused severe environmental stress by reducing solar radiation for several months as suggested by Pope et al. [1994]. The impact-induced CO_2, on the other hand, may cause a long-term (>10^3 years) global warming of ~1°C. Although evidence in the $\delta^{13}C$ geologic record exists for a global heating event, the ~1°C magnitude we calculate appears unlikely to have produced mass extinctions. We therefore, in agreement with Pope et al. [1994], infer that the most likely cause of the K/T extinction is global cooling, possibly induced by H_2SO_4 aerosol or by impact induced-dust, as first proposed by Alvarez et al. [1980]. However, the lack of a clear-cut geochemical signature in the stratigraphic record makes those conclusions highly tentative.

Chapter 4

A Six Channel High-Sensitivity, Time-Resolving Pyrometer for Shock Temperature Measurements

4.1 Introduction

Time-resolved pyrometry has been widely used in the fields of condensed matter physics, chemistry, high explosives and high-pressure geophysics. Boslough and Ahrens [1989] reviewed the applications of pyrometry to study shocked materials.

In the field of high-pressure geophysics, there have been great interest in measuring the temperatures of Fe, Fe compounds and alloys, Earth mantle minerals under shock pressures up to ~300 GPa [Williams et al., 1987; Yoo et al., 1993; Ahrens et al., 1990]. Recently, thermal conductivities of LiF and Al_2O_3 under high pressure have been measured in order to obtain more accurate shock temperature measurements for metals [e.g. Gallagher and Ahrens, 1995]. Shock temperature measurements place constraints on high-pressure equation-of-states, permit detection and quantification of phase transformations. These also provide data needed to describe both evolution of heat from the core as well as constrain mantle convection modeling [e.g. Tackley et al., 1994].

The light detectors that are used for time-resolved pyrometers employ either photomultipliers [e.g. Radousky and Mitchell, 1989] or photodiodes [e.g. Boslough, 1984]. Photomultiplier tubes have relatively fast response-times (1-3 ns) but their

sensitivity is usually limited to the UV/visible range. Moreover, they require high-voltage power supplies (> 1200 volt). Photodiodes, on the other hand, are sensitive in the near-infrared and require only 15 volt DC power supplies. When attached to amplifier systems, they have slower rise-times (~10 ns). The use of beam splitters in previous pyrometers makes the alignment of these systems cumbersome. A recent fiber-coupled design by Holmes [1995] has eliminated the beam splitters and greatly simplified calibration methods. However, this design does not average different regions of the shocked sample, and hence is more sensitive to the usual sample flaws in naturally occurring minerals.

In this work, an existing six-channel pyrometer [Miller and Ahrens., 1989] is modified using high sensitivity, fast-response photodiodes and an improved light transmitting system. The design aims to allow time-dependent shock-induced signals in minerals (~1000 ns) to be measured with rise-time of <3 ns as well as permits relatively low temperatures (~2000 K) to be measured.

As an example of the application of this new pyrometer, experiments were conducted on the Caltech 25 mm light-gas gun [Jeanloz and Ahrens, 1977]. The thermal diffusivities of lithium fluoride (LiF) at 165 and 266 GPa and aluminum oxide (Al_2O_3) at 242 GPa relative to iron also shocked to these pressures were measured.

4.2 System Layout and Discussions

The description of the optical system (Figure 4.1) is given following the light path emitted from the target. In the case of the relative thermal diffusivity measurements, the target (Fig. 4.1b and Fig. 4.2a) is a sandwich in which a thin metal film (~500 Å) is embedded between two transparent window plates (2-7 mm LiF or Al_2O_3). During shock loading, light emitted from the metal-window interface is collected and recorded by the system. An edge mask (typically with a hole diameter of 2 to 5 mm) is placed in front of the window to allow only optical radiation of material subject to one-dimensional

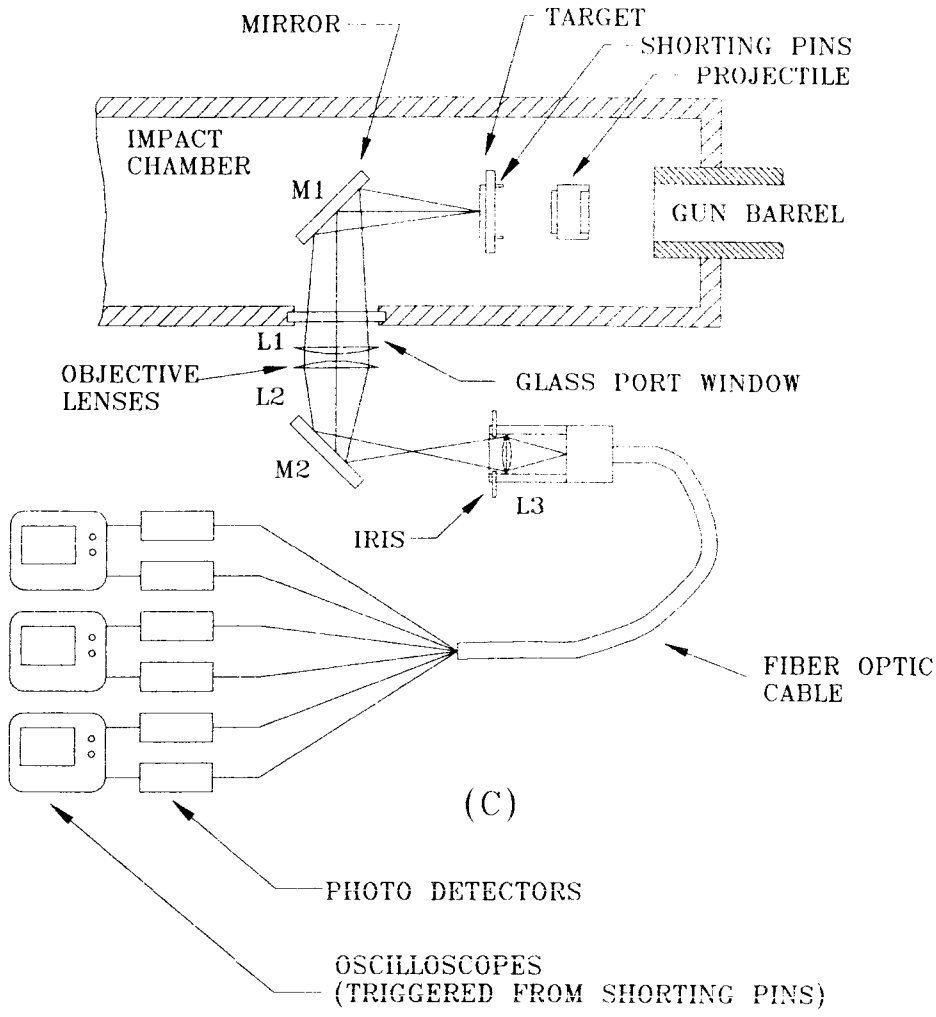

Figure 4.1 Schematic drawing of the pyrometer system. (C) The whole system layout.

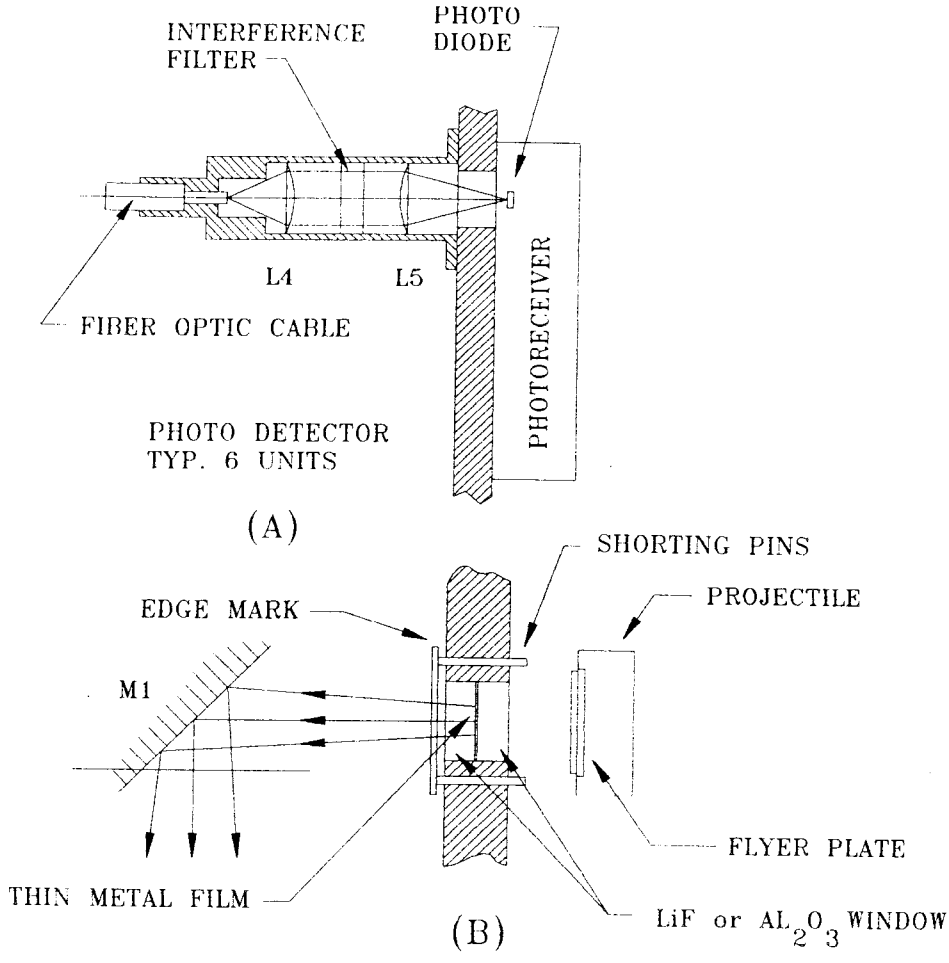

Figure 4.1 Schematic drawing of the pyrometer system. (A) The probe which collimates and focuses light onto the sensitive element of the photoreceiver; (B) The target assembly.

compression to be viewed. Mirror M1 turns the light 90^{o} into a port window. A expendable Pyrex glass plate (10 mm thick) is used as a fragment shield. L1 and L2 are two crown glass plano-convex lenses with focal lengths of 50 cm and clear aperture of 11.4 cm. The target is at the focal point of the L1. L2 focuses the light onto a field lens, L3, which is at the focal point of L2. L3 is a crown glass bi-convex lens with a focal length 5 cm and a clear aperture of 2.5 cm. L3 images L2 onto the common end of a multi-leg fused silica fiber bundle (Oriel Corp., customer design). The introduction of lens, L3, insures that a ray from every point of the target will completely fill the end of the fiber bundle [Wyatt, 1983]. Thus all fibers collect light from the whole target area defined by the edge mask. Therefore, possible inhomogeneities [Kondo and Ahrens, 1983] in the sample area are averaged, and the possibility that different fibers, and thus different channels, may receive radiation from different regions of the sample is eliminated. In addition, the 100 μm fibers are randomly packed inside the bundle, this further minimizes any possible sampling biases for six channels. The common end of the fiber bundle has a core of 5 mm diameter (20 cm long) and its six branches (10 cm long) each have a 2 mm diameter core. They are sheathed with stainless steel monocoil for protection and flexibility. An iris is used in front of L3 to accommodate different sample sizes and eliminates light from sources other than the sample. Each leg is then connected to a probe (Figure 4.1c) which collimates the collected light, which passes through a band-pass interference filter (~30 nm width) and then focuses it onto the photodiode of the photoreceiver. Lenses L4 and L5, which collimate and focus the light, are crown glass plano-convex with 19 mm focal length and 11 mm diameter of clear aperture. The photoreceiver (New Focus, Inc., Model 1801) used consists of a silicon PIN diode with a sensitive area of 0.85 mm^2, a transimpedance built-in amplifier with a conversion gain of 24 mv/μW at 850 nm wavelength. It has a bandwidth of DC-125 MHz and a rise time of 3 ns. The photoreceivers are powered by +/-15 Volt DC power supplies (New Focus, Inc., Model 0901). The output signals from the photoreceivers are recorded by an array of DC-

500 MHz digitizers (HP 54111). Taking the digitizers' rise time (~0.7 ns) into account, the rise time of the whole system is about 3 ns. All the components of the system, except the objective lenses L1 and L2, the power supplies and the digitizers, are mounted on a steel rack and physically occupies 30cmx60cmx90cm.

Calibration is conducted before every shot. A 200 Watt tungsten coil filament quartz-halogen lamp (General Electric type Q6.6A/T4Q/5CL 200 Watt, calibrated by Optronics Laboratories, Inc.) or a 1000 Watt lamp (also calibrated by Optronics Laboratory, Inc.) are used, depending on how much light is expected during the experiment, to achieve improved signal to noise ratios. Before a shot, the lamp is placed within ±0.5 mm of the sample position and the calibration is then conducted using a DC power supply which supplies lamp current within ±0.1 Amp. at 64 V-DC as required by calibration procedures. After the calibration, the lamp is replaced by the sample. Other components are not altered before the experiment is conducted. Detailed descriptions of calibration procedures and discussions of the error analysis of the effective wavelength of all the optical components can be found in [Boslough and Ahrens, 1989] and the references therein. Here we concentrate our discussion of experimental parameters which affects quality of experimental results.

Since the radiation energy, E, received by lens L1 is proportional to the square of the diameter, d_m, of the edge mask, i. e.:

$$E \propto d_m^2 \qquad (4.1)$$

the diameter of the edge mask used is a critical parameter. The diameter we previously employed was usually 5-10 mm. Due to the higher gain of the new photoreceivers (~20 times of previous pyrometer), the diameter of the edge mask now can be as small as 1.5 mm. This allows measurement of 5 mm diameter mineral samples.

A neutral density filter needs to be placed in front of the iris (Figure 4.1a) during calibration and for experiments for which the light emission is expected to saturate the photoreceivers. In this case, the 1000 Watt lamp is used in calibration since it emits five

times more light than the 200 Watt lamp and consequently it gives a better signal to noise ratio for the calibration. The saturation energy of the photo-receivers is a function of wavelength (e.g., 75 μW @ 850 nm). Thus in experiments some channels will saturate while we try to obtain the highest signal-to-noise ratio for the channels which output smaller signal levels. Therefore, the probes (Figure 4.1a) are moved to defocus the beams so that the photodiode will receive less light and not be saturated. The specific density of the filter is determined by estimating the amount of radiation energy the photoreceiver will receive during a shot. Another way to avoid saturation is to use interference filters with narrower band-pass for channels receiving more radiation energy and wider bandpass for channels receiving less radiation energy. Table 4.1 shows the (typical) calibration results for shot 285.

4.3 Thermal Conductivity Measurements of LiF and Al_2O_3 under High Pressure

Shock temperature measurement of metals are usually conducted by measuring the radiation emitted from a metal-window interface (usually LiF, Al_2O_3 or diamond [Bass et al., 1987; Yoo et al., 1993]). Because the knowledge of the thermal diffusivities of the window materials are needed in order to calculate the Hugoniot temperature of the metal, experimental determination of thermal conductivities of dielectrics such as LiF and Al_2O_3 is very important since there is no experimental constraints on the theoretically calculated values under high pressure and temperature [Roufosse and Jeanloz, 1983; Tang, 1994]

Three shots has been conducted with pressures from 165-266 GPa. In these experiments, thin metal films (~500 Å) were sandwiched by LiF or Al_2O_3 windows, the time-resolved radiation from the metal-window interface were collected by the six channel pyrometer after the shock wave propagated through the metal film. Each series of

Table 4.1 Calibration results for shot 285

Channel	1	2	3	4	5	6
Wavelength (nm)	451.5±0.05	555.5±0.05	603.7±0.05	661.5±0.05	748.2±0.05	904.0±0.05
Light intensity $(\frac{\mu W}{cm^2 \cdot nm})$	0.4409	0.6966	0.7714	0.8244	0.8389	0.7583
Output signal (mv)	169.0±6	413.9±6	307.2±6	166.7±6	354.3±6	63.0±6
Calibration value $(\frac{10^{-3}\mu W}{cm^2 \cdot nm \cdot mv})$	2.609±0.093	1.683±0.024	2.511±0.049	4.945±0.178	2.368±0.040	12.04±1.15

radiation versus time data were then multiplied by the calibration factors (e.g., Table 4.1) obtained from the calibration using the standard tungsten lamp before further analysis. The interface temperature at a specific time was then obtained by fitting the six channel data to a gray-body Planck spectrum:

$$I = \frac{c_1 \varepsilon \lambda^5}{\exp(\frac{c_2}{\lambda T}) - 1} \qquad (4.2)$$

where I is radiance, ε is emissivity, λ is wavelength, T is temperature, c_1 and c_2 are constants with values 1.191×10^{-6} Wm^2/ster and 1.438×10^{-2} mK, respectively. Figure 4.2a shows a typical geometry of an experiment used to determine the thermal diffusivity of the window material (relative to the assumed known property of iron film).

To analyze the radiance versus time data, such as shown in Fig. 4.2b, finite-difference calculation was performed using the ' Conman ' program [King et al., 1991]. We solve the coupled thermal conduction equations for the spatial and temporal temperature distribution within window and the film. The ratio of the thermal diffusivities of the metal (κ_1) and window (κ_2), R, has been varied. The best fit R matches the experimentally obtained time-dependent temperature profile. We assume the thermal conductivity of metal ($k_1 = \rho_1 c_{1p} \kappa_1$, where ρ_1 and c_{1p} are density and specific heat of the shock state) in the metal can be calculated accurately using previously obtained electrical conductivity data versus shock pressure for iron via the Weidemann-Franz law. Separate measured parameters including equations of state of the metal and window materials, thermal conductivities of the window materials ($k_2 = \rho_2 c_{2p} \kappa_2$) can be calculated. For shot 286 (Figure 4.2b), the best fit is given by R ~100. Table 4.2 lists the resulting high pressure thermal conductivity values for Al_2O_3 and LiF. The measured values are 2-3 orders of magnitude less than theoretically predicted. Note that the larger the value of R, the closer the interface temperature is to the interior of the film. Thus we conclude that temperatures in metals obtained from previous shock experiments using windows may have been overestimated since much higher thermal conductivities were used for window

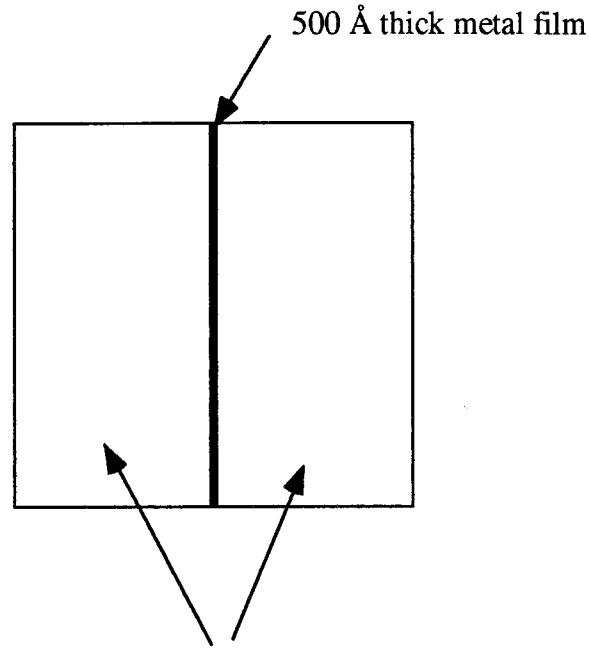

Figure 4.2a Diagram of experimental assembly showing the metal film sandwiched by the single crystal Al_2O_3 or LiF windows.

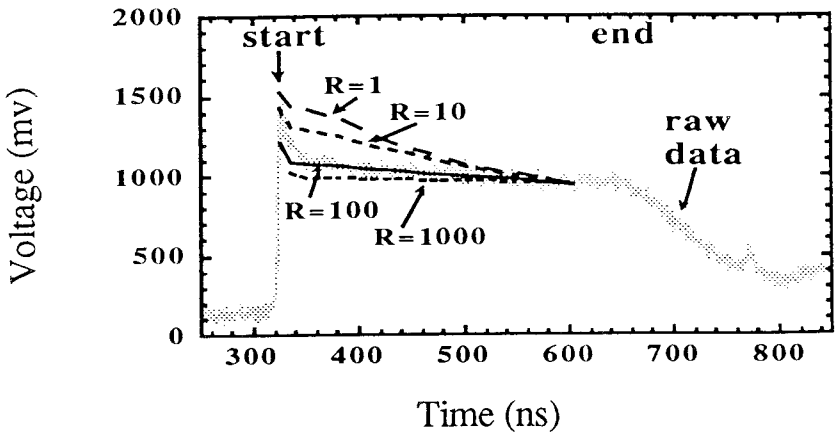

Figure 4.2b Comparison of raw data for shot 286 (channel 3 @603.7 nm) and theoretical models for various R, the ratio of thermal diffusivities of the Fe film and the LiF window at shock pressure of 266 GPa and 2100 K.

Table 4.2 Experimental High Temperature and Pressure Thermal Conductivities of LiF and Al_2O_3

Shot No.	Material	P_h (GPa)	T_h (K)	$k_{t,p}$ (W/mK)
285	Al_2O_3	242	2753	~0.02
286	LiF	266	2100	0.02
287	LiF	165	2087	0.01-0.02

P_h is Hugoniot pressure, T_h is Hugoniot temperature, $k_{t,p}$ is measured thermal conductivity at P_h and T_h .

media in correcting interface temperature to obtain too high a Hugoniot temperature [Williams et al., 1987; Bass et al., 1987].

4.4 Summary

A high-sensitivity (24 mv/μW @850nm), time-resolved six-channel pyrometer has been designed and constructed and used in shock temperature measurements. Due to the high gain of the system, small mineral samples (~5 mm in diameter) can be used in shock temperature experiments. The employment of a field lens in the light path of the system and the random packing of the glass fiber bundle insures that the radiative temperature measured is an average over the whole viewed area of the sample and thus is insensitive to flaws in minerals. Thermal conductivities of LiF and Al_2O_3 were measured, for the first time, using this new system. Their values are 2-3 orders of magnitude less than theoretical values which were previously used for making window corrections in shock temperature measurements for Fe [Bass et al., 1987]. The new thermal conductivity caused corrections for the Fe melting point may have significant implications on temperature and transfer of heat within the Earth's interior.

Bibliography

Adadurov, G. A., D. B. Balashov, and A. N. Dremin, A study of the volumetric compressibility of marble at high pressures, *Bull. Acad. Sci. USSR Geophys. Ser.*, 5, 463-466, 1961.

Ahrens, T. J., and V. G. Gregson, Jr., Shock compression of crustal rocks: Data for quartz, calcite, and plagiclase rocks, *J. Geophys. Res.*, 69, 4839-4874, 1964.

Ahrens, T. J., J. T. Rosenberg, and M. V. Ruderman, Dynamic properties of rocks, *Rep. DASA* 1868, 107-111, Stanford Res. Inst., Menlo Park, Calif., 1966.

Ahrens, T. J., D. L. Anderson, and A. E. Ringwood, Equations of state and crystal structures of high-pressure phases of shocked silicates and oxides, *Rev. Geophys. Space Phys.*, 7, 667-707, 1969a.

Ahrens, T. J., C. F. Petersen, and J. T. Rosenberg, Shock compression of feldspars, *J. Geophys. Res.*, 74, 2727-2746, 1969b.

Ahrens, T. J., J. H. Lower, and P. L. Lagus, Equation of forsterite, *J. Geophys. Res.*, 76, 514-528, 1971.

Ahrens, T. J., Shock melting and vaporization of metals, *J. Appl. Phys.*, 43, 2443-2445, 1972.

Ahrens, T. J., and J. D. O'Keefe, Shock melting and vaporization of lunar rocks and minerals, *The Moon*, 4, 214-249, 1972.

Ahrens, T. J., and J. D. O'Keefe, Equation of state and impact-induced shock-wave attenuation on the moon, in: *Impact and Explosion Cratering*, D. J. Roddy, R. O. Pepin, R. B. Merrill, eds., pp. 639-656, Pergamon, New York, 1977.

Ahrens, T. J., Shock wave techniques for geophysics and planetary physics, in *Methods of Experimental Physics*, Vol. 24, C. G. Sammis and T. L. Henyey eds., pp. 185-235, Academic, San Diego, Calif., 1987.

Ahrens, T. J., J. D. Bass, and J. R. Abelson, in: *Proceedings of Shock Compression of Condensed Matter*-1989, edited by S. C. Schmidt, J. N. Johnson, L. W. Davison, Elsevier Science Publishers, B. V., pp 851-857, 1990.

Ahrens, T. J., W. W. Anderson, and Y. Zhao, Shock propagation in crustal rock, *Report for Air Force Office of Scientific Research,* contract No. F49620-92-J-0402 (CIT 64649), 1995.

Alvarez, L. W., W. Alvarez, F. Asaro, and H. V. Michel, Extraterrestrial cause for the Cretaceous/Tertiary extinction, *Science*, 208, 1095-1108, 1980.

Alvarez, W., P. Claeys, and S. W. Kieffer, Emplacement of Cretaceous-Tertiary boundary shocked quartz from Chicxulub crater, *Science,* 269, 930-935, 1995.

Baines, K. H., and W. H. Smith, The atmospheric structure and dynamical properties of Neptune derived from ground-based and IUE spectrophotometry, *Icarus* 85, 65-108, 1990.

Barker, L. M., and R. E. Hollenbach, Shock-wave studies of PMMA, fused silica, and sapphire, *J. Appl. Phys.*, 41, 4208-4226, 1970.

Barker, L. M., and R. E. Hollenbach, Laser interferometer for measuring high velocities of any reflecting surface, *J. Appl. Phys.*, 43, 4669-4675, 1972.

Barker, L. M., and R. E. Schuler, Correction to the velocity-per-fringe relationship for the VISAR interferometer, *J. Appl. Phys.*, 45, 3692-3693, 1974.

Barker, L. M., VISAR88 - a new data reduction program for VISARs, *Sandia Natl. Lab., Rep. SAND88-2788,* Albuquerque, NM, 1988.

Barker, L. M., The Valyn VISAR, Valyn International, Albuquerque, New Mexico, 1994.

Bass, J. D., B. Svendsen, and T. J. Ahrens, The temperature of shock compressed iron, in *High-Pressure Research in Mineral Physics*, edited by M. H. Manghnani and Y. Syono, American Geophysical Union, Washington, D. C., pp. 393-402, 1987.

Blum, J. D. and C. P. Chamberlain, Oxygen isotope constraints on the origin of impact glasses from the Cretaceous-Tertiary Boundary, *Science*, 257, 1104-1107, 1992.

Bohor, B. F., E. E. Foord, P. J. Modreski, and D. M. Triplehorn, Mineralogical Evidence for an Impact Event at the Cretaceous-Tertiary Boundary, *Science*, 224, 867-869, 1984.

Boslough, M. B., Shock-wave properties and high-pressure equations-of-state of geophysically-important materials, *Ph D thesis*, California Institute of Technology, Pasadena, California, 1984.

Boslough, M. B., and T. J. Ahrens, A sensitive time-resolved radiation pyrometer for shock-temperature measurements above 1500-K, *Rev. Sci. Instum.*, 60, 3711-3716, 1989.

Brett, R., The Cretaceous-Tertiary Extinction: A lethal mechanism involving anhydrite target rocks, *Geochim. et Cosmochim. Acta* , 56, 3603-3606, 1992.

Bridgman, P. W., The linear compressibility of thirteen natural crystals. *American Journal of Science,* 15, 287-296, 1925.

Bridgman, P. W., The high pressure behaviour of miscellaneous minerals, *American Journal of Science,* 237, 7-18, 1939.

Chen, G., J. A. Tyburczy, and T. J. Ahrens, Shock-induced devolatilization of calcium sulfate and implication for K-T extinctions, *Earth Planet. Sci. Lett.*, 128, 615-628, 1994.

Crutzen, P. J., Acid rain at the K/T boundary, *Nature*, 330, 108-109, 1987.

Dandekar, D. P., Pressure dependence of the elastic constants of calcite. *Physical Review,* 172, 873, 1968.

Duffy T. S., Elastic Properties of Metals and Minerals Under Shock Compression, *Ph. D. thesis*, California Institute of Technology, Pasadena, California, 1992.

Emiliani C., E. B. Kraus, and E. M. Shoemaker, Sudden death at the Mesozoic, *Earth Planet. Sci. Lett.*, *55*, 317-334, 1981.

Fiquet, G., F. Guyot, and J. P. Itié, High-pressure X-ray diffracton study of carbonates: $MgCO_3$, $CaMg(CO_3)_2$, and $CaCO_3$, *American Mineralogist, Vol. 79,* 15-23, 1994.

Gallagher, K G., and T. J. Ahrens, Ultra high pressure thermal conductivity measurements of griceite and corundum, in Proceedings of the 20th ISSW, 1995 (in press)

Gerasimov, M. V., Y. P. Dikov, O. I. Yakovlev, and F. Wlotzka, High-temperature vaporization of gypsum and anhydrite: Experimental results. *LPSC XXV*, 413-414, Lunar and Planetary Institute, Houston, Texas, 1994.

Grady D. E., W. I. Murri, and G. R. Fowles, Quartz to stishovite: Wave propagation in the mixed phase region, *J. Geophys. Res.*, 79, 332-338, 1974.

Grady D. E., Processes occurring in shock compression of rocks and minerals, in: *High Pressure Research: Applications to Geophysics,* M. H. Manghnani and S. Akimoto, eds., pp. 389-438, Academic Press, New York, N. Y., 1977.

Grady, D. E., R. E. Hollenbach, K. W. Schuler, Compression wave studies on calcite rock, *J. Geophys. Res.*, 83, 2839-2849, 1978.

Grady, D. E., Compression wave studies in Oakhall Limestone, *Rep. SAND85-0947, Sandia Natl. Lab.*, Albuquerque, N. M., 1983.

Grieve, R. A. F., and P.J. Robertson, The terrestrial cratering record, 1, current status of observations, *Icarus,* 83, 212-229, 1979.

Hemsing, W. F., Velocity sensing interferometer (VISAR) modification, *Rev. Sci. Instum.*, 50, 73-78, 1979.

Hemsing, W. F., VISAR: 2 1/2 minutes for data reduction, in *High Speed Photography, Videography, and Photonics, Proc. SPIE,* 427, 199-202, 1983.

Hildebrand, A. R., G. T. Penfield, D. A. Kring, M. Pilkington, A. Camargo Z., S. B. Jacobsen, and W. V. Boynton, Chicxulub Crater: A possible Cretaceous/Tertiary boundary impact crater on the Yucatán Peninsula, Mexico, *Geology,* 19, 867-871,

1991.

Holsapple, K. A., The scaling of impact processes in planetary sciences, *Ann. Rev. Earth Planet. Sci.*, 21, 333-373, 1993.

Holmes, N. C., Fiber-coupled optical pyrometer for shock-wave studies, *Rev. Sci. Instrum,*. 66, 2615-2618, 1995.

Hsü, K. J., and J. A. McKenzie, The carbon cycle and atmospheric CO_2: Natural variations, *Geophys. Monogr.*, 32, Am. Geophys. Un., Washington DC, pp. 627, 1985.

Huang, W. L., and P. J. Wyllie, Melting relationship in the system CaO-CO_2 and MgO-CO_2 to 33 kilobars, *Geochim. Cosmochim. Acta,* 40, 129-132, 1976.

Hut, P., W. Alvarez, W. P. Elder, T. Hansen, E. G. Kauffman, G. Keller, E. M. Shoemaker, and P. R. Weissman, Comet showers as a cause of mass extinctions, *Nature* , 329, 118-126,1987.

Irving, A. J., and P. J. Wyllie, Subsolidus and melting relationships for calcite, magnesite, and the join $CaCO_3$-$MgCO_3$ to 36kbar, *Geochim. Cosmochim. Acta,* 39, 35-53, 1975.

Izett, G. A., W. A. Cobban, J. S. Obradovich, and M. J. Kunk, The Manson Impact Structure: $^{40}Ar/^{39}Ar$ age and its distal impact ejecta in the Pierre shale in southeastern South Dakota, *Science*, 262, 729-732, 1993.

Jeanloz, R., and T. J. Ahrens, Pyroxenes olivines: structure implications of shock-wave data for high pressure phases, *High-Pressure Research in Mineral Physics*, M. H. Manghnani and Akimoto eds., Academic, New York, p. 439, 1977.

Jamieson, J. C., Introductory studies of high-pressure polymorphism to 24,000 bars by X-ray diffraction with some comments on calcite II, *J. Geol.*, 65, 334-343, 1957.

Jessberger, E. K., J. Kissel, and J. Rahe, The composition of comets, in: *Origin and evolution of planetary and satellite atmospheres*, S. K. Atreya, J. B. Pollack, M. S. Matthews, eds., Univ. Arizona Press, Tucson, 1989.

Johannes, W., and D. Puhan, The calcite-aragonite transition, reinvestigated, *Contrib. Mineral. Petrol. 31*, 28-38, 1971.

Kalashnikov, N. G., M. N. Pavlovskiy, G. V. Simakov, and R. F. Trunin, Dynamic compressibility of calcite-group minerals, *Physics of the Solid Earth,* 2, pp. 80-84, Academy of Science of the USSR, 1973.

Kasting, J. F., and T. P. Ackerman, Climatic consequences of very high carbon dioxide levels in the Earth's early atmosphere, *Science* , 234, 1383-1385, 1986.

Kerley, G. I., Equation of state for calcite minerals. I. Theoretical model for dry calcium carbonate, *High Pressure Research,* 2, 29-47,1989.

Kieffer, S. W., and C. H. Simonds, The role of volatiles and lithology in the impact cratering process, *Rev. Geophys. Space Sci.,* 18, 143-181, 1980.

King S. D., A. Raefsky, and B. H. Hager, ConMan: Vectorizing a finite element code for incompressible two-dimensional convection in the Earth's mantle, *Phys. Earth Plan. Int.,* 59, 195-207, 1989.

Kipp, M. E., and R. J. Lawrence, WONDY V - A one-dimensional finite-difference wave propagation code, *Sandia Natl. Lab., Rep. SAND81-0930,* Albuquerque, NM, 1982.

Koeberl, C., Chicxulub crater, Yucatan-tektites, impact glasses, and the geochemistry of target rocks and breccias, *Geology* , 21, 211-214, 1993.

Kondo, K., and T. J. Ahrens, Heterogeneous shock-induced thermal radiation in minerals, *Phys. Chem. Miner.,* 9, 173-181, 1983.

Lange, M. A., and T. J. Ahrens, Shock-induced CO_2 loss from $CaCO_3$; implications for early planetary atmospheres, *Earth Planet. Sci. Lett.,* 77, 409-418, 1986.

Larson, D. B., and G. D. Anderson, Plane shock wave studies of geologic media, *J. Geopgys. Res.,* 84, 4592-4600, 1979.

Lyzenga, G. A., and T. J. Ahrens, Multiwavelength optical pyrometer for shock compression experiments, *Rev. Sci. Instum.,* 50, 1421-1424, 1979.

Malitson, I. H., Interspecimen comparison of the refractive index of fused silica, *J. Opt. Soc. Am.*, 55, 1205-1209, 1965.

Marsh, S. P., *LASL Shock Hugoniot Data*, 658 pp., University of California Press, Berkeley, 1980.

McHone, J. F., R. A. Nieman, C. F. Lewis, and A. M. Yates, Stishovite at the Cretaceous-Tertiary boundary, Raton, New Mexico, *Science*, 243, 1182-1184, 1989.

Melosh, H. J., *Impact Cratering: A geologic process*, 233-234, Oxford University Press, New york, 1989.

Melosh, H. J., N. M. Schneider, K. J. Zahnle, and D. Latham, Ignition of global fires at Cretaceous/Tertiary boundary, *Nature*, 343, 251-254, 1990.

Miller, G, and T. J. Ahrens, unpublished notes, 1989.

Murri, W. J., D. E. Grady, and K. D. Mahrer, Equation of state of rocks, *Final Rep. PYU-1883*, Stanford Res. Inst., Menlo Park, Calif., 1975.

O'Keefe, J. D., and T. J. Ahrens, Impact-induced energy partitioning, melting and vaporization on terrestrial planets, *LPSC VIII*, 3357-3374, Lunar and Planetary Institute, Houston, Texas, 1977.

O'Keefe, J. D., and T. J. Ahrens, Impact production of CO_2 by the Cretaceous/Tertiary extinction bolide and the resultant heating of the earth, *Nature*, 338, 247-249, 1989.

Pinto, J. P., R. P. Turco, and O. B. Toon, Self-limiting physical and chemical effects in volcanic eruption clouds, *J. Geophys. Res.*, 94, 11165-11174, 1989.

Pollack, J. B., O. B. Toon, T. P. Ackerman, C. P. McKay, and R. P. Turco, Environmental effects of an impact-generated dust cloud: implications for the Cretaceous-Tertiary extinctions, *Science*, 219, 287-289, 1983.

Pope, K. O., K. H. Baines, A. C. Ocampo, and B. A. Ivanov, Biospheric effects of sulfuric acid aerosols produced by the Chicxulub Cretaceous/Tertiary impact, *Earth Planet. Sci. Lett.*, 128, 719-725, 1994.

Prinn, R. G., and B. Fegley, Bolide impacts, acid rain and biospheric traumas at the Cretaceous-Tertiary boundary, *Earth Planet. Sci. Lett.*, 83, 1-15, 1987.

Raduosky, H. B., W. J. Nellis, M. Ross, D. C. Hamilton, and A. C. Mitchell, Molecular dissociation and shock-induced cooling in fluid nitrogen at high densities and temperatures, *Phys. Rev. Lett.*, 57, 2419-2422, 1986.

Radousky, H. B., and A. C. Mitchell, A fast UV/visible pyrometer for shock temperature measurements to 20000 K, *Rev. Sci. Instrum.*, 60, 3707-3710, 1989.

Rice, M. H., R. G. McQueen, and J. M. Walsh, Compression of solids by strong shock waves, in *Solid State Physics,* Vol. 6, F. Seitz and D. Turnbull, Eds., Academic Press Inc., New York, 1958.

Robie, R. A., B. S. Hemingway, and J. R. Fisher, *Thermodynamic Properties of Minerals and Related Substances at 298.15 K and 1 bar (10^5 Pascals) Pressure and at Higher Temperatures,* Geological Survey Bulletin 1452, 1979.

Roufosse, M. C., and R. Jeanloz, Thermal conductivity of minerals at high pressure: The effect of phase transition, *J. Geophys. Res.*, 88, 7399-7409, 1983.

Ruoff, A. L., Linear shock-velocity-particle-velocity relationship, *J. Appl. Res.*, 38, 4976-4980, 1967.

Schmidt, D. R., and T. J. Ahrens, Shock temperatures in silica glass-implications for modes of shock-induced deformation, phase-transformation, and melting with pressure, *J Geophys. Res.*, 94, 5851-5857, 1989.

Schuler, K. W., and D. E. Grady, Compression wave studies in Solenhofen Limestone, . *SAND76-0279,* Sandia Natl. Lab., Albuquerque, N. M. 1977.

Sharpton, V. L., K. Burke, A. Camargozanoguera, S. A. Hall, and D. S. Lee, Chicxulub multi-ring impact basin-size and other characteristics derived from gravity analysis, *Science,* 261, 1564-1567, 1993.

Sigurdsson, H., Assessment of the atmospheric impact of volcanic eruptions, in: *Global Catastrophes in Earth History; An Interdisciplinary Conference on Impact,*

Volcanism, and Mass Mortality, V. L. Sharpton, P. D. Ward and T. B. Museum, eds., Geol. Soc. Am. Spec. Pap. 247, 99-110, 1990a.

Sigurdsson, H., Evidence of volcanic loading of the atmosphere and climate response, *Palaeogeogr. Palaeoclimatol. Palaeoecol.*, 89, 277-289, 1990b.

Sigurdsson, H., S. D'Hondt, M. A. Arthur, T. J. Bralower, J. C. Zachos, M. Fossen, and J. E. T. Channell, Glass from the Cretaceous-Tertiary boundary in Haiti, *Nature*, 349, 482-487, 1991a.

Sigurdsson, H., Ph. Bonté, L. Turpin, M. Chausidon, N. Metrich, M. Steinberg, Ph. Prade, and S. D'Hondt, Geochemical constraints on source region of Cretaceous/Tertiary impact glasses, *Nature*, 353, 839-842, 1991b.

Sigurdsson, H., S. D'Hondt, and S. Carey, The impact of the Cretaceous/Tertiary bolide on evaporite terrane and generation of major sulfuric acid aerosol, *Earth Planet. Science Lett.*, 109, 543-559, 1992.

Simakov, G. V., M. N. Pavlovskiy, N. G. Kalashnikov, and R. F. Trunin, Shock Compressibility of Twelve Minerals, *Physics of the Solid Earth, No. 8,* 488-492, Academy of Science of the USSR, 1974.

Singh, A. K., and G. C. Kennedy, Compression of calcite to 40 kbar, *J. Geophys. Res., 79*, 2615-2622, 1974.

Stishov, S. M., The thermodynamics of melting of simple substances, *Sov. Phys. Usp.*, 17, 625-643, 1974.

Stishov, S. M., Entropy, disorder, melting, *Sov. Phys. Usp.*, 31, 52-67, 1988.

Svendsen, B., and T. J. Ahrens, Shock-induced temperatures of MgO, *Geophys. J. R. Astro. Soc.*, 91, 667-691, 1987.

Svendsen, B., and T. J. Ahrens, Optical radiation from shock-compressed materials and interfaces, *High-Pressure Research in Mineral Physics*, edited by M. H. Manghnani and Y. Syono, American Geophysical Union, Washington, D. C., pp. 403-423, 1987.

Swisher III, C. C., J. M. Grajales-Nishimura, A. Montanari, S. V. Margolis, P. Claeys, W. Alvarez, P. Renne, E. Cedillo-Pardo, F. J-M. R. Maurrasse, F. H. Curtis, J. Smit, and M. O. McWilliams, Coeval Ar-40/Ar-39 ages of 65.0 million years ago from Chicxulub crater melt rock and Cretaceous-Tertiary boundary tektites, *Science*, 257, 954-958, 1992.

Tackley, P. J., D. J. Stevenson, G. A. Glatzmaier, and G. Schubert, Effects of multiple phase transitions in a three-dimensional spherical model of convection in Earth's mantle, *J. Geophys. Res.*, 99, 15877-15901, 1994.

Tan, H., and T. J. Ahrens, Shock temperature measurements for metals, *High Pressure Research*, 2, 159-182, 1990.

Tang, W., The pressure and temperature dependence of thermal conductivity for nonmetal crystals. *Chinese J. High Press. Phys.*, 8, 125-132, 1994.

Trucano, T. G., and J. R. Asay, Effects of vaporization on debris cloud dynamics, *Int. J. Impact Engng.*, 5, 645-653, 1987.

Tyburczy, J. A., and T. J. Ahrens, Dynamic compression and volatile release of carbonates, *J. Geophys. Res.*, 91, 4730-4744, 1986.

Vizgirda, J., and T. J. Ahrens, Shock compression of aragonite and implications for the equation of state of carbonates, *J. Geophys. Res.*, 87, 4747-4758, 1982.

Williams, Q., R. Jeanloz, J. Bass, B. Svendsen, and T. J. Ahrens, The melting curve of iron to 250 gigapascals-A constraint on the temperature at Earth's center, *Science, 236*, 181-182, 1987.

Wise, J. L., and L. C. Chhabildas, Laser interferometer measurements of refractive index in shock-compressed materials, in *Shock Waves in Condensed Matter*-1985, edited by Y. M. Gupta, 441-454, Plenum, New York, 1986.

Wolbach, W. S., R. S. Lewis, and E. Anders, Cretaceous extinctions; evidence for wildfires and search for meteoritic material, *Science*, 230, 167-170, 1985.

Wyatt, C. L., *Radiometric System Design*, Macmillan Publishing Company, New York, 187-188, 1981.

Yoo, C. S., N. C. Holmes, M. Ross, D. J. Webb, and C. Pike, Shock temperatures and melting of iron at Earth core conditions, *Phys. Rev. Lett.*, 70, 3931-3934, 1993.

Zeldovich, Y. B., and Y. P. Raizer, *Physics of Shock Waves and High Temperature Phenomena*, Academic Press, New York, Vol. II, 1966.

Zhang, B., H. Zhao , H. Jiang, J. Li, S. Yun, S. Zhang, S. Yang, and T. Wang, *Explosion and its Application*, Defense Press, Beijing, p. 348,1979.

Zwick, H. H., and G. G. Shepard, Defocusing a wide-angle Michelsen interferometer, *Appl. Opt., 10,* 2569-2571, 1971.